Micromechanical Analysis of Random Composites

by

Michal Šejnoha and Jan Zeman

Czech Technical University
Faculty of Civil Engineering

2000

TABLE OF CONTENTS

LIST OF FIGURES

LIST OF TABLES

LIST OF ALGORITHMS

ACKNOWLEDGMENTS

We would like to express our deepest gratitude and thanks to Prof. Ing. Jiří Šejnoha, DrSc. for his support, endless patience, continuous encouragement and invaluable contribution to our education in solid mechanics. The financial support by the research project J04/98:210000003 and by the GAČR 103/97/P040, GAČR 103/00/0756 and GAČR 106/99/0096 is also gratefully acknowledged.

Michal Šejnoha

Jan Zeman

Prague

October 2000

Czech Technical University
Faculty of Civil Engineering

Abstract

Micromechanical Analysis of Random Composites

by Michal Šejnoha and Jan Zeman

Effective elastic properties are found for a fibrous graphite-epoxy composite system with fibers randomly distributed within a transverse plane section of the composite aggregate. Two different approaches are examined. The first approach assumes a well defined geometry of the fiber arrangement and specific boundary conditions. In the modeling framework, the complicated real microstructure is replaced by a material representative volume element consisting of a small number of particles, which statistically resembles the real microstructure. Periodic distribution of such unit cells is considered and the finite element method is called to carry out the numerical computation. The theoretical basis for the second approach are the Hashin-Shtrikman variational principles. The random character of the fiber distribution is incorporated directly into the variational formulation employing certain statistical descriptors.

A number of statistical descriptors suitable for the microstructure characterization of a random media are examined first. Several methods for their determination are proposed and tested for some simple theoretical models of microstructures. Additionally, a validity of various statistical hypotheses usually accepted for a random heterogenous media is checked for the real microstructure represented here by the graphite fiber tow embedded into the polymer matrix.

Suitable optimization procedure formulated in terms of selected statistical descriptors is proposed to derive the desired unit cell. A variety of stochastic optimization algorithms

is examined to solve this problem. Judging from our experience with similar optimization problems, the genetic algorithms based solution techniques are explored. This study suggests that the augmented simulated annealing method, which effectively combines the essentials of genetic algorithms with the basic concept of the simulated annealing method, is superior to other approaches. Applicability of such unit cells is tested for polymer systems. Nevertheless, other systems such as ceramic or metal matrix systems may also benefit from the present work.

A number of numerical studies are performed to quantify individual unit cells. The objective is to identify a number of particles required for specific problems to provide a sufficiently accurate representation of the behavior of real composites. A standard problem of deriving the effective mechanical properties is considered first. A general approach permitting either strain or stress control is pursued. It is observed that the unit cell consisting of five fibers only provides reasonably accurate estimates of the macroscopic properties. Similar conclusion follows from the thermal and viscoelastic problems considered next.

In certain applications the finite element tool used with the unit cell analysis may prove to be unnecessary expensive. In such a case, one may appreciate well known effective medium theories where applicable. Here, the most widely used variational principles of Hashin and Shtrikman extended to account for the presence of various transformation fields defined as local eigenstrain or eigenstress distributions in the phases are revisited. Random character of fibers arrangement is described here by the two-point probability function. When used with the Hashin-Shtrikman variational principles this function provides sufficient information for obtaining bounds on the effective material properties of real composites with statistically homogeneous microstructures. The Fourier transform is successfully implemented when solving the resulting integral equations.

Chapter 1

INTRODUCTION

The doubtless benefits offered by composite materials such as a high strength, light weight, non-corrosive properties, etc., have recently attracted many design engineers in civil engineering industry primarily in conjunction with rehabilitation and repair of concrete and masonry structures. A lucid discussion on this subject is given in the work of [Šejnoha et al., 1999]. An endless search for reliable and low cost structural and material systems resulted in inexpensive fabrication methods, which have made composites affordable to other applications such as facade and structural parts of both commercial and industrial buildings and even bridges.

Among the most prominent material systems complying with the aforementioned requirements remain polymer matrix systems reinforced either by aligned fibers, whiskers or fabrics. The latter ones, in particular, are under continuous rise in civil infrastructure applications. They are typically supplied in form of thick sandwich and laminated plates or woven tubes.

It has been long ago recognized that an overall response of such structures is highly influenced by micromechanical behavior of the composite systems. As suggested by Fig. 1.1, showing a sample of a graphite fiber fabric – polymer matrix composite system, such a research venture involves analyses on different scales. This example clearly manifests the importance of multi-scale modeling starting from large structural element, e.g. composite ply Fig. 1.1(a), having certain effective or macroscopic properties derived for the geometry specified on the meso-scale, Fig. 1.1(b). A classical problem of determining the effective elastic properties becomes even more complex when taking the level of constituents, micro-

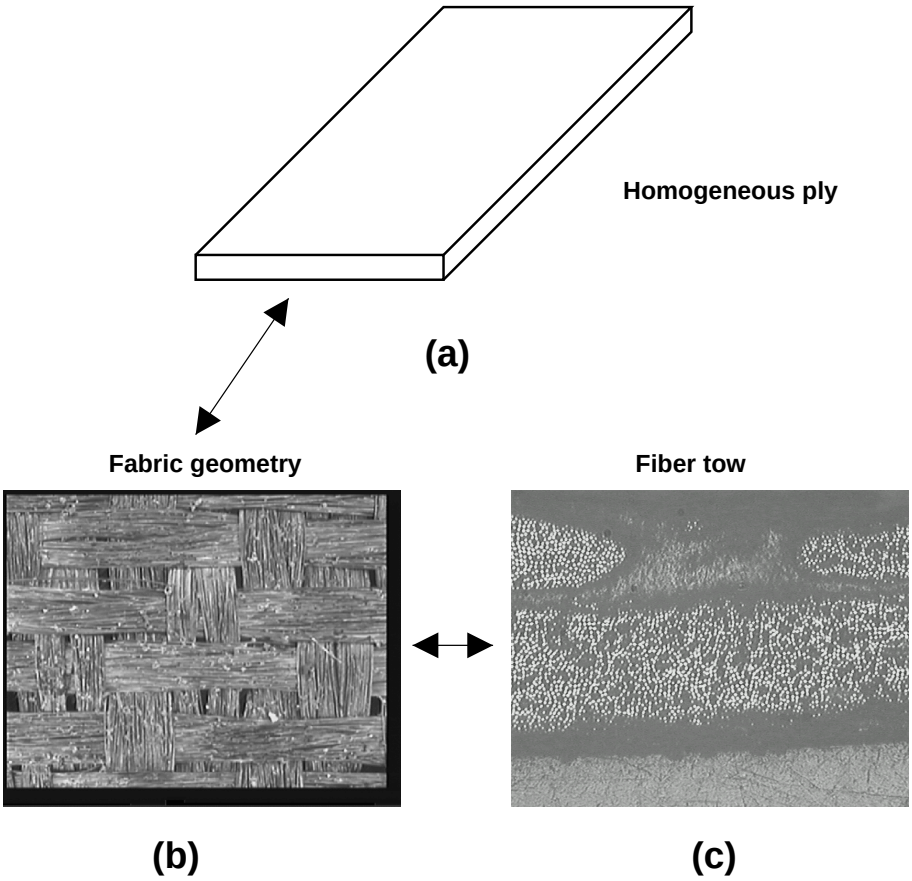

Figure 1.1: Graphite fiber fabric – polymer matrix composite

scale Fig. 1.1(c), into consideration. Such a step creates demands for special techniques enabling to determine the effective properties of disordered media.

To develop a multi-scale numerical model requires to start already at the micro-scale with the fiber and matrix mixture forming a fiber tow. Up to date the simple averaging techniques ([Hill, 1965, Mori and Tanaka, 1973, Benveniste, 1987] among others) were mostly used to generate effective properties of this basic building element. However, since fibers are randomly distributed within the bundle and since this distribution is likely affected by the initial fiber pre-stress it is advisable to treat homogenization on this level from the probabilistic methods point of view. To this date, there exists a well-founded physical and mathematical

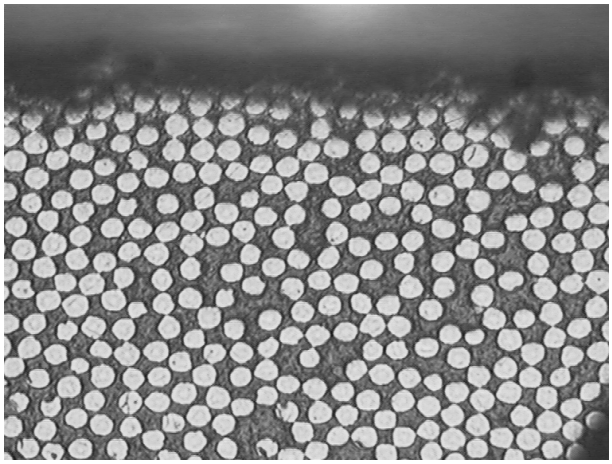

Figure 1.2: A real micrograph of a transverse plane section of the fiber tow

basis for describing the materials statistics including phase volume fractions and at minimum the two-point correlation function. A vast body of literature has been devoted to this subject (see [Beran, 1968, Drugan and Willis, 1996, Torquato, 1998, Zeman and Šejnoha, 2001] to cite a few).

Much of the work on characterizing the microstructure of heterogeneous materials now relies on the existence of images of real materials. The material system under consideration viewed under the scanning electron-microscope appears in Fig. 1.2. Such a medium is evidently disordered and conventional periodic unit cell models such as the hexagonal array model [Teplý and Dvořák, 1988] are not applicable. To provide for the lack of periodicity, one may incorporate various types of n-point statistical descriptors in the analysis of disordered media. Such statistical descriptors introduce information beyond that contained in the volume fractions. It turns out that the two-point correlation function S_{rs}, which gives the probability of finding two points $\mathbf{x}_1, \mathbf{x}_2$ randomly thrown into the media located in the phases r, s, is sufficient in determining the effective properties of the composite displayed in Fig. 1.2.

Knowing this function, the evaluation of overall response on the smallest size–scale calls for a suitable micromechanics analysis. Perhaps the most widely used approach draws on the Hashin-Shtrikman variational principle [Hashin and Shtrikman, 1963, Willis, 1977]. This approach has received considerable attention when the material deforms in proportion to the magnitude of the applied forces and temperature changes. Although this approach does not preclude description of material behavior at strains beyond the elastic limit, it is usually preferable to tackle such a problem with the help of a representative volume element defined in terms of a suitably chosen periodic unit cell (PUC).

As suggested by [Povirk, 1995], the original microstructure characterized by a certain statistical function, e.g., the two–point matrix probability function S_{mm}, can be replaced by a material representative volume element (RVE), which approximates the real material statistics as close as possible. Periodic microstructures are usually treated with this approach. Therefore, the RVE is assumed to be surrounded by the periodic replicas of itself. This step allows to substitute the complicated real microstructure by a *periodic unit cell* which consists of a small number of reinforcements and yet possesses similar statistical properties as the original material. The argument is that if the PUC has a statistically similar spatial distribution of fibers as the real microstructure it will also possess similar thermomechanical properties. Such a unit cell follows from an optimization procedure which keeps the difference between the statistical functions for the real microstructure and the PUC at minimum. This idea has been successfully implemented by [Zeman and Šejnoha, 2001, Zeman, 2000]. Standard homogenization technique can be used [Suquet, 1987, Michel et al., 1999] to analyze such unit cells under various thermomechanical loading conditions.

Detailed numerical simulations on the micro-scale, Fig. 1.1(c), combined with carefully selected laboratory measurements should offer homogenized constitutive law for graphite fiber tow/epoxy matrix mixture. Such a result then allows to carry out a proper analysis on the meso-scale. On this level of sophistication the computational challenge becomes obvious when examining the sample of woven composite plate in Fig. 1.1(b). A periodic character of the geometry shown in Fig. 1.1(b) suggests to formulate a representative volume element

in terms of a unit cell. The main task at this level is to find the macroscopic response of the unit cell for prescribed macroscopic strains or stresses resulted from the analysis on the macro-scale, Fig. 1.1(a). At this point the waviness and noticeable misalignment of fiber tow can be accounted for using tools provided again by statistical mechanics.

What has been said so far suggests possible routes one may wish to consider when dealing with complex composite structures such as the one in Fig. 1.1. The proposed approach inevitably creates demands for efficient computational strategies and algorithms linked to parallel environment.

The present work is confined to the micro-level. Various novel approaches discussed so far are introduced in very detail. A special attention is paid to the micromechanical analysis of random composites. Loading conditions are limited to those, which maintain the local stresses below the elastic limits. Nevertheless, residual strains associated with thermal effects or creep deformation are admitted.

The work is organized as follows. Chapter 2 reviews basic statistical descriptors for the two-phase random media. First, the concept of an ensemble is briefly discussed and the principle of *ensemble averaging* is outlined. Successively, various hypotheses often applied to random composite materials are remembered and tested for microstructures similar to that of Fig. 1.2. Microstructural descriptors suitable for the characterization of the two-phase two-dimensional media are introduced together with methods for their evaluation. Example results illustrate their applicability for the selected types of microstructures. A special attention is devoted to real composite systems represented here by a graphite–fiber tow bonded to the polymer matrix.

Chapter 3 deals with the micromechanical analysis of periodic microstructures. It takes the reader through a complex optimization process, which provides a unit cell with the same material statistics as the real composite. A variety of stochastic simulation techniques based on genetic algorithms is implemented to accomplish this task. The resulting periodic unit cell is then subjected to a set of thermomechanical loading conditions leading to uniform overall stress and strain fields. Applications to material systems prone to viscoelastic deformation

are visited in conjunction with generalized viscoelastic models of Maxwell or Kelvin types.

Micromechanical analysis of random composites combined with the Hashin-Shtrikman variational principles is the subject of Chapter 4. Both the primary and dual principles, extended to account for the presence of initial strains, are revisited in a systematic way. The main objective are macroscopic constitutive equations incorporating the random nature of the microstructure. The Fourier transform based approach is suggested to derive various microstructure dependent tensors or matrices entering the constitutive law. Demanding theoretical background is exposed in associated appendices.

Customary tensor and vector/matrix notation is used throughout this text. Tensor quantities are denoted either by lightface Greek letters e.g. σ_{ij}, L_{ijkl} ; (6×1) and (4×1) vectors are denoted by boldface italic letters, (6×6) and (4×4) matrices are denoted by uppercase boldface Roman letters e.g. $\mathbf{L}$ and scalars are denoted by lightface e.g. r. The inverse of non-singular matrix is denoted by $\mathbf{L}^{-1}$ and $\mathbf{L}^{\mathrm{T}}$ stands for transposition of matrix $\mathbf{L}$. Standard contracted notation is adopted when appropriate, thus $1 \equiv 11$, $2 \equiv 22$, $3 \equiv 33$, $4 \equiv 23$, $5 \equiv 13$ and $6 \equiv 12$. To distinguish the ensemble and volume averages, we adopt notation introduced by Beran [Beran, 1968] and denote an ensemble (or probabilistic) average of a function $\boldsymbol{u}(\mathbf{x})$ as $\overline{\boldsymbol{u}(\mathbf{x})}$, while in a volume-averaged sense we write $\langle \boldsymbol{u}(\mathbf{x}) \rangle$.

Chapter 2

QUANTIFICATION OF MICROSTRUCTURE MORPHOLOGY

Micromechanical analysis of composite materials with disordered microstructure is usually limited to applications of various approximate techniques such as the self-consistent or the Mori-Tanaka methods [Dvorak and Benveniste, 1992a]. However, when a certain knowledge of the real microstructure is available, the estimates of local fields can be improved by treating random composites. Such a modeling framework is considered throughout this text.

This opening chapter outlines evaluation of various statistical descriptors, which arise in the analysis of two–phase fibrous composites with random character of fibers arrangement. While the specific applications discussed in Chapters 3 and 4 are limited to the graphite fiber tow embedded in the polymer matrix, the theoretical background introduced in this chapter is quite general and can be applied to any two–phase random heterogeneous media of arbitrary phase geometry.

Section 2.1 reviews basic concepts and hypotheses associated with quantification of microstructure morphology. Individual statistical descriptors used in the present work are introduced in Section 2.2. Their evaluation for various types of microstructures is presented in Section 2.3. Finally, extension to a real composite system is provided in Section 2.4.

2.1 Basic concepts and hypotheses

To introduce the subject, imagine a collection of a large number of micrographs (ensemble) describing the geometry of a two phase fibrous composite. Example of such a micrograph is displayed in Fig. 2.1. Fig. 2.1(a) represents a portion of a graphite–fiber tow containing approximately twelve thousand fibers. A random cut consisting of about three hundred fibers

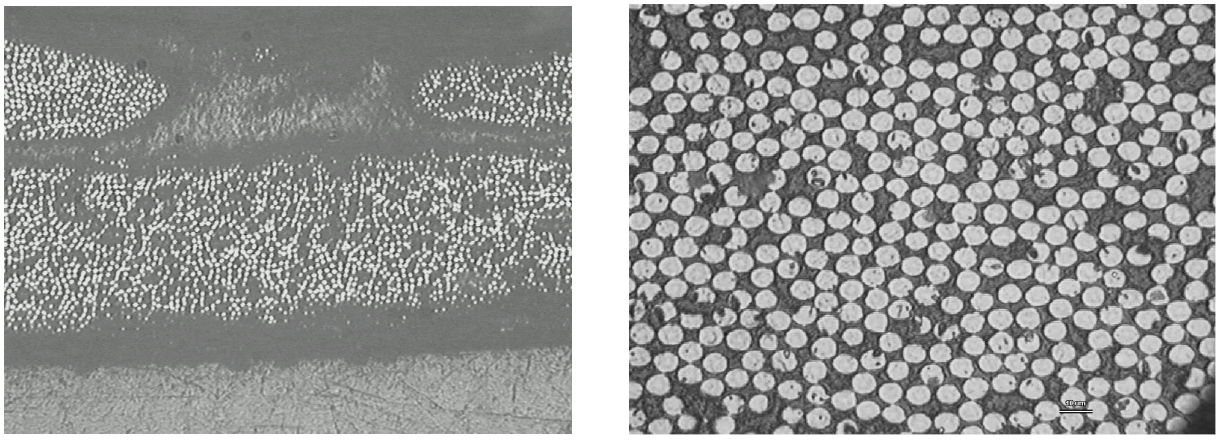

Figure 2.1: A real micrograph of a transverse plane section of the fiber tow

is shown in Fig. 2.1(b). Although having a large number of fibers, one can hardly assume that such a representative can completely describe the morphology of the whole composite. Simply taking similar micrographs from other parts of the fiber tow indicates substantial difference in the microstructure from sample to sample. The resulting representative, which would effectively sample all possible microstructural configurations, would be too large leading to enormous numerical calculations. To abandon such an unrealistic treatment one has to recognize the *random nature* of geometrical arrangements of phases - it means that the particular microstructure of a given sample yields only one possible arrangement of phases. Therefore, instead of determining the exact value of some quantity at a given point (which is sample dependent), attention is given to its *expected* or *averaged* or *macroscopic* value, which incorporates information from all samples taken from a material.

2.1.1 Concept of an ensemble

To reflect a random character of a heterogeneous media it is convenient to introduce the concept of an *ensemble* – the collection of a large number of systems which are different in their microscopical details but they are entirely identical within a point of view of macroscopic de-

tails (see e.g. [Beran, 1968, Boublík, 1996]). Within this concept, *effective* or *expected* value of some quantity corresponds to the process of its averaging through all systems, forming the ensemble.

To begin, consider a sample space $\mathcal{S}$, identify individual members of this space by α and define $p(\alpha)$ as the probability density of α in $\mathcal{S}$ (see [Drugan and Willis, 1996] and [Kohler and Papanicalou, 1982] for further reference). Then the *ensemble average* of function $F(\mathbf{x}, \alpha)$ at point $\mathbf{x}$ is provided by

$$\overline{F(\mathbf{x})} = \int_{\mathcal{S}} F(\mathbf{x}, \alpha) p(\alpha) \mathrm{d}\alpha. \tag{2.1}$$

Following the above definition would require experimental determination of the ensemble average of function $F(\mathbf{x}, \alpha)$ for a given point $\mathbf{x}$ through the cumbersome procedure of manufacturing a large number of samples (which form the ensemble space $\mathcal{S}$), measuring $F(\mathbf{x}, \alpha)$ for every sample and then its averaging for all samples. Therefore, it appears meaningful to introduce certain hypotheses regarding the ensemble average, which substantially simplify this task.

2.1.2 Ergodic hypothesis

This hypothesis demands all states available to an ensemble of the systems to be available to every member of the system in the ensemble as well ([Beran, 1968]). Once this hypothesis is adopted, *spatial* or *volume average* of function $F(\mathbf{x}, \alpha)$ given by

$$\langle F(\mathbf{x}, \alpha) \rangle = \lim_{V \to \infty} \frac{1}{V} \int_V F(\mathbf{x} + \mathbf{y}, \alpha) \mathrm{d}\mathbf{y} \tag{2.2}$$

is independent of α and identical to the *ensemble average*,

$$\langle F(\mathbf{x}) \rangle = \overline{F(\mathbf{x})}. \tag{2.3}$$

This hypothesis allows to examine only one arbitrary member of the sample space, provided that the sample is "sufficiently large" (see Eq. (2.2)). A possible way to fulfill this condition is to assume a periodic composite described by a unit cell Ω. Then,

$$\lim_{V \to \infty} \frac{1}{V} \int_V F(\mathbf{x} + \mathbf{y}, \alpha) \mathrm{d}\mathbf{y} = \frac{1}{\Omega} \int_\Omega F(\mathbf{x} + \mathbf{y}, \alpha) \mathrm{d}\mathbf{y} \tag{2.4}$$

so for the ergodic periodic composite medium, the ensemble average is equal to the volume average taken over the unit cell.

2.1.3 Statistical homogeneity

Suppose that function F depends on n vectors $\mathbf{x}_1, \ldots, \mathbf{x}_n$. If the material is *statistically homogeneous* the ensemble average of F is invariant with respect to translation [Beran, 1968, Torquato and Stell, 1982], so the expression

$$\overline{F(\mathbf{x}_1, \ldots, \mathbf{x}_n)} = \overline{F(\mathbf{x}_1 - \mathbf{y}, \ldots, \mathbf{x}_n - \mathbf{y})} \tag{2.5}$$

holds for an arbitrary value of $\mathbf{y}$. The most common choice is to set $\mathbf{y} = \mathbf{x}_1$, so

$$\overline{F(\mathbf{x}_1, \ldots, \mathbf{x}_n)} = \overline{F(\mathbf{0}, \mathbf{x}_2 - \mathbf{x}_1, \ldots, \mathbf{x}_n - \mathbf{x}_1)} = \overline{F(\mathbf{x}_{12}, \ldots, \mathbf{x}_{1n})}, \tag{2.6}$$

where $\mathbf{x}_{ij} = \mathbf{x}_j - \mathbf{x}_i$.

2.1.4 Statistical isotropy

Further simplification arises when assuming the material to be *statistically isotropic*. In such a case, the ensemble average is not only independent of the position of the coordinate system origin but also of the coordinate system rotation. Under this hypothesis, the ensemble average depends on the absolute value of vectors $\mathbf{x}_{12}, \ldots, \mathbf{x}_{1n}$ only:

$$\overline{F(\mathbf{x}_{12}, \ldots, \mathbf{x}_{1n})} = \overline{F(r_{ij})} \tag{2.7}$$

where $r_{ij} = \|\mathbf{x}_{ij}\|, i = 1, \ldots, n, j = i, \ldots, n$.

2.2 Microstructure description

A number of statistical descriptors are available to characterize the microstructure of a two–phase random medium. This section describes two specific sets of descriptors which proved to be useful in the present work. First, a set of general n–point probability functions, applicable to an arbitrary two–phase composite, is introduced. A different set of statistical

functions deserves attention when considering a particulate composite. Both sets are introduced through a fundamental random function relevant to the microstructure configuration. Then, statistical moments of this function are identified as descriptors of the microstructure morphology. Finally, connection between individual sets of statistical descriptors is demonstrated.

2.2.1 Microstructure description for general composites

Fundamental function and statistical moments. Consider an ensemble of a two-phase random media. To provide a general statistical description of such a system it proves useful to characterize each member of the ensemble by a random stochastic function– *characteristic* or *indicator* function $\chi_r(\mathbf{x}, \alpha)$, which is equal to one when point $\mathbf{x}$ lies in phase r in the sample α and equal to zero otherwise [Beran, 1968, Torquato and Stell, 1982],

$$\chi_r(\mathbf{x}, \alpha) = \begin{cases} 1 & \mathbf{x} \in D_r(\alpha) \\ 0 & \text{otherwise.} \end{cases}, \tag{2.8}$$

where $D_r(\alpha)$ denotes the domain occupied by r-th phase; $r = m, f$ is further assumed to take values m for the matrix phase while symbol f is reserved for the second phase. Except where noted, a fibrous composite with aligned impenetrable fibers having circular cross-section of equal radius is considered ($f \rightarrow$ fiber). For such a system the characteristic functions $\chi_f(\mathbf{x}, \alpha)$ and $\chi_m(\mathbf{x}, \alpha)$ are related by

$$\chi_m(\mathbf{x}, \alpha) + \chi_f(\mathbf{x}, \alpha) = 1. \tag{2.9}$$

Following [Torquato and Stell, 1982, Beran, 1968, Drugan and Willis, 1996], we write the ensemble average of the product of characteristic functions

$$S_{r_1,\ldots,r_n}(\mathbf{x}_1,\ldots,\mathbf{x}_n) = \overline{\chi_{r_1}(\mathbf{x}_1,\alpha)\cdots\chi_{r_n}(\mathbf{x}_n,\alpha)}, \tag{2.10}$$

where function $S_{r_1,\ldots,r_n}$ referred to as the *general n-point probability* gives the probability of finding n points $\mathbf{x}_1,\ldots,\mathbf{x}_n$ randomly thrown into media located in the phases $r_1,\ldots,r_n$.

Functions of the first and second order. Hereafter, we limit our attention to functions of the order of one and two, since higher-order functions are quite difficult to determine in practice. Therefore, description of the random media will be provided by the *one-point probability* function $S_r(\mathbf{x})$

$$S_r(\mathbf{x}) = \overline{\chi_r(\mathbf{x},\alpha)}, \tag{2.11}$$

which simply gives the probability of finding the phase r at $\mathbf{x}$ and by the *two-point probability* function $S_{rs}(\mathbf{x},\mathbf{x}')$

$$S_{rs}(\mathbf{x},\mathbf{x}') = \overline{\chi_r(\mathbf{x},\alpha)\chi_s(\mathbf{x}',\alpha)}, \tag{2.12}$$

which denotes the probability of finding simultaneously phase r at $\mathbf{x}$ and phase s at $\mathbf{x}'$. In general, evaluation of these characteristics may prove to be prohibitively difficult. Fortunately, a simple method of attack can be adopted when accepting a reasonable assumption regarding the material as statistically homogeneous, so that

$$S_r(\mathbf{x}) = S_r, \tag{2.13}$$

$$S_{rs}(\mathbf{x},\mathbf{x}') = S_{rs}(\mathbf{x}-\mathbf{x}'). \tag{2.14}$$

Further simplification arises when assuming the medium to be *statistically isotropic*. Then $S_{rs}(\mathbf{x}-\mathbf{x}')$ reduces to

$$S_{rs}(\mathbf{x}-\mathbf{x}') = S_{rs}(\|\mathbf{x}-\mathbf{x}'\|). \tag{2.15}$$

Finally, making an ergodic assumption allows to substitute the one-point correlation function by its volume average,i.e., *volume concentration* or *volume fraction* of the r-th phase c_r,

$$S_r = c_r. \tag{2.16}$$

Limiting values. In addition, the two-point probability function S_{rs} depends on the one-point probability function S_r for certain values of its arguments such that

$$\text{for } \mathbf{x} \to \mathbf{x}' \quad : \quad S_{rs}(\mathbf{x}, \mathbf{x}') = \delta_{rs} S_r(\mathbf{x}), \tag{2.17}$$

$$\text{for } \|\mathbf{x} - \mathbf{x}'\| \to \infty \quad : \quad \lim_{\|\mathbf{x}-\mathbf{x}'\|\to\infty} S_{rs}(\mathbf{x}, \mathbf{x}') = S_r(\mathbf{x}) S_s(\mathbf{x}'), \tag{2.18}$$

where symbol δ_{rs} stands for Kronecker's delta. Relation (2.17) states that probability of finding two different phases at a single point is equal to 0 (see also Eq. (2.9)) or is given by the one-point probability function if phases are identical. Equation (2.18) manifests that for large distances points $\mathbf{x}$ and $\mathbf{x}'$ are statistically independent. This relation is often denoted as the *no-long range orders* hypothesis (see e.g. [Willis, 1977]).

Finally, according to Eq. (2.9) we may determine one and two-point probability functions for all phases providing these functions are given for one arbitrary phase. For one-point probability function of statistically homogeneous and ergodic media, this relation assumes a trivial form

$$c_m = 1 - c_f. \tag{2.19}$$

Relations for the two-point probability functions of statistically isotropic and ergodic medium are summarized in Table 2.1. Note that symbol r which stands for $\|\mathbf{x}\|$ in Table 2.1 should not be mistaken with subscripted r used as a phase index heretofore.

	Known function		
	$S_{mm}(r)$	$S_{mf}(r)$	$S_{ff}(r)$
$S_{mm}(r)$	$S_{mm}(r)$	$c_m - S_{mf}(r)$	$c_m - c_f + S_{ff}(r)$
$S_{mf}(r)$	$c_m - S_{mm}(r)$	$S_{mf}(r)$	$c_f - S_{ff}(r)$
$S_{ff}(r)$	$c_f - c_m + S_{mm}(r)$	$c_f - S_{mf}(r)$	$S_{ff}(r)$

Table 2.1: Relations between two-point probability functions

2.2.2 Microstructure description for particulate composites

Another approach to the microstructure characterization can be adopted when the composite material is *particulate* - it consists of particles with identical specific shape (e.g. ellipsoids, cylinders etc.) embedded in a matrix phase. Note that fibrous composites fall under this category. Microstructure morphology of such a composite can be described using only *centers* of particles. This approach is frequently used in the statistical mechanics of liquids (see e.g. [Boublík, 1996, Chapter 6]). Its principles will be applied here.

Fundamental function and statistical moments. Suppose that each sample α in $\mathcal{S}$ is formed by N distinguishable particles with centers located at distinct points $\mathbf{x}_\alpha^1, \ldots, \mathbf{x}_\alpha^N$ placed in a matrix of volume (area) V. Such a system of random points can be described using the random field density function $\psi(\mathbf{x}, \alpha)$ (see [Ponte Casteñada and Willis, 1995, Markov, 1998] and references therein)

$$\psi(\mathbf{x}, \alpha) = \sum_{i=1}^{N} \delta(\mathbf{x} - \mathbf{x}_\alpha^i), \tag{2.20}$$

where $\delta(\cdot)$ stands for Dirac's function.

The foregoing procedure is similar to that described in Section 2.2.1. The *generic n-particle probability density function* $\rho_n(\mathbf{x}_1, \ldots, \mathbf{x}_n)$ for *distinct* points $\mathbf{x}_1, \ldots, \mathbf{x}_n$ is found by ensemble averaging the product of basic functions,

$$\rho_n(\mathbf{x}_1, \ldots, \mathbf{x}_n) = \overline{\psi(\mathbf{x}_1, \alpha) \cdots \psi(\mathbf{x}_n, \alpha)}, \tag{2.21}$$

which gives the probability density of finding a particle center in all points $\mathbf{x}_1, \ldots, \mathbf{x}_n$ randomly thrown into the material ([Boublík, 1996, Quintanilla and Torquato, 1997]).

Functions of the first and second order. To keep formal similarity with Section 2.2.1 we confine the following discussion to the one and two-particle functions only. Starting from the *generic one-particle probability density function* modify Eq. 2.21 to read

$$\rho_1(\mathbf{x}) = \overline{\psi(\mathbf{x}, \alpha)}, \tag{2.22}$$

which gives the probability density of finding an inclusion centered at $\mathbf{x}$. The *generic two-particle probability density function* is then provided by

$$\delta(\mathbf{x}-\mathbf{x}')\rho_1(\mathbf{x}) + \rho_2(\mathbf{x},\mathbf{x}') = \overline{\psi(\mathbf{x},\alpha)\psi(\mathbf{x}',\alpha)}, \tag{2.23}$$

which represents the probability density of finding one inclusion centered at $\mathbf{x}$ and the second one at $\mathbf{x}'$. The first term in Eq. (2.23) is added to allow for points $\mathbf{x}$ and $\mathbf{x}'$ become coincident. This modification is easily justified by making an assumption about *statistical homogeneity* to get

$$\rho_1(\mathbf{x}) = \rho_1 \tag{2.24}$$

$$\rho_2(\mathbf{x},\mathbf{x}') = \rho_2(\mathbf{x}-\mathbf{x}'). \tag{2.25}$$

If the material is *statistically isotropic* the function $\rho_2(\mathbf{x}-\mathbf{x}')$ reduces to

$$\rho_2(\mathbf{x}-\mathbf{x}') = \rho_2(\|\mathbf{x}-\mathbf{x}'\|). \tag{2.26}$$

Finally, making an ergodic assumption equals the value of the one-point probability density function of statistically homogeneous media to the *number of particle centers per unit volume*

$$\rho_1 = \rho = \lim_{V\to\infty} \frac{N}{V}. \tag{2.27}$$

Limiting values. Recall that $\overline{\psi(\mathbf{x},\alpha)\psi(\mathbf{x}',\alpha)}$ gives the probability density of finding particle centers located at points $\mathbf{x}$ and $\mathbf{x}'$ randomly thrown into the sample. When points $\mathbf{x}$ and $\mathbf{x}'$ happen to coincide, this probability density is simply equal to the probability density of finding a particle center at point $\mathbf{x}$ (note that one point $\mathbf{x}$ cannot be occupied by two centers of distinguishable particles). Therefore,

$$\text{for } \mathbf{x}\to\mathbf{x}' \quad : \quad \overline{\psi(\mathbf{x},\alpha)\psi(\mathbf{x}',\alpha)} = \overline{\psi(\mathbf{x},\alpha)} = \rho_1(\mathbf{x}). \tag{2.28}$$

However, when $\|\mathbf{x}-\mathbf{x}'\| \to \infty$ we have

$$\overline{\psi(\mathbf{x},\alpha)\psi(\mathbf{x}',\alpha)} = \lim_{\|\mathbf{x}-\mathbf{x}'\|\to\infty} \rho_2(\mathbf{x},\mathbf{x}') = \rho_1(\mathbf{x})\rho_1(\mathbf{x}'). \tag{2.29}$$

Combining Eqs. (2.24), (2.27) and (2.29) yields.

$$\rho_1(\mathbf{x})\rho_1(\mathbf{x}') = \rho^2.$$

For statistically homogeneous and ergodic medium this suggests to introduce the *radial* or *pair distribution function* $g_2(\mathbf{x}-\mathbf{x}')$ [Axelsen, 1995, Boublík, 1996, Pyrz, 1994]

$$g_2(\mathbf{x}-\mathbf{x}') = \frac{\rho_2(\mathbf{x}-\mathbf{x}')}{\rho^2}, \tag{2.30}$$

which equals one for points $\mathbf{x}$ and $\mathbf{x}'$ spread infinitely apart. Literature offers another distribution function known as the *total correlation function* $h(\mathbf{x}-\mathbf{x}')$ [Boublík, 1996]

$$h(\mathbf{x}-\mathbf{x}') = g_2(\mathbf{x}-\mathbf{x}') - 1. \tag{2.31}$$

Note that $h(\mathbf{x}-\mathbf{x}') \to 0$ when the mutual distance of points $\mathbf{x}$ and $\mathbf{x}'$ increases infinitely, which may be of value in certain applications.

Either function can be used to provide the desired statistics of the composite sample. To employ these functions, however, requires the knowledge of function ρ_2 for a given microstructures which is rather difficult to determine. Fortunately, a suitable substitute is available through the *second order intensity function* $K(r)$ defined by [Ripley, 1977]. This function gives the number of further points expected to lie within a radial distance r of an arbitrary point divided by the number of particles (fibers) per the unit area and is related to the radial distribution function by

$$g_2(r) = \frac{1}{2\pi r}\frac{\mathrm{d}K(r)}{\mathrm{d}r}. \tag{2.32}$$

Unlike the *generic two-particle probability density function* ρ_2, the function $K(r)$ can be easily evaluated. Details are given in Section 2.3.

Finally, we turn our attention to composite media consisting of non-overlapping particles. The impenetrability condition implies that $\rho_2(\mathbf{x},\mathbf{x}')$ is equal to zero for all $(\mathbf{x}-\mathbf{x}') \in \Omega_d$. It means that each particle center is surrounded by a "secure area" Ω_d which cannot be occupied by another particle center. If we consider a unidirectional fiber composite with identical circular fibers of radius R, then Ω_d is a cylinder with radius $2R$ centered at $\mathbf{x}$.

2.2.3 Connection between functions S and ρ for particulate microstructures

To reconcile individual approaches discussed in Sections 2.2.1 and 2.2.2 it is desirable to establish a connection between functions S_n and ρ_n. Since function ρ_n applies only to particulate composites, we limit our discussion to such a type of systems.

In principle, it suffices to relate the characteristic function $\chi_r(\mathbf{x}, \alpha)$ and the probability density function $\psi(\mathbf{x}, \alpha)$. It is easy to notice that for the composite formed by impenetrable particles the following relation holds [Ponte Casteñada and Willis, 1995]

$$\chi_f(\mathbf{x}, \alpha) = \int \psi(\mathbf{y}, \alpha) m(\mathbf{x} - \mathbf{y}) \mathrm{d}\mathbf{y}, \tag{2.33}$$

where $m(\mathbf{y})$ is the characteristic function of one inclusion with center at the origin of coordinate system.

Then, substituting Eq. (2.33) into Eq. (2.12) and and making use of Eq. (2.23) gives

$$\begin{aligned} S_{ff}(\mathbf{x}_1, \mathbf{x}_2) &= \int\int m(\mathbf{x}_1 - \mathbf{x}_3) m(\mathbf{x}_2 - \mathbf{x}_4) \left[\int \psi(\mathbf{x}_3, \alpha) \psi(\mathbf{x}_4, \alpha) p(\alpha) \mathrm{d}\alpha \right] \mathrm{d}\mathbf{x}_3 \mathrm{d}\mathbf{x}_4 \\ &= \int\int m(\mathbf{x}_1 - \mathbf{x}_3) m(\mathbf{x}_2 - \mathbf{x}_4) \left[\delta(\mathbf{x}_3 - \mathbf{x}_4) \rho_1(\mathbf{x}_3) + \rho_2(\mathbf{x}_3, \mathbf{x}_4) \right] \mathrm{d}\mathbf{x}_3 \mathrm{d}\mathbf{x}_4. \end{aligned}$$

For statistically homogeneous and ergodic media this expression invites a substitution of $h(\mathbf{x}_3, \mathbf{x}_4)$ for $\rho_2(\mathbf{x}_3, \mathbf{x}_4)$ to get

$$\begin{aligned} S_{ff}(\mathbf{x}_1 - \mathbf{x}_2) &= \rho\, \Omega_{int}(\mathbf{x}_1 - \mathbf{x}_2) + \rho^2 \Omega^2 + \\ &+ \rho^2 \int\int h(\mathbf{x}_3 - \mathbf{x}_4) m(\mathbf{x}_1 - \mathbf{x}_3) m(\mathbf{x}_2 - \mathbf{x}_4) \mathrm{d}\mathbf{x}_3 \mathrm{d}\mathbf{x}_4, \end{aligned} \tag{2.34}$$

where $\Omega_{int}(\mathbf{x}_1 - \mathbf{x}_2)$ stands for the intersection volume (area) of two particles with centers located at points $\mathbf{x}_1$ and $\mathbf{x}_2$ and Ω is the volume (area) of one particle. Knowing the function S_{ff} one may use results from Table 2.1 to establish similar relations for all remaining functions. In particular, the two–point matrix probability function S_{mm} assumes the form

$$\begin{aligned} S_{mm}(\mathbf{x}_1 - \mathbf{x}_2) &= 1 - \rho\, \Omega_u(\mathbf{x}_1 - \mathbf{x}_2) + \rho^2 \Omega^2 + \\ &+ \rho^2 \int\int h(\mathbf{x}_3 - \mathbf{x}_4) m(\mathbf{x}_1 - \mathbf{x}_3) m(\mathbf{x}_2 - \mathbf{x}_3) \mathrm{d}\mathbf{x}_3 \mathrm{d}\mathbf{x}_4, \end{aligned} \tag{2.35}$$

where $\Omega_u(\mathbf{x}_1 - \mathbf{x}_2) = 2\Omega - \Omega_{int}(\mathbf{x}_1 - \mathbf{x}_2)$ is the union volume (area) of two particles with centers located at points $\mathbf{x}_1$ and $\mathbf{x}_2$. This relation is equivalent to formulas derived by [Torquato and Stell, 1985] using a slightly different procedure.

To further simplify Eq. (2.35) we consider a statistically isotropic two-dimensional composite formed by identical circles with radius R. In such a case, the two–point matrix probability function is provided by

$$\begin{aligned} S_{mm}(r_{12}) &= 1 - \rho\,\Omega_u(r_{12}) + \rho^2\Omega^2 + \rho^2 \int\int h(r_{34})m(r_{13})m(r_{23})\mathrm{d}\mathbf{x}_3\mathrm{d}\mathbf{x}_4 \\ &= 1 - \rho\,\Omega_u(r_{12}) + \rho^2\Omega^2 + \rho^2 M(r_{12}), \end{aligned} \tag{2.36}$$

where Ω equals to πR^2. Functions $m(\mathbf{x})$ and $\Omega_u(\mathbf{x})$ depend on $r = \|\mathbf{x}\|$ only and are given by

$$m(r) = \begin{cases} 1 & r \le R \\ 0 & \text{otherwise} \end{cases}, \tag{2.37}$$

$$\Omega_u(r) = \begin{cases} 2R^2\left[\pi - \arccos(r/2R) + r/2R\sqrt{1-(r/2R)^2}\right] & r < 2R \\ 2\pi R^2 & r \ge 2R \end{cases}. \tag{2.38}$$

Evaluation of the last term in Eq. (2.36) creates no obstacles since $M(r)$ is in fact a double convolution. In such a case the Fourier transform of M is given as a multiplication of the Fourier transforms of individual functions (see Appendix C)

$$\widetilde{M}(t) = \widetilde{h}(t)\widetilde{m}(t)\widetilde{m}(t). \tag{2.39}$$

After some algebra outlined in Appendix B we arrive at

$$\widetilde{m}(t) = \frac{2\pi R}{t} J_1(R\,t) \tag{2.40}$$

$$\widetilde{h}(t) = 2\pi \int_0^\infty h(t) J_0(rt)\, r\,\mathrm{d}r = t\int_0^\infty \widetilde{K}(r) J_1(rt)\mathrm{d}r, \tag{2.41}$$

where $J_0(\cdot)$ and $J_1(\cdot)$ in above equations are the Bessel functions of the first kind, zero and first order, respectively, and $\widetilde{K}(r) = K(r) - \pi r^2$. The inverse Fourier transform is then written as

$$M(r) = \frac{1}{2\pi}\int_0^\infty \widetilde{M}(t) J_0(rt) t\,\mathrm{d}t. \tag{2.42}$$

2.3 Numerical evaluation of microstructural statistics

Numerical evaluation of microstructural statistics introduced in the previous sections proceeds as follows. We begin with the n-point probability functions assuming a statistically homogeneous and ergodic medium. To that end, two different approaches are examined. First, a simple simulation technique is proposed. Next, an approach suitable for digitized media is explored. The determination of the radial distribution function is performed by deterministic procedure. At present, a statistical isotropy is assumed explicitly.

Precision of individual methods is tested for both theoretical and real microstructures. In general, a heterogeneous medium formed by N identical circles with radius R and centers located at positions $\mathbf{x}^1, \ldots, \mathbf{x}^N$ embedded in the rectangle with dimensions $\langle 0; H_1 \rangle \times \langle 0; H_2 \rangle$ is considered.

2.3.1 Functions S_n

To determine $S_{r_1,\ldots,r_n}$ we recall that the *general n-point probability* gives the probability of finding n points $\mathbf{x}_1, \ldots, \mathbf{x}_n$ randomly thrown into a medium located in the phases $r_1, \ldots, r_n$. Among all functions, the one–point and two–point probability functions deserve a special attention as they arise in the formulation of macroscopic constitutive equations of random composites discussed in Chapter 4. In view of Table 2.1 we further consider only the matrix probability functions.

To follow up the above definition, the one–point matrix probability function S_m gives the chance of finding a randomly placed point located in the matrix phase. To determine this quantity, a simple Monte-Carlo like simulation can be utilized – we throw a randomly point into the microstructure and count successful "hits" into the matrix phase. Then, the value of function S_m can be estimated as

$$S_m \approx \frac{n'}{n}, \tag{2.43}$$

where n' is the number of successful hits and n denotes the total number of throws. Entirely similar procedure can be employed to determine values of $S_{mm}(\mathbf{x})$.

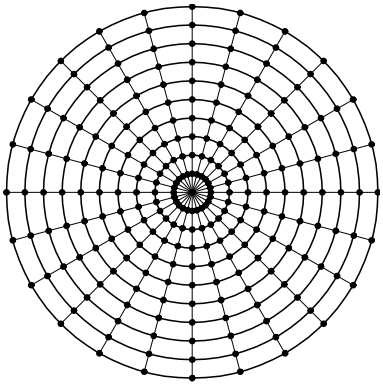

Figure 2.2: Example of sampling template

Smith and Torquato, [Smith and Torquato, 1988], proposed another procedure which appeals to the determination of $S_{mm}(\mathbf{x})$. Instead of tossing a line corresponding to $\mathbf{x}$ into a medium, sampling template is formed (see Fig. 2.2). The center of such a sampling template is randomly thrown into a medium and corresponding successful hits are counted. Furthermore, if the medium under consideration is statistically isotropic, values found for points located on the same circumference can be averaged as well, which allows large number of tests to be performed within one placement of the template. Although simple, such simulations are computationally very intensive.

Another, more attractive approach, is available when the real microstructure is replaced by its binary image. A binary version of Fig. 2.1(b) is shown in Fig. 2.3. Such a digitized micrograph can be imagined as a discretization of the characteristic function $\chi_r(\mathbf{x}, \alpha)$, usually presented in terms of a $M \times N$ bitmap. Denoting the value of χ_r for the pixel located in the i^{th} row and j^{th} column as a $\chi_r(i, j)$ allows to write the first two moments of function S_n for an ergodic and statistically homogeneous medium in the form

$$S_r = \frac{1}{MN} \sum_{i=1}^{M} \sum_{j=1}^{N} \chi_r(i, j) \tag{2.44}$$

$$S_{rs}(m, n) = \frac{1}{(i_m - i_M + 1)(j_m - j_M + 1)} \sum_{i=i_m}^{i_M} \sum_{j=j_m}^{j_M} \chi_r(i, j)\chi_s(i + m, j + n), \tag{2.45}$$

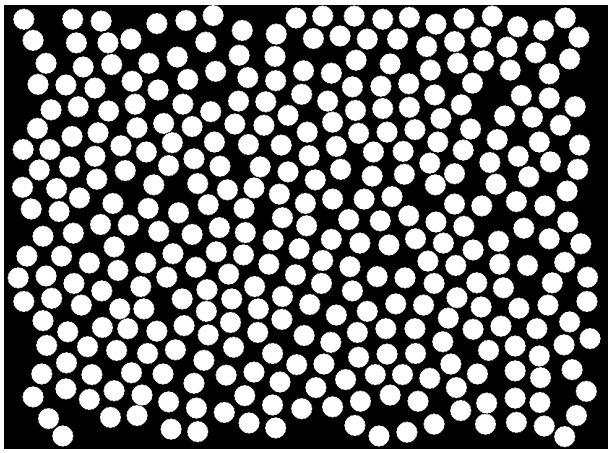

Figure 2.3: Idealized binary image of Fig. 2.1(b); resolution 976x716 pixels

where $i_m \geq (1-m, 1), i_M \leq (M, M-m)$. Observe that to compute function S_r requires $O(MN)$ operations, while $O((MN)^2)$ operations are needed for function S_{rs}. This might be computationally demanding, particularly for a large micrograph, and does not seem to bring any advantageous over simulation techniques.

The required number of operations, however, can be reduced when writing the two–point probability function S_{rs} for the periodic ergodic media as a *correlation* of functions χ_r and χ_s, recall Eq. (2.4),

$$S_{rs}(\mathbf{x}) = \frac{1}{\Omega}\int_{\Omega} \chi_r(\mathbf{y})\chi_s(\mathbf{x}+\mathbf{y})\mathrm{d}\mathbf{y} \tag{2.46}$$

Then, using relation (C.11) the Fourier transform of S_{rs} is provided by

$$\widetilde{S}_{rs}(\boldsymbol{\xi}) = \frac{1}{\Omega}\widetilde{\chi_r}(\boldsymbol{\xi})\overline{\widetilde{\chi_s}(\boldsymbol{\xi})}, \tag{2.47}$$

where $\bar{\cdot}$ now stands for the complex conjugate. Taking advantage of the periodicity of function χ_r one may implement the Discrete Fourier Transform (DFT) [Burrus and Parks, 1985] when evaluating Eq. (2.47). To shed a light on this subject we first write the discrete version of Eq. (2.46) in the form

$$S_{rs}(m,n) = \frac{1}{MN}\sum_{i=1}^{M}\sum_{j=1}^{N} \chi_r(i,j)\chi_s((i+m)\%(M),(j+n)\%N), \tag{2.48}$$

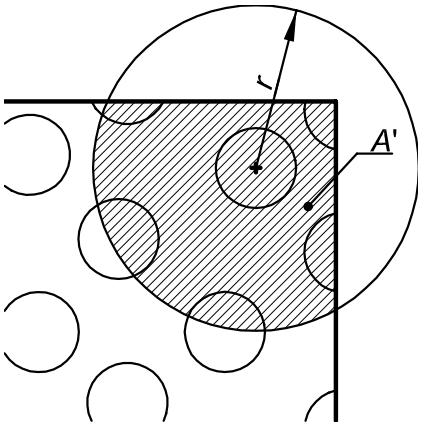

Figure 2.4: Correction factor

where symbol "%" stands for modulo. The above equation, usually termed the cyclic correlation, readily implies periodicity of function S_{rs}. Note that the correlation property of DFT holds for cyclic correlation. Referring to Eq. (2.47) it is given by the following relation

$$\mathrm{DFT}\{S_{rs}(m,n)\} = \mathrm{DFT}\{\chi_r(m,n)\}\mathrm{DFT}\overline{\{\chi_s(m,n)\}}. \tag{2.49}$$

The inverse DFT denoted as IDFT then serves to derive function S_{rs} at the final set of discrete points as

$$S_{rs}(m,n) = \mathrm{IDFT}\{\mathrm{DFT}\{\chi_r(m,n)\}\mathrm{DFT}\overline{\{\chi_s(m,n)\}}\}. \tag{2.50}$$

This method is very economical and its accuracy depends only on the selected resolution of digitized media. See also Appendix C for further discussion. Usually, the Fast Fourier Transform, which needs only $O(\log(MN))$ operations, is called to carry out the numerical computation.

2.3.2 Functions ρ_n

Direct evaluation of function ρ_n for all n is not trivial owing to its definition as the probability density function. On the contrary, a function given as an integral of ρ_n (which can be

interpreted as a probability function) can be easily determined. The second–order intensity function $K(r)$ in Eq. (2.32) represents such functions. Following [Axelsen, 1995, Pyrz, 1994], this function assumes the form

$$K(r) = \frac{A}{N^2} \sum_{k=1}^{N} \frac{I_k(r)}{w_k}, \tag{2.51}$$

where $I_k(r)$ is the number of points (particle centers) within a circle with radius r centered at particle k, N is the total number of particles (fibers) in the sample, A is the sample area and w_k stands for correction factor, which takes into account points outside the sampling area if not included in $I_k(r)$. In principle, w_k is a weighting factor given by, Fig. (2.4),

$$w_k = \frac{\pi r^2}{A'}. \tag{2.52}$$

When a periodic microstructure is considered it equals 1.

Eq. (2.51) suggests that evaluation of K for a given r requires to count the number of points distant by r from all particle centers in the sample. Provided that particle centers are sorted with respect to one coordinate, this task can be accomplished using a very simple projection method with computational complexity $O(N[\log_2(N)+k])$, where $k \leq N$ (see e.g. [Hudec, 1999, Chapter 4]). Evidently, this procedure may perform rather poorly when samples with a very large number of particles are analyzed. However, in applications considered herein it proved to be very efficient.

Knowing the function $K(r)$, the radial distribution function g_2 follows from Eq. (2.32) using numerical differentiation. The two–particle probability density function for an isotropic medium ρ_2 is then found from Eq. (2.30). The required statistical isotropy associated with $K(r)$ presents one of the drawbacks. It therefore desirable to confirm this hypothesis first prior to selecting this function for the description of a random media.

2.3.3 Microstructural statistics for theoretical models of microstructures

The purpose of this section is to test the proposed evaluation techniques for two simple examples of statistically isotropic models of the microstructure – the hexagonal arrangement

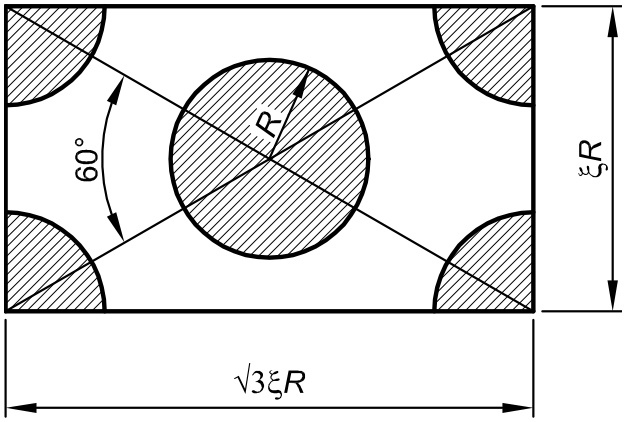

Figure 2.5: Unit cell for hexagonal lattice of fibers

of particles and the model of equal-sized fully penetrable cylinders. Selection of these two microstructures is rather intentional. In fact, the closed form of $K(r)$ is known for both configurations. Also, the closed form of $S_{mm}(r)$ has been found for the model of fully penetrable cylinders. Note that both models assume periodic microstructures.

Hexagonal array of cylinders. The hexagonal arrangement of particles in the matrix is uniquely specified by the periodic unit cell displayed in the Fig. 2.5. The dimensionless constant ξ is given by

$$\xi^4 = \frac{4}{3}\frac{\pi^2}{c_f^2}. \tag{2.53}$$

A simple geometric consideration reveals that function $K(r)$ will experience jumps corresponding to regular spacing of particles denoted by ${}^1r$ for corner fibers and ${}^2r$ for central fibers,

$${}^1r^2 = \xi^2 R^2(3i^2 + j^2), \tag{2.54}$$

$${}^2r^2 = \frac{\xi^2}{4}R^2\left[3(2i+1)^2 + (2j+1)^2\right], \tag{2.55}$$

where $i, j = 0, \ldots, \infty$. Since there are exactly six additional fibers found for every fiber at a

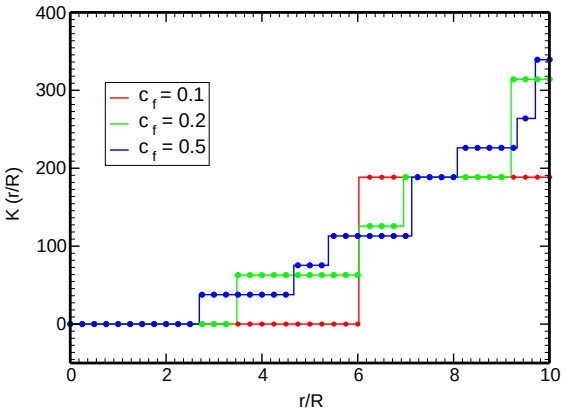

Figure 2.6: Function $K(r)$ for hexagonal packing of fibers

given jump, it follows from Eq. (2.51) that the value of ΔK for every jump reads

$$\Delta K = \frac{6\pi}{c_f} R^2. \tag{2.56}$$

Caution must be exercised when evaluating the function $K(r)$ for an arbitrary r. In particular, one should carefully inspect values ${}^1r$ and ${}^2r$ to avoid taking one step into consideration twice. The resulting curves for different values of c_f appear in Fig. 2.6. The solid lines correspond to the closed form solution while dots denote discrete values obtained numerically.

Fully penetrable cylinders This model assumes that positions of particle centers are totally independent. Thus, the value of $\rho_2(r)$ is constant and equal to ρ^2. Then, $g_2(r) = 1$ and from Eq. (2.32)

$$K(r) = \pi r^2. \tag{2.57}$$

Next, recall that $S_{mm}(\mathbf{x}, \mathbf{x}')$ represents the probability of finding two points $\mathbf{x}$ and $\mathbf{x}'$ randomly thrown into the medium both in the matrix. For fully penetrable cylinders this function corresponds to the probability that union of two cylinders with radius R and centers located in points $\mathbf{x}$ and $\mathbf{x}'$ is not occupied by any other particle center. Such an event can be

described by the Poisson probability distribution (see e.g. [Rektorys, 1995a, p. 662]) with the intensity $\rho\,\Omega_u(\mathbf{x},\mathbf{x}')$,

$$S_{mm}(\mathbf{x},\mathbf{x}') = \exp(-\rho\,\Omega_u(\mathbf{x},\mathbf{x}')). \tag{2.58}$$

For the statistically isotropic medium, this expression reduces to [Torquato, 1991]

$$S_{mm}(r) = \exp(-\rho\,\Omega_u(r)), \tag{2.59}$$

where $\Omega_u(r)$ is the union area of two identical cylinders with radius R and centers separated by distance r. To arrive at the number of particles ρ per unit area (volume) we combine Eqs. (2.17) and (2.38) to write the matrix volume fraction in the form

$$S_{mm}(r=0) = c_m = \exp(-\rho\,\pi R^2) \tag{2.60}$$

Therefore, for a given c_m the above relation readily provides the corresponding value of ρ.

Numerical experiments were performed for twenty different configurations containing 100 particles having a circular radius R. Each configuration was generated purely randomly keeping the matrix volume fraction c_m fixed. The value of S_{mm} was found by placing a template of Fig. 2.2 randomly into a medium. Each value was averaged over 5,000 throws. A procedure analogous to the previous subsection was applied to determine the corresponding values of K. The curves derived from simulations and Eq. (2.57) or (2.59) are displayed in Fig. 2.7. The solid lines were derived by averaging the resulting values over all twenty configurations.

To conclude, results displayed in Figs. 2.6–Fig. 2.7 mark the proposed methods as sufficiently accurate to provide reliable values for selected statistical functions.

2.4 Analysis of real microstructure

In this closing section, the preceding procedures are applied to the real microstructure represented here by the micrograph of Fig. 2.1(b) taken from the bundle of graphite fibers bonded to the polymer matrix. For numerical analysis, the real microstructure is replaced by its

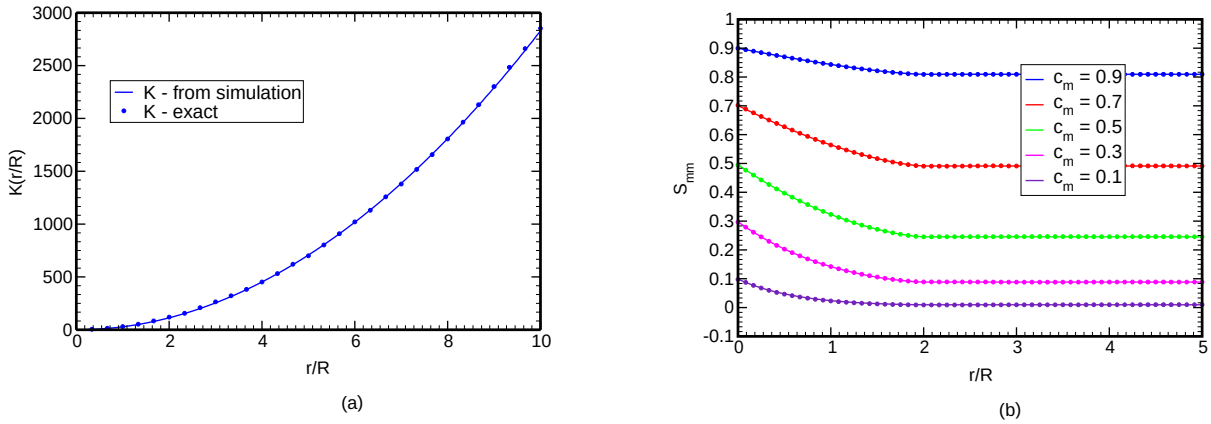

Figure 2.7: Microstructural functions for fully penetrable cylinders.

idealized binary image, Fig. 2.3, which offers rather concise yet more useful notion about the actual arrangement of fibers within a sample.

Before proceeding, the powerful image analyzer LUCIE is called to provide for the basic geometrical information such as the fiber radius, position of all particles in the sample and the fiber volume fraction. At present, the periodicity of microstructure is invoked so the micrograph is assumed to be surrounded by periodic replicas of itself, which indirectly implies ergodicity and statistical homogeneity of the medium. Therefore, the validity of these statistical assumptions should be checked first, see Sections 2.4.1–2.4.2. A number of results derived for the selected statistical descriptors are referenced in Section 2.4.3.

2.4.1 Testing ergodic hypothesis

To test the ergodic hypothesis it is necessary to form the ensemble space $\mathcal{S}$. When sampling individual members of $\mathcal{S}$ we started from three micrographs of the fiber tow taken from three specimens at approximately the same location. Each member of the ensemble was then found through a random cut of a part of a given micrograph subjected to condition of the "same" fiber volume fraction. This condition actually supplements the lack of infinity of

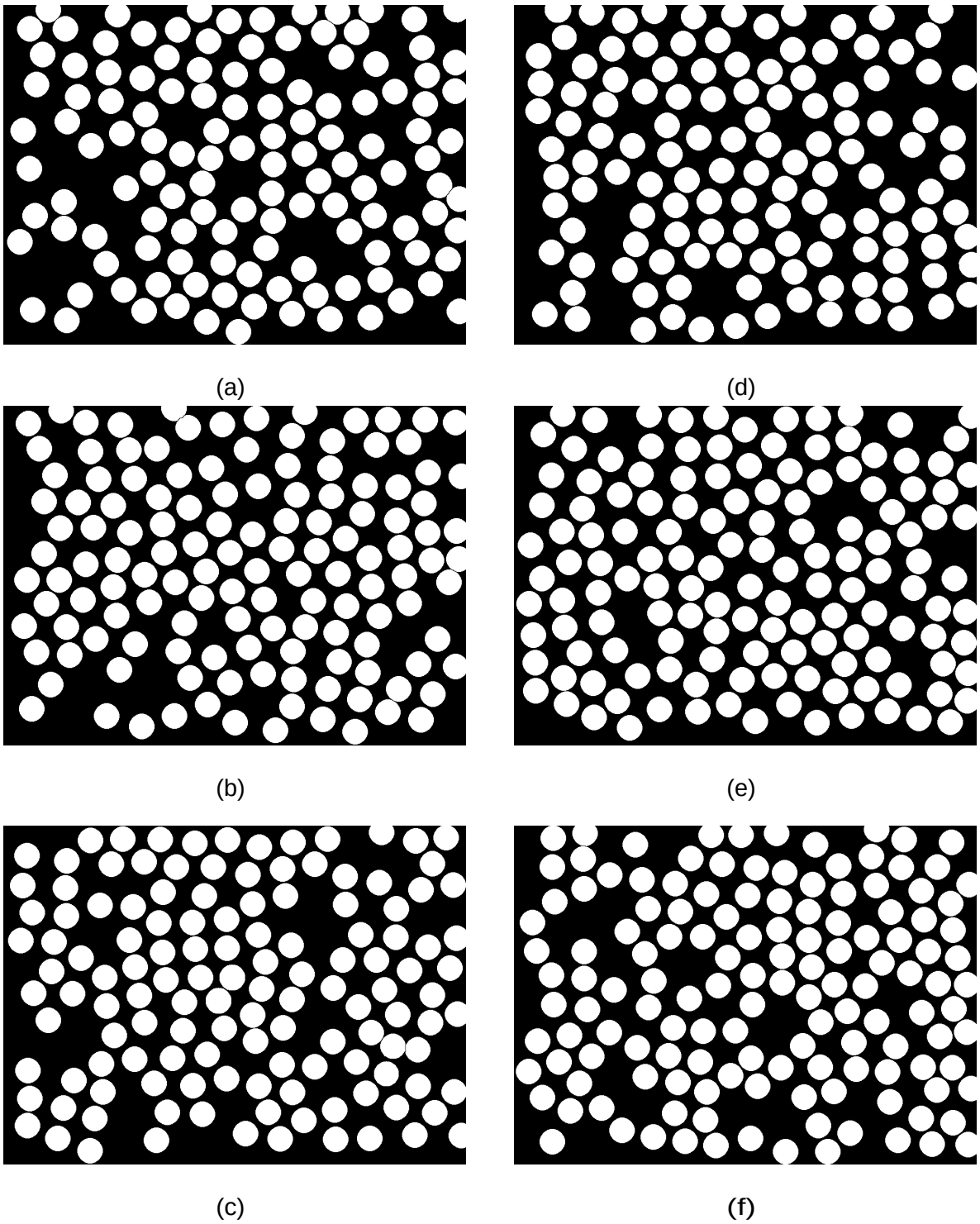

Figure 2.8: Selected members of the sample space

our composite medium. Fig. 2.8 shows six such individuals generated from the micrograph displayed in Fig. 2.3. In view of the above comments we shall only require that

$$c_r = \frac{1}{n}\sum_{i=1}^{n} S_r^i, \qquad r = f, m \ , \tag{2.61}$$

where n is the number of members in the ensemble. Functions S_r^i can be derived by randomly placing a point in the member i in a certain number of times while counting the number of hits in the phase r and then dividing by the total number of throws. When setting the number of throws equal to 500 we found $\overline{S_f} = 0.42$, which agrees well with the average fiber volume fraction $\overline{c_f} = 0.435$. A better agreement can be expected for larger n. Although an ultimate justification of an ergodic assumption would require to prove equality of higher moments as well, we argue that the presented results are sufficient for the medium to be considered as ergodic, providing the medium is indeed statistically homogeneous. In the sense of an ergodic assumption we suggest that a single micrograph can be used hereafter for evaluation of the required statistical descriptors.

2.4.2 Test of statistical isotropy

To check the statistical isotropy of the medium under consideration we plot the distribution of the two-point matrix probability function S_{mm} for a statistically uniform medium as a function of coordinates of points $\mathbf{x}$ and $\mathbf{x}'$, Fig. 2.9(a). These results were derived after 100,000 random throws of the sampling template from Fig. 2.2. Should the material be statistically isotropic (independent of orientation) the variation coefficient $v(\phi)$ of $S_{mm}(\phi)|_{r/R}$ for a given ratio r/R would be equal to zero. Nevertheless, to facilitate the micromechanics analysis addressed in Chapter 3 the material will be treated as statistically isotropic, and the maximum 5% variation evident from Fig. 2.9(b) is taken as an acceptable error of the assumption.

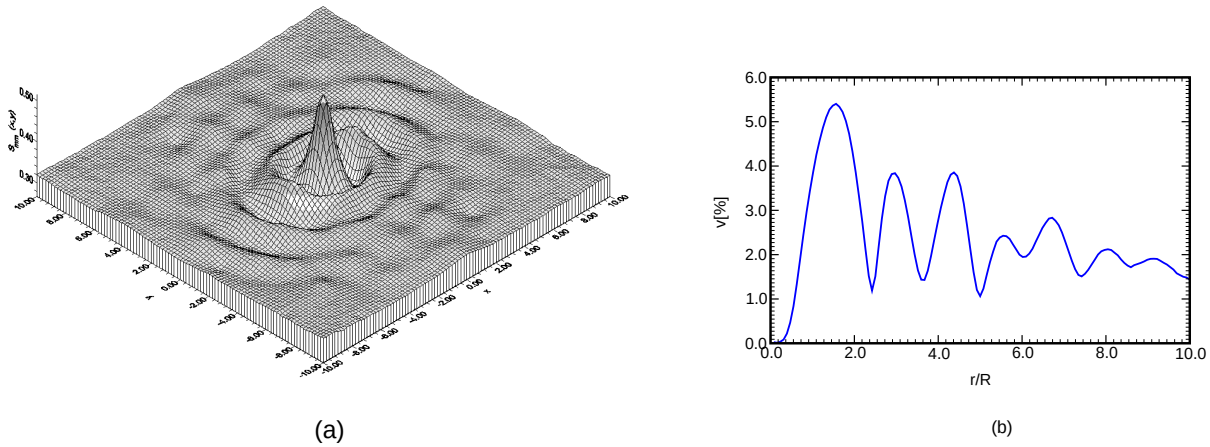

(a) (b)

Figure 2.9: Two-point matrix probability function $S_{mm}(\mathbf{x}-\mathbf{x}^{'})$ and variation coefficient $v(\phi)$ of $S_{mm}(r,\phi)$ plotted as a function of r/R.

2.4.3 Microstructure describing functions

After verifying the statistical assumptions at least to some extent, we may proceed to determine all the microstructure describing functions for the current microstructure.

The two-point probability functions. Apart from Fig. 2.9(a), numerical results are presented only for the ergodic and isotropic medium. Fig. 2.10(a) illustrates the variation of S_{mm} as a function of the number of random throws of the sampling template. It is evident that for the present microstructure 5,000 repetitions are sufficient. Fig 2.10(b) further shows certain unique relationships pertaining to the isotropic and ergodic medium (recall Table 2.1). Clearly, Eq. (2.17) reduces to $S_{rs}(0) = \delta_{rs}c_r$ while Eq. (2.18) becomes $\lim_{\|\mathbf{x}-\mathbf{x}'\|\to\infty} S_{rs}(\mathbf{x},\mathbf{x}') = c_r c_s$. The former relation simply manifests the ergodic hypothesis. Its justification for the present material system is supported by results plotted in Fig 2.10(b). Note that in this particular case the fiber volume fraction was found to be equal to 0.44. The latter one roughly states that two space points $\boldsymbol{x}$ and $\boldsymbol{x}^{'}$ spread far apart ($r = 10R$, Fig. 2.10(b)) are statistically independent. The remaining theoretical relations listed in

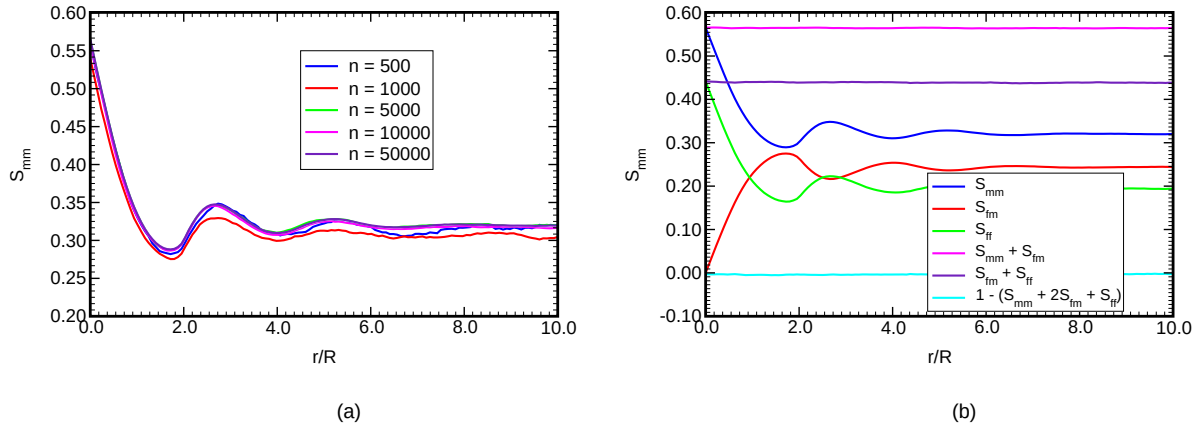

Figure 2.10: Two-point matrix probability $S_{mm}(r)$ and unique relations for the general two-point probability function $S_{rs}(r)$.

Table 2.1 agree well with the numerical predictions, which further confirms justly used assumptions regarding the statistical isotropy and ergodicity for the present system. Methods arising from the analysis of digitized media offer another, computationally more attractive way to evaluate the desired statistics. They either use a discrete counterpart to integral expressions (2.11)–(2.12) (recall Eqs. (2.45), (2.48)) which requires only point by point integration. Or, when an ergodic assumption applies, an integral formula given in form of correlation, Eq. (2.46), can be exploit. In view of Section 2.3.1, this approach employs the Fast Fourier Transform (FFT) to evaluate Eq. (2.49). Inverse FFT is then applied to solve Eq. (2.50). Operations based on the FFT are usually build on various public-domain packages optimized for a given computer. These definite advantages make this particular approach rather appealing, see also Table 2.2. The final comment reconciles the true behavior of function S_{rs} and its periodic character which arises from Eq. (2.50). Recall that with $r \longrightarrow \infty$ $S_{rs} \longrightarrow c_r c_s$, Eq. (2.18). Therefore, the sample size should be sufficiently large to comply with this property. As illustrated in Fig. 2.12(b) this requirement is certainly fulfilled for the present samples shown in Figs. 2.3 and 2.11. Fig. 2.12(a) illustrates a variation of the two–point matrix probability function $S_{mm}(r)$ derived in turn from Eqs. (2.45), (2.48),

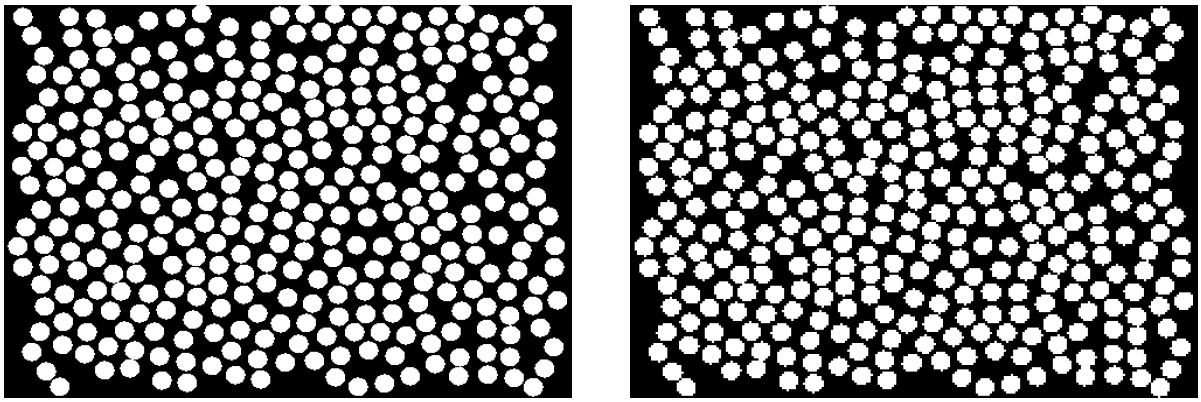

Figure 2.11: Idealized binary images of Fig. 2.1(b); (a)–resolution 488x358 pixels, (b)–resolution 244x179 pixels.

Table 2.2: CPU time in seconds required to evaluate function S_{mm}

Method	**Bitmap resolution**		
	976 × 716	488 × 358	244 × 179
Direct with periodicity	×	9095.27	446.03
Direct without periodicity	×	5200.07	238.62
FFT based	6.24	1.54	0.37

(2.50) assuming the bitmap of Fig. 2.3. While the curves derived from Eqs. (2.48) and (2.50), which presume periodic microstructures, are in perfect match, results from Eq. (2.45) deviate. It is clear that a higher resolution of a digitized medium inevitably increases the required computational time. Table 2.2. indicates that lowering the degree of resolution provides a noticeable improvement in terms of the computational efficiency. Encouraging results are plotted in Fig. 2.12(b) suggesting that even at low resolutions a reasonable match with the "exact" solution (the highest possible resolution) can be anticipated. Note that all results were initially derived for a statistically homogeneous ergodic medium. To make them comparable with former predictions, a sampling template was used again to average

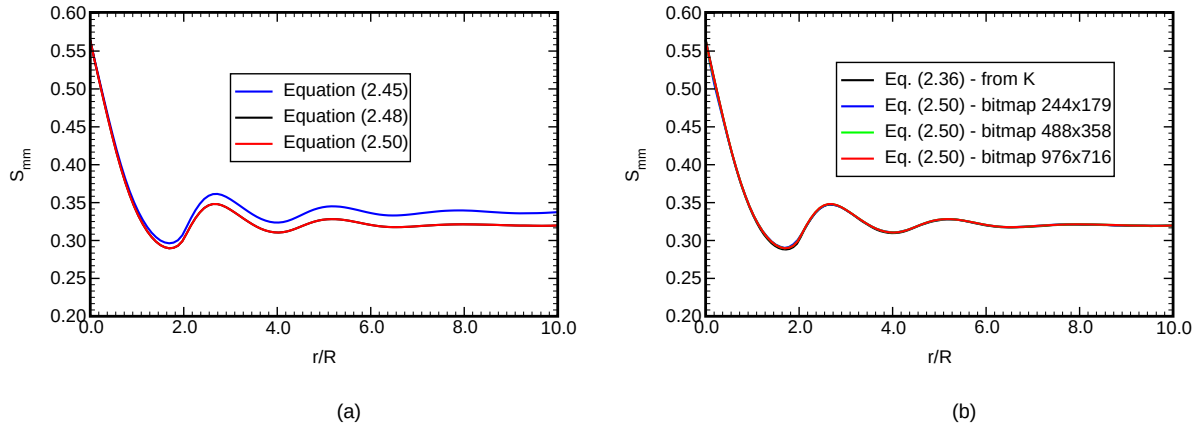

Figure 2.12: Two-point matrix probability $S_{mm}(r)$ derived for a digitized medium.

values for a given radius, thus arriving at a statistically isotropic medium. As evident from Fig. 2.12(b), both approaches provide identical results. Similar conclusions can be drawn for a statistically homogeneous medium by inspecting Fig. 2.13, which shows distributions of variation coefficient $v(\phi)$ as a function of r/R for selected binary images of the present composite system (see Figs. 2.3 and 2.11).

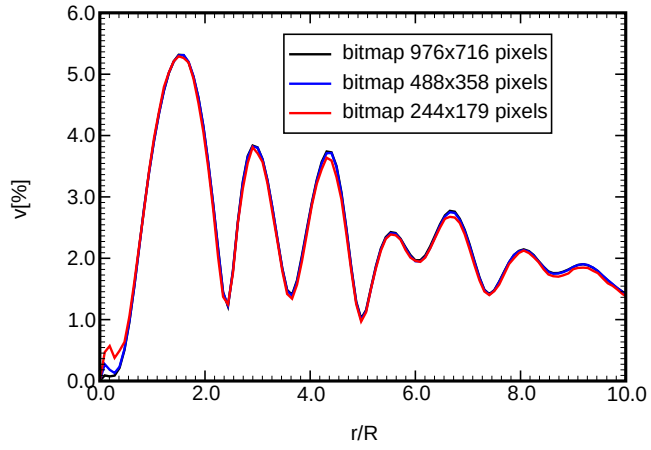

Figure 2.13: Distributions of variation coefficient $v(\phi)$ of $S_{mm}(r, \phi)$ for several digitized media

The two-particle probability density based functions. First, we turn our attention to the second order intensity function $K(r)$. Recall that the number of repetitions needed for its evaluation now corresponds to the number of fibers within the sampling area, since the center of the sampling template to count the number of points for a given radius r is now placed in turn into centers of individual fibers only. Its determination is thus simple and for the moderate number of particles in a sample very efficient.

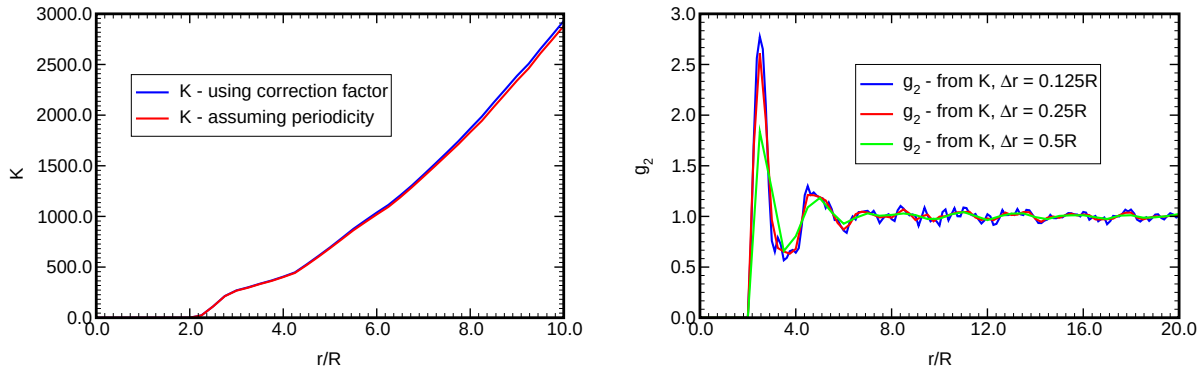

Figure 2.14: Second order intensity function $K(r)$ and radial distribution function $g_2(r)$

Evaluation of K for both the stand-alone micrograph and the periodic one are examined. The resulting curves appear in Fig. 2.14(a). Deviation of both curves suggests that the results obtained using the correction factor are partially biased, especially for larger values of r. Even more severe difference is expected for micrographs with smaller number of particles.

To complete our exposition to the selected set of statistical descriptors we show a variation of the pair distribution function $g_2(r)$ obtained by the numerical differentiation of the second order intensity function $K(r)$ employing the central difference formula. Individual curves on Fig. 2.14(b) correspond to various step sizes used when solving Eq. (2.32). Fig. 2.14(b) indicates two major flaws associated with Eq. (2.32). First, the value of $g_2(r)$ is strongly dependent on the selected step size. A rather small step size is required to capture accurately the critical region. In contradiction, reducing the step size Δr results in substantial

oscillation of this function. In addition, the amplitude of these oscillations does not become negligible even for large r.

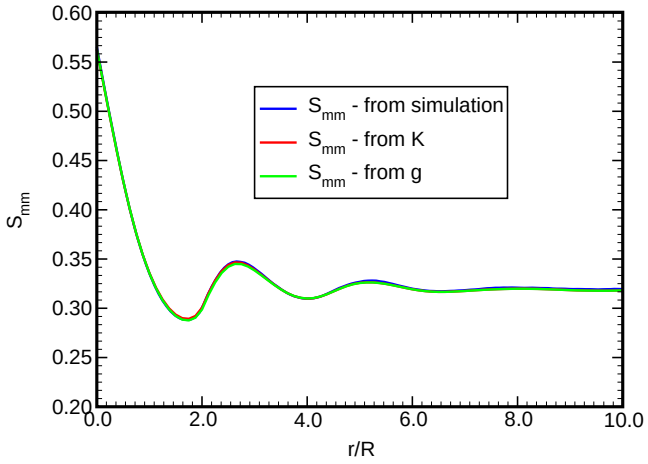

Figure 2.15: The two-point matrix probability function

To conclude, we inspect the unique connection (2.36) between S_{mm} and functions $K(r)$ and $g_2(r)$ for the isotropic and ergodic medium. Integrals (2.41, 2.42) are evaluated numerically using adaptive Simpson's integration scheme (see [Burden and Faires, 1989]) with the prescribed tolerance 10^{-4}. Fig. 2.15 shows the variation of function S_{mm} derived from various approaches. Coincidence of individual curves is evident. Note that procedure which requires solution of (2.36) for a given distribution of $K(r)$ is considerably more efficient then the one based on simulations, and therefore preferable.

Chapter 3

LOCAL AND OVERALL RESPONSE OF RANDOM COMPOSITES VIA PERIODIC FIELDS

The purpose of this chapter is to introduce a simple micromechanics based approach to the analysis of random composites. Owing to the complexity of the microstructure, recall Fig. 1.2, the analysis is usually left to rely on incomplete geometrical information about the composite microstructure. The problem is not successfully resolved even when considering a large sample of composite as such displayed in Fig. 1.1. Instead, it appears preferable to exploit various statistical descriptors discussed in detail in Chapter 2.

An essential ingredient of the present model applicable in both the elastic and inelastic regimes is a carefully selected material representative volume element (RVE) replacing the real microstructure. Such a RVE is represented here by a periodic unit cell (PUC) consisting of a small number of particles, which statistically resembles the actual composite. For an early study on this subject we refer the reader to [Povirk, 1995]. A definite choice of the number of particles within a unit cell depends on a given problem one wish to analyze.

A number of ways can be used to accomplish this task. Here, we offer a simple approach based on the microstructural statistics. In particular, the PUC is found from a certain optimization procedure. A random character of the microstructure is accounted for through the two-point probability and the second order intensity functions (Section 2.3) introduced into an objective function. The procedure is outlined in Section 3.1. Results are presented for the graphite-fiber tow impregnated by the polymer matrix.

A number of theoretical problems, generally beneficial to the designer, are selected to test applicability of the present approach. Section 3.2 is concerned with numerical evaluation of

effective mechanical properties of composites with periodic microstructures. Contribution due to local eigenstrains to overall response is studied in Section 3.3. Here we admit only thermal changes and viscoelastic deformations. Extension to other deformation modes is straightforward. The interested reader may consult the work by [Michel et al., 1999] for details on this subject.

3.1 Construction of the periodic unit cell

In this section we are concerned with one of the major goals of this work: determination of the periodic unit cell, which is statistically equivalent to the original microstructure. In achieving this, the knowledge about material's statistics acquired in Chapter 2 is used. In particular, the PUC is constructed by matching a selected microstructure describing function of the real microstructure and the unit cell. To that end, an optimization procedure based on the method of least squares is implemented. The optimization problem then reduces to the minimization of an objective function involving the selected statistical descriptor. Although the required statistical information can be provided by any function presented in previous sections, the proper choice of a statistical descriptor may result in significant improvement of the optimization process.

The process of finding the minimum value of the objective function is divided into two steps: finding the optimal positions of fibers for fixed dimension of the unit cell and then generating the optimal dimensions of the unit cell. While the second step of this procedure represents an elementary one-dimensional minimization problem, the solution of the first problem requires the minimization of a multi-dimensional, multi-modal function with a large number of local minima. A variety of stochastic algorithms is described in Section 3.1.2. Section 3.1.4 offers some additional improvements to optimization algorithms. Resulting unit cells are introduced in Section 3.1.5.

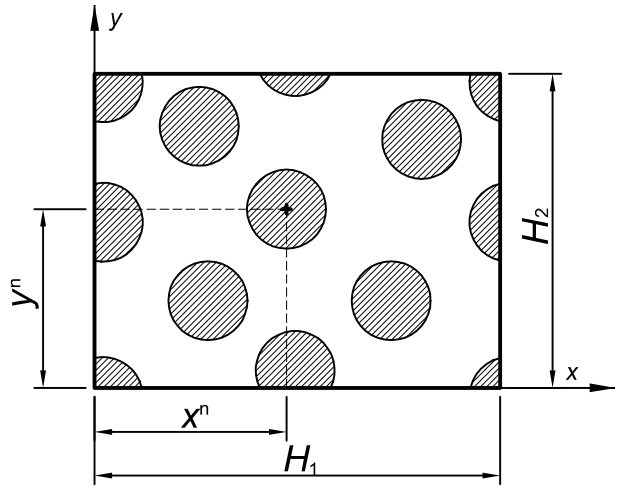

Figure 3.1: Geometry of the periodic unit cell

3.1.1 Objective function and problem definition

Consider a periodic unit cell consisting of N particles displayed in Fig. 3.1. The geometry of such a unit cell is determined by dimensions H_1 and H_2 and the x and y coordinates of all particle centers. The objective is to keep material's statistics of both the PUC and the actual composite as much similar as possible. At present, the particle locations together with an optimal ratio of cell dimensions H_1/H_2 are found by minimizing an objective function involving the second order intensity function $K(r)$

$$F(\mathbf{x}^N, H_1, H_2) = \sum_{i=1}^{N_m} \left(\frac{K_0(r_i) - K(r_i)}{\pi r_i^2} \right)^2, \tag{3.1}$$

where $\mathbf{x}^N = \{x^1, y^1, \ldots, x^N, y^N\}$ stores the positions of particle centers of the periodic unit cell, x^i and y^i correspond to the x and y coordinates of the i-th particle, H_1 and H_2 are the dimensions of the unit cell, $K_0(r_i)$ is the value of K corresponding to the original media evaluated at the position r_i and N_m is the number of points, in which both functions are evaluated.

The choice of function $K(r)$ for the optimization problem is primarily attributed to its simplicity and a very rapid evaluation for a reasonable number of particles N. In addition, the

selected form of the objective function F, Eq. (3.1), serves directly as a "natural" penalization when particles happen to overlap. Therefore, no additional algorithmic labor necessary for avoiding unacceptable solutions [Povirk, 1995] is needed if the material is formed by impenetrable particles.

The minimization of objective function (3.1) is performed in two steps, where each step corresponds to a single optimization problem. It proved advantageous to start from an optimal spatial distribution of particle centers for a given set of cell dimensions. The desired ratio of cell dimensions then follows from a separate optimization problem. Hence, the following optimization problem is solved first

Optimal fiber configuration. For a given number of fibers N, dimensions of a unit cell H_1 and H_2 and values of the original function $K_0(r)$ evaluated at points $r_i,\ i = 1, \ldots, N_m$ find the configuration of particle centers $\mathbf{x}^N(H_1, H_2)$ such that:

$$\mathbf{x}^N(H_1, H_2) = \arg\min_{\mathbf{x}^N \in \mathcal{S}} F(\mathbf{x}^N, H_1, H_2), \tag{P1}$$

where $\mathcal{S}$ denotes a set of admissible vectors $\mathbf{x}^N$.

Several alternatives are acceptable to define a set $\mathcal{S}$ of admissible solutions. When studying periodic microstructures the components of vector $\mathbf{x}^N$ can take arbitrary values so the problem is treated as an *unconstrained* one. If desirable one may avoid the presence of two materials at the boundary by restricting the positions of fibers such that the components of vector $\mathbf{x}$ satisfy the following condition

$$0 \le x^i \le H_1, \quad 0 \le y^i \le H_2, \quad i = 1, \ldots, N. \tag{3.2}$$

The minimization problem then becomes *bound-constrained*. Finally, as discussed in Section 3.1.3 the *impenetrability condition* can be imposed. With some additional tricks this substantially improves performance of the optimization procedure.

After solving the above problem, we are left with only two unknown parameters, H_1 and H_2, to be determined. Maintaining the same fiber volume fraction c_f for both the periodic unit cell and original microstructure imposes an additional constraint on a set of unit cell dimensions. The second optimization problem thus reduces to the minimization of the objective function (3.1) with respect to the ratio $\eta = H_1/H_2$

Optimal ratio H_1/H_2 . For known values of $\mathbf{x}^N(\eta)$ and for the fixed volume fraction of phases, find the ratio η^N such that:

$$\eta^N = \arg \min_{\eta \in \langle \eta_a ; \eta_b \rangle} F(\mathbf{x}^N(\eta)), \tag{P2}$$

where values η_a and η_b should be chosen to cover all the reasonable dimensions of the unit cell.

The solution of problem (P2) can be obtained through the *Golden Section search* method [Press et al., 1992, Chapter 10.1]. In a nutshell, starting from an initial triplet of points a, b, c this method is based on generating a new point in locations, which divide intervals $\langle a; b \rangle$ or $\langle b; c \rangle$ in some prescribed ratio – Golden section. The new point then replaces one of the points a, b, c according to its function value and position. The essentials of this method are summarized in Algorithm 3.1.

For all computations performed herein, the parameters η_a and η_b were set to 1.0 and 2.0, respectively. To check the solution admissibility we recall the properties of function $K(r)$ evaluated for the hexagonal packing of fibers. The results presented in Section 2.3.3 imply that every regularity of microstructure generates a jump of function $K(r)$ with the amplitude corresponding to the number of fibers located at the same distance from a given particle. Therefore, for the side ratio $\eta = 1.0$ as well as for $\eta = 2.0$ and e.g. for values of $r = iH_1,\ i = 1, \ldots, \infty$, four other fibers are always found, while this situation does not occur for the intermediate values of η. Since function $K(r)$ relevant to the original microstructure does not experience such jumps (see Fig. 2.14) the value of function F for $\eta \in (1; 2)$ should be always less than for the interval endpoints.

```
1 supply values a < b < c such that f(a) > f(b) ∧ f(c) > f(b)
2 while((c − a) < ϵ) {
3    ddetermine new point d
4    if (f(d) < f(b))
5       b = d, update a, c with respect to step 1
6    else
7       if(d < b) a = d
8       else c = d
9 }
```

Algorithm 3.1: Golden Section search

Step 1 The initial points a and b corresponds in the present context to values η_a and η_b in (P2) and the function value $f(\cdot)$ represents here the minimum value of function F found for the optimization problem (P1) for a given side ratio.

Step 3 The new point is located in the larger of two intervals $\langle a; b\rangle$ and $\langle b; c\rangle$, its distance from the point b is $(3 - \sqrt{5})/2$ times the length of a larger interval.

While solving the above problem is relatively simple, the solution to the first problem (P1) requires to locate the global minimum of multi-dimesional function, which is far from clean but rather rugged with a large number of plateaus and local minima. To manifest the problem complexity, an admissible unit cell consisting of 10 fibers together with an example of the objective function F is shown in Fig. 3.2. Coordinates x^1 and y^1 in Fig. 3.2(b) represent locations of the filled fiber center. Positions of remaining fibers are fixed. The minimum of function F for the present configuration is marked by a hollow circle. As

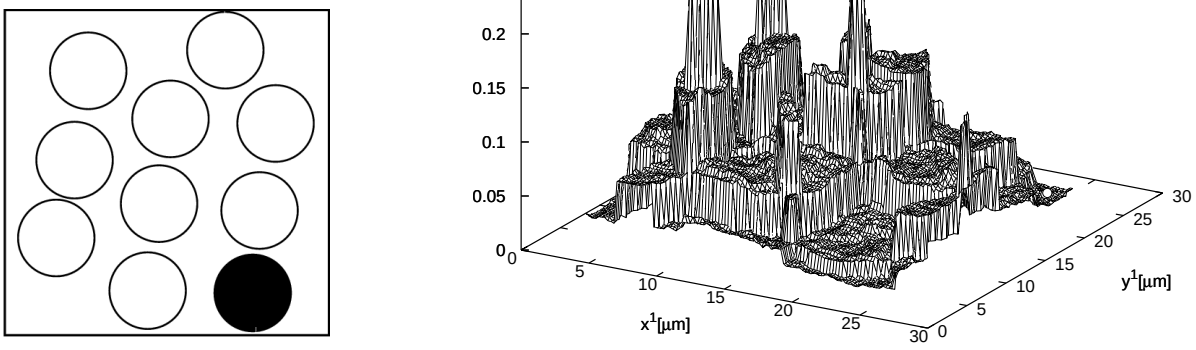

Figure 3.2: An admissible unit cell

suggested in [Matouš et al., 2000] and [Lepš and Šejnoha, 2000] an optimization problem of this kind can be tackled very efficiently with the help of problem solving systems based on principles of evolution such as genetic algorithms or simulated annealing methods. A list of efficient algorithms collectively called the stochastic optimization methods is given in the next section.

3.1.2 Stochastic optimization methods

A variety of genetic algorithms based *Evolution programs* has been developed in the last few decades. For thorough discussion on this subject we refer the interested reader to [Goldberg, 1989], [Michalewicz, 1992], [Beasley et al., 1993] and [Kvasnička, 1994], among others. Here, we do not attempt to provide any major break-through in evolutionary programming but rather effectively exploit up to date knowledge to attain the goal we set.

Principle of genetic algorithms

Genetic algorithms (GAs) are formulated using a direct analogy with evolution processes observed in nature, a source of fundamental difference between traditional optimizers and GAs. In contrast to traditional methods, genetic algorithms work simultaneously with a population of individuals, exploring a number of new areas in the search space in parallel,

thus reducing a probability of being trapped in a local minimum. As in nature, individuals in a population compete with each other for surviving, so that fitter individuals tend to progress into new generations, while the poor ones usually die out. This process is briefly described in Algorithm 3.2. Algorithm 3.2 provides basic steps of a single GA cycle; reproduction phase

---

1 $t = 0$
2 generate P_0, evaluate P_0
3 **while** (**not** termination-condition) {
4 $t = t + 1$
5 select M_t from P_{t-1} (apply sampling mechanism)
6 alter M_t (apply genetic operators)
7 create P_t from M_t and evaluate P_t (insert new individuals into P_t)
8 }

Algorithm 3.2: Principle of the genetic algorithm

(step 5), recombination (step 6), and selection of a new population (step 7). In paragraphs to follow, we first explore mechanisms guiding selections of new individuals, which undergo genetic process (step 5), and then proceed with basic operators controling the step 6. Steps 5 and 7 will be explained in more details when formulating various algorithms we tested.

Sampling mechanisms

Sampling mechanism facilitates the reproduction step of the GA (step 5 in Algorithm 3.2). In principle, individuals selected for reproduction are copied to the "mating" pool according to their relative performance reffered to as their "fitness", or "figure of merit". In case of function optimization, it simply equals the function value or rather its inverse when solving minimization problem. An expected number of copies each individual should receive in the

mating pool M_t is given by

$$e_i = \frac{s_i}{\sum_{j=1}^{P} s_j} M, \qquad s_i = \frac{1}{\delta + f_i}, \qquad f_i \geq 0 \tag{3.3}$$

where P is the number of individuals in the population, M is the number of individuals in a mating pool M_t, and f_i is the function value associated with the i-th individual; $s_i = f_i$ when solving maximization problem. Parameter δ is a small positive number which prevents division by zero. This procedure is called *sampling mechanism*. The most popular ones are reviewed in the sequel.

Fitness scaling. Usually it is not desirable to sample individuals according to their raw fitness. In such a case the best individuals may receive a large number of copies in a single generation. In other words, increasing the selection pressure decreases the population diversity. To compress the range of fitness a *linear scaling* (shifting) of the fitness function is incorporated into sampling procedures [Goldberg, 1989]. Then, the relation between the raw fitness s and the scaled fitness s' is simply $s' = as + b$. To determine constants a and b we require the average raw fitness s_{avg} and scaled fitness s'_{avg} to be the same. The second condition is then provided by setting the value of maximal scaled fitness to $s'_{\text{max}} = C_{\text{mult}} s'_{\text{avg}}$, where $C_{\text{mult}} \in \langle 1.2; 2 \rangle$.

Roulette wheel selection. The method starts by setting the probability of selecting i-th individual to $p_i = s'_i / \sum_{j=1}^{P} s'_j$. Next, a real number p with uniform distribution on the interval $\langle 0; 1 \rangle$ is generated and then the first individual with its *cumulative probability* $\sum_{i=1}^{j} p_i$ exceeding p is inserted into the mating pool. This procedure is repeated until the mating pool is full. More details can be found in [Goldberg, 1989, Kvasnička, 1993].

Note that this procedure is often described with analogy to a single spin of a roulette wheel with one marker, where parts of the wheel corresponding to individual members are allocated with respect to the value p_i.

Stochastic universal sampling (SUS). Stochastic universal sampling is a generalization of previous selection method proposed by Baker in [Baker, 1987]. The standard roulette wheel is marked with equally spaced pointers indicating the happy individual selected for reproduction. A number of pointers indicates a number of desired individuals used for reproduction, which are again obtained by the single spin of a roulette wheel.

Remainder Stochastic Independent Sampling (RSIS). [Baker, 1987] This method allocates individuals according to the integer part of their e_i. The remaining places in a population are then sampled according to their fractional part representing here the probability of selection. In particular, the fractional part of each individual is checked against a real number r uniformly distributed over the $\langle 0; 1\rangle$. If greater, the individual is added to the mating pool and its fractional part is set equal to zero. If not, move to the next individual. These steps are repeated until the number of individuals in the mating pool equals M.

To make our exposition complete we briefly mention two selection methods which are not based on the expected number of copies in mating pool each individuals should receive. The main advantage of this approach is that it principally prevents the best individuals from causing the premature convergence of the whole population.

Tournament selection. Whenever an individual is to be selected to the mating pool, two individuals are picked randomly from the original generation. Then the individual with higher fitness is copied into the mating pool. This procedure is repeated until the mating pool is full. More details about this procedure can be found in [Beasley et al., 1993].

Normalized geometric ranking. In this method, the probability of individual's selection is based on its *rank* or *position* in the population rather than on the value of fitness. As described in [Houck et al., 1995], probabilities are assigned to each individual exponentially and are normalized to provide the cumulative probability of selection equal to 1. Thus, the

probability of selection of i-th individual is

$$p_i = q'(1-q)^{r-1},$$

where q is the probability of selecting the best individual in the population , r is the rank of i-th individual with respect to its raw fitness, and $q' = q/(1-(1-q)^P)$.

Although a proper selection scheme may quite significantly influence an ultimate performance of the GA, there is no firm evidence proving the superiority of one particular sampling method over the others.

Genetic operators

Breeding is the essential force driving evolution of each species. Mating process, in which two parents combine their good characteristics to produce a better offspring, is accomplished in GAs through various "cross-breeding" and "mutating" operators referred to as *genetic operators*. These operators work on a set of solution vectors $\mathbf{x}^N$ transformed into a sequence of genetic information - *chromosome*. Individual variables are then termed *genes*. This framework is usually introduced to distinguish between the search and representation spaces.

In its classical version [Goldberg, 1989], the genetic algorithm was limited exclusively to binary representation of chromosomes with only two basic operators, single-point crossover and mutation, being used. The binary representation of searched variables , however, suffers from various drawbacks such as a precision limitation. For example, coding a high-precision real number may lead to binary strings of size which essentially prevents the GA from successful implementation. This problem becomes particularly important when the search space is formed by high-precision continuous parameters, since a high-precision requirement usually implies a very large representation space. In such a case the binary genetic algorithm performs rather poorly.

To avoid this shortcoming we turn our attention to a floating-point representation of genes [Michalewicz, 1992]. This step brings a number of advantages. First of all, using real numbers easily allows representation to the machine precision. In addition, the search operators work

directly in the search domain thus no mapping between the representation space and the search space is required. This is a direct consequence of the floating point implementation, where each chromosome vector is coded as a vector of floating point numbers, of the same length as the solution vector. Particularly, each individual – a configuration of particles in the unit cell – is represented by a real-valued chromosome $\mathbf{X} = \{x_1, \ldots, x_{2N}\}$. Individual components of this vector are related to the actual fiber centers as follows

$$x_{2i-1} = x^i \quad \text{and} \quad x_{2i} = y^i \quad \text{for} \quad i = 1, \ldots, N,$$

where N is the number of fibers within the unit cell, x^i and y^i represent the x and y coordinate of i-th particle.

Moreover, different representation of genes calls for the suitable choice of genetic operators. Michalewicz in [Michalewicz, 1992, Michalewicz et al., 1994] proposed a group of real-valued genetic operators which are formulated for the convex search space $\mathcal{S}$, so they can be directly used for the solution of considered problem. The description of these operators follows.

Let L_i and U_i represent the lower and upper bound for each variable x_i, respectively. Further assume that vector $\mathbf{X}$ represents a parent, whereas vector $\mathbf{X}'$ corresponds to an offspring; $u(a, b)$ is a real number and $u[a, b]$ is an integer number with uniform distribution defined on a closed interval $\langle a; b\rangle$. The following operators can be now defined:

Uniform mutation: Let $j = u[1, 2N]$ and set:

$$x_i' = \begin{cases} u(L_i, U_i), & \text{if } i = j \\ x_i, & \text{otherwise} \end{cases}$$

Boundary mutation: Let $j = u[1, 2N]$, $p = u(0, 1)$ and set:

$$x_i' = \begin{cases} L_i, & \text{if } i = j, p < .5 \\ U_i, & \text{if } i = j, p \geq .5 \\ x_i, & \text{otherwise} \end{cases}$$

Non-uniform mutation: Let $j = u[1, 2N]$, $p = u(0, 1)$ and set:

$$x_i' = \begin{cases} x_i + (L_i - x_i)f(t), & \text{if } i = j, p < .5 \\ x_i + (U_i - x_i)f(t), & \text{if } i = j, p \geq .5 \\ x_i, & \text{otherwise} \end{cases}$$

where $f(t) = u(0, 1)(1 - t/t_{max})^b$, t is the current generation, t_{max} is the maximum number of generations and b is the shape parameter. This operator allows for a local tuning as it searches the space uniformly initially and very locally at later stages.

Multi-non-uniform mutation: Non-uniform mutation applied to all variables of $\mathbf{X}$.

Simple crossover: Let $j = [1, 2N]$ and set:

$$x_i' = \begin{cases} x_i, & \text{if } i < j \\ y_i, & \text{otherwise} \end{cases}$$

$$y_i' = \begin{cases} y_i, & \text{if } i < j \\ x_i, & \text{otherwise} \end{cases}$$

Simple arithmetic crossover: Let $j = u[1, 2N]$, $p = u(0, 1)$ and set:

$$x_i' = \begin{cases} px_i + (1 - p)y_i, & \text{if } i = j \\ x_i, & \text{otherwise} \end{cases}$$

$$y_i' = \begin{cases} py_i + (1 - p)x_i, & \text{if } i = j \\ y_i, & \text{otherwise} \end{cases}$$

Whole arithmetic crossover: Simple arithmetic crossover applied to all variables of $\mathbf{X}$.

Heuristic crossover: Let $p = u(0, 1)$ and set:

$$\mathbf{X}' = (1 + p)\mathbf{X} - p\mathbf{Y}$$

$$\mathbf{Y}' = \mathbf{X}$$

where $\mathbf{X}$ is better individual than $\mathbf{Y}$ in terms of fitness. If $\mathbf{X}' \notin \mathcal{S}$, then a new random number p is generated until the feasibility condition ($\mathbf{X}' \in \mathcal{S}$) is met or the maximum allowed number of heuristic crossover applications is exceeded.

Now when the principal steps of genetic algorithms are introduced we proceed with several specific examples of genetic algorithms. We describe them in turn by referencing individual steps of Algorithm 3.2.

Genetic algorithm I (GA I)

We begin with the most simple one usually termed as *Steady State GAs*. Reproduction is implemented through the weighted roulette wheel and only one or two offspring are created within each generation. For better understanding we now review the relevant steps:

Step 5 By spinning the roulette wheel select the r individuals from population P_{t-1} required for mating (one individual for mutation, two individuals when the crossover operator is applied). These individuals are temporarily stored in the mating pool M_t. Linear scaling is used to reduce a common threat of premature convergence to a local optimum.

Step 6 Altering M_t by applying either crossover or mutation operators. In our case, the mutation operators are used twice as often as the crossover operators.

Step 7 Based on a number of new offspring created select a corresponding number of individuals from P_{t-1} to die using the inverse roulette wheel. Insert new offspring into P_{t-1} to create P_t.

Genetic algorithm II (GA II)

This algorithm closely resembles the simple genetic algorithm described in [Goldberg, 1989] with only minor changes. To reduce statistical errors associated with the roulette wheel

selection the *Remainder Stochastic Independent Sampling* procedure is employed in this case. As for **GA I** we now review the important steps of Algorithm 3.2:

Step 5 By applying the **RSIS** sample individuals from P_{t-1} and copy them into the mating pool M_t. Note that precisely P individuals are selected for reproduction. This sampling method thus falls into category of preservative and generational selections according to the classification of [Michalewicz, 1992]. Similar actions as in **GAR I** are taken to deal with the premature convergence.

Step 6 Genetic operators are applied to *all* individuals in M_t. Each operator is used in a prescribed number of times depending on the population size, and new individuals are placed into a temporary population P'_t. Parents for breeding are selected uniformly.

Step 7 Create a new population P_t by successively replacing the worst individual from P_{t-1} by individuals from the temporary population P'_t.

Genetic algorithm III (GA III)

This algorithm is essentially a replica of the Michalewicz modGA algorithm presented in [Michalewicz, 1992, p. 59]. It employs the *stochastic universal sampling mechanism* since it allows selection of arbitrary number of individuals to the mating pool by a single wheel spinning. This is particularly appreciable when applying the modGA, which is characterized by following steps:

Step 5a Using the **SUS** select a subset of n individuals from P_{t-1} for reproduction and copy them to M_t. Note that each member of M_t can appear only once in the reproduction cycle.

Step 5b Again using the **SUS** select exactly $P - n$ individuals from P_{t-1} and copy them to a new population P_t.

Step 6 Select uniformly parents from M_t to produce exactly n offsprings (as in **GAR II**, but in this case the genetic operators act only on n individuals stored in the mating pool).

Step 7 Add new offsprings to population P_t.

Hybrid genetic algorithm (HGA)

GAs are generally very efficient in finding promising areas of the searched solution. On the other hand, they may perform rather poorly when shooting for the exact solution with a high degree of precision (premature convergence, convergence to a local minimum, etc.). Therefore it appears logical to combine GAs exploring the search space initially with a deterministic optimizer exploiting promising solutions locally.

As is natural for GAs, this procedure can be implemented in a number of ways. When experimenting with this approach, various ideas suggested up to date were combined, which eventually led to a reliable and efficient algorithm. It works with relatively small population sizes, which makes computationally feasible to restart the genetic algorithm after a given convergence criterion is met. Each restart is associated with a certain number of new members entering the initial population to maintain a sufficient diversity among chromosomes. Consequently, mutation operators can be excluded from reproduction. Individual steps of this algorithm are now discussed in a sequel:

Step 2 Randomly generate a small population.

Steps 5&6 Perform standard genetic operations until convergence or the maximum number of generations exceeded. To select chromosomes for reproduction *stochastic tournament selection* scheme is applied. Only crossover operators are used.

Step 7a Select n best individuals for local search. We adopt the *Dynamic Hill Climbing* method of Yuret [Yuret, 1994] to seek for the desired optimum with a starting point provided by the GA. When the local optimizer converges copy new individuals into P_t.

Step 7b Add $P - n$ randomly generated individuals to fill population P_t. This ensures diversity among chromosomes. Goto step 5 and restart the GA.

```
1  T = T_max, t = 0
2  generate P_0, evaluate P_0
3  while (not termination-condition) {
4     counter = success = 0
5     while( counter < counter_max ∧ success < success_max) {
6        counter = counter + 1, t = t + 1
7        select operator O
8        select individual(s) I_t from P_t
9        modify I_t by O
10       select individual(s) I'_t from P_t
11       p = exp((F(I'_t) − F(I_t))/T)
12       if (u(0,1) ≤ p) {
13          success = success + 1
14          insert I_t into P_t instead of parents
15          evaluate P_t
16       }
17    }
18    decrease T
19 }
```

Algorithm 3.3: Augmented Simulated Annealing

Augmented simulated annealing (AUSA)

When talking about stochastic optimization algorithms, it would be unfair not to mention another popular method using random choice to explore the solution space, namely the *Augmented simulated annealing method* presented by [Mahfoud and Goldberg, 1992]. This method effectively exploits the essentials of GAs (a population of chromosomes, rather than a single point in space, is optimized) together with the basic concept of simulated annealing method guiding the search towards minimum energy states.

If we wish to put GAs and the **AUSA** on the same footing, we may relate the **AUSA** to a group of *Steady state* and *On the fly* methods [Michalewicz, 1992], in which offspring replace their parents immediately. The replacement procedure is controlled by the Metropolis criterion, which allows a worse child to replace its better parent with only a certain probability. The probability of accepting a worse solution is reduced as the procedure converges to the "global" minimum. For proper implementation of the **AUSA** refer to Algorithm 3.3.

Step 7 It is recommended to choose mutation operators with much higher probabilities than crossovers. In [Kvasnička, 1993] ratio ≈ 0.1 is proposed.

Step 8 New individuals are selected using the *normalized geometric ranking* method.

Step 11 The temperature $T_{\max}$ should be chosen such that the ratio of accepted solutions to all solutions is $\approx 50\%$.

Step 18 This step is called the *cooling schedule*. We use a very simple form of cooling schedule $T_{i+1} = T_{\text{mult}} T_i$. In this step we also perform *reannealing* if necessary. If the actual temperature is lower than a given parameter $T_{\min}$, we set $T = T_{\max}$ and copy a half of the current population to a new one. Remaining part of a new population is generated randomly.

Diversity of population

As is evident from Fig. 3.2(b), the objective function possesses a large number of plateaus. Thus a part of population inevitably lands on one of theses plateaus if no action is taken. This, however, substantially decreases performance of the genetic algorithm.

To overcome this obstacle we introduce a very simple procedure for maintaining a sufficient diversity in population: Before inserting an offspring $\boldsymbol{X}$ into population, we first search for an individual $\boldsymbol{X'}$ which satisfies

$$F(\boldsymbol{X}) = F(\boldsymbol{X'}) \qquad \max_i |x_i - x'_i| < \varepsilon, i = 1, \ldots, 2N,$$

where ε is set here to 1×10^{-5}. If such an individual exists, it is replaced by $\boldsymbol{X}$. Otherwise an individual $\boldsymbol{X}$ enters a population following the step 7 in above algorithms. This procedure, though very simple and "naive", yields substantial improvement in stability of all previously mentioned methods.

3.1.3 Test example

To test individual methods we assumed a square periodic unit cell consisting of 10 fibers with the same volume fraction as the real specimen. As a first step we wished to fit functions $K_0(r)$ and $K(r)$ in five points only ($N_m = 5$). Sampled points were spaced by fiber diameter.

In all cases the initial population was generated purely randomly. Except for the **HGA** we created a population of size equal to 64 chromosomes. Only 8 individuals were generated to fill a population when running the **HGA**. Iteration process was terminated, if one of the following conditions was met:

- Algorithm returned value $F(\boldsymbol{x}) \leq \varepsilon = 6 \times 10^{-5}$.
- Number of function evaluations exceeded 250,000.

Each algorithm was running twenty times. For each run the number of function evaluations was recorded together with the minimum attained value of the objective function (3.1).

Table 3.1: Number of function evaluations

Algorithm	**Number of evaluations**		
	Min	Avg	Max
GA I	8,896	74,562	193,600
GA II	6,956	17,270	55,296
GA III	4,484	12,037	26,224
HGA	1,613	8,856	24,404
AUSA	3,490	8,709	26,314

Table 3.2: Characteristics of the best individual

Algorithm	**Number**	**Returned value** $\times 10^5$		
	found	Min	Avg	Max
GA I	18/20	6.0	7.2	16.4
GA II	20/20	5.9	6.0	6.0
GA III	20/20	5.9	6.0	6.0
HGA	20/20	5.9	6.0	6.0
AUSA	20/20	5.9	6.0	6.0

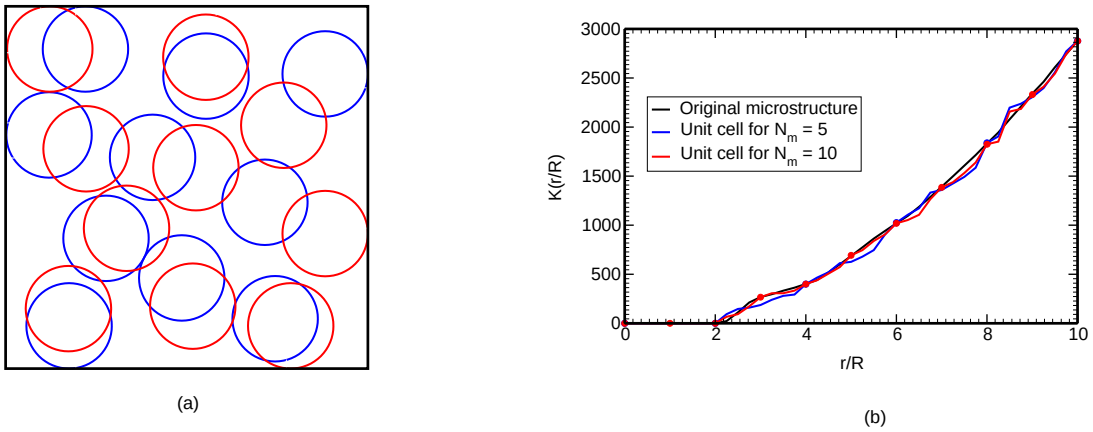

Figure 3.3: Periodic unit cells with corresponding second order intensity functions

Results and conclusions. Table 3.1 shows the minimum, maximum, and average values for the number of function evaluations. Table 3.2 lists similar results for the best chromosome in a population. In this case, however, we also included runs terminated after exceeding the maximum number of function evaluations. Presented results provide no evidence for promoting one particular method and discriminate the others, although nobody is perhaps caught by surprise seeing the **HGA** as the current winner and the **GAR I**, which did not always converged, as a looser. On the other hand, since all properties affecting the searching process (population size, initial parameter settings relevant to individual methods, age and optimization process dependent probabilities guiding an application of a given genetic operator) are hand tuned only, the efficiency of algorithms can be underestimated.

To check quality of the resultant unit cell we plotted the second order intensity function for original microstructure ($K_0(r)$) against the one associated with a unit cell chosen as the minimum from twenty independent runs. Results, derived via the **AUSA** method are plotted in Fig. 3.3(b). Evidently, both functions agree well at sampled points. Unfortunately, a significant deviation is distinct in all other points. To improve coincidence of both functions the number of sampled points was increased to 10 ($N_m = 10$) and the solutions obtained for $N_m = 5$ were used as initial guesses. In this way, a much better agreement was attained, see Fig. 3.3(b). Fig. 3.3(a) shows how the unit cell evolved when increasing an accuracy of our

solution. It is interesting to note that when running for example the **AUSA** for $N_m = 10$ from the beginning, we arrived at the minimum equal to 1.63×10^{-4} after approximately 173,000 function evaluations. However, when starting from $N_m = 5$ and then continuing with $N_m = 10$ we received the desired minimum after 115,000 function evaluations only. This just confirms similar conclusions drawn from experiments with complicated functions.

3.1.4 Some additional improvements

Improving the performance of genetic algorithms by putting in use the knowledge of the problem nature is essential for successful implementation of evolution programs. A proper selection of data coding, as discussed earlier, is just one example. Other features such as the adaptive operator probabilities or the problem-dependent operators are worthwhile to consider. Their impact on the present problem is inspected in subsequent paragraphs.

Adaptive operator probabilities

One of the most difficult problems faced when using a stochastic algorithm is a proper tuning of its parameters. In addition, as suggested by [Davis, 1989] and [Michalewicz et al., 1994], the role of individual operators changes during the optimization run.

Here, the approach established by [Davis, 1989] is reviewed. The key idea is to use operators which produce better offspring more often than those performing poorly. Besides promoting the operator which produced a good offspring, the operator responsible for creating its parent should receive some credit as well. In achieving this goal, the following guide-lines may be followed.

Whenever a new member is added to a population in step 7 of Algorithm 3.2 a pointer is set to its parent(s) and to the operator which created it. Further, a check is performed whether the new individual is the best one among all individuals in the current population. If yes, the amount that it is better is stored as a "local delta". This information is stored in some "adaptation window" which contains last W inserted members with parents considered

M generations back. The performance of each operator is computed after every I inserted new individuals. In the first step, every offspring in adaptation window passes P times its local delta to its parents and this parent(s) passes P portion of this value back to their parents etc. Then, delta is summed up for all members in adaptation window for all operators and operator probabilities are updated - each operator keeps S portion of its original value and remaining part is redistributed according to operators performance. More information can be found in [Davis, 1989].

In the present study, the **AUSA** algorithm served to assess applicability of the above procedure. Following [Davis, 1989], every operator was given initially the same probability and the parameter S was set to 0.01. The **AUSA** algorithm was called twenty times and terminated once the first adaptation took place. The adapted values were then averaged over all runs to obtain the initial probabilities of individual operators. The resulting operator probabilities are displayed in Table 3.3. It is evident that for the initial parts of the optimization process most of the progress is done by the boundary mutation and simple arithmetic crossover.

Operator	***Initial probability***
Uniform mutation	0.150
Boundary mutation	0.278
Non-uniform mutation	0.063
Multi-non uniform mutation	0.048
Simple crossover	0.040
Simple arithmetic crossover	0.233
Whole arithmetic crossover	0.097
Heuristic crossover	0.088

Table 3.3: Initial operator probabilities resulting from adaptation procedure

Finally, using these initial values of operator probabilities, the algorithm was rerun again

Table 3.4: AUSA algorithm with adaptive operator probabilities

Number	**Returned value** $\times 10^5$			**Number of evaluations**		
found	Min	Avg	Max	Min	Avg	Max
12/20	5.9	11.8	36.9	2,092	6,358	25,316

twenty times. The adaptivity setting was the same as in the previous example, except the value of S was set to .7. The results appear in Table 3.4.

Unfortunately, this approach seems to provide no benefit in the present optimization problem. The reason is obvious - the optimization procedure gets trapped in a local minimum. This can be attributed to a rapid increase in the probability of crossover operators as they produce good offspring.

Problem-dependent operators

The problem-dependent operators are the principle source of improvement. Their role in the present context is explored next.

Suppose that the parent configuration we selected for reproduction meets the *impenetrability constraint* imposed on the fibers arrangement. In the recombination step we wish to introduce only such operators, which yield an offspring configuration complying with the impenetrability condition as well. To state this in more formal manner, we define the search space as

$$\mathcal{S} = \left\{ x^i \in \langle 0; H_1 \rangle, y^i \in \langle 0; H_2 \rangle : \sqrt{(x^i - x^j)^2 + (y^i - y^j)^2} \geq 2R \,; i, j = 1, \ldots, N \right\}. \quad (3.4)$$

The simplest way to fulfill the above condition may rely on randomly generating a vector $\mathbf{x}'$ until the condition $\mathbf{x}' \in \mathcal{S}$ is met (death penalty to an infeasible individual (see e.g. [Povirk, 1995, Yeong and Torquato, 1998]). Clearly, this process may become prohibitively expensive, especially for a higher concentration of fibers.

To deal with this problem, it is more efficient to first determine a set of possible locations

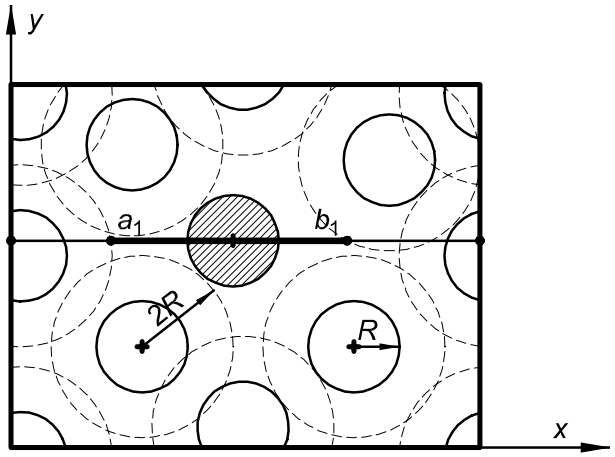

Figure 3.4: Allowable position of particle

of all particles and successively generate a new particle or particles, which belong to this set. Unfortunately, solving this problem in its full generality is rather complicated. Thus, instead of identifying allowable locations of *all* particles, we limit our attention to a set of possible locations of *one particle* permitted to translate either in the x or y direction, while the coordinates of the remaining fibers are kept fixed. We shall denote these sets as

$$\begin{aligned} \mathcal{S}|_{y^i} &= \left\{ x^i \in \langle 0; H_1 \rangle : \mathbf{x} \in \mathcal{S} \right\} \\ \mathcal{S}|_{x^i} &= \left\{ y^i \in \langle 0; H_2 \rangle : \mathbf{x} \in \mathcal{S} \right\}. \end{aligned} \tag{3.5}$$

To construct the above sets imagine a collection of identical cylinders, surrounded by a certain concentric protective cylindrical surface with diameter equal to $2R$ (see also discussion in Section 2.2.2). In view of the impenetrability constraint the secure cylinder cannot be occupied by another fibers' center. In particular, to identify space $\mathcal{S}|_{y^i}$ with the i-th particle we draw a line $x = x^i$, which intersects the protective surfaces around all remaining fibers in $n-1$ intervals $\langle a'_j; b'_j \rangle$ where $j = 1, \ldots, (n-1)$. Then the set $\mathcal{S}|_{y^i}$ of allowable locations of the particle i is given by (see Fig 3.4)

$$\mathcal{S}|_{y^i} = \langle 0; H_1 \rangle \setminus \bigcup_{j=1}^{n-1} \langle a'_j; b'_j \rangle = \bigcup_{j=1}^{n} \langle a_j; b_j \rangle. \tag{3.6}$$

Similarly we write

$$\mathcal{S}|_{x^i} = \langle 0; H_2\rangle \setminus \bigcup_{j=1}^{n-1} \langle a'_j; b'_j\rangle = \bigcup_{j=1}^{n} \langle a_j; b_j\rangle. \tag{3.7}$$

In the spirit of Eqs. (3.6) and (3.7) we can now define the following set of problem-specific operators (see also [Michalewicz et al., 1994]):

Uniform mutation Generate an integer number $i = u[1, N]$ with uniform distribution on a closed interval $\langle 1; N\rangle$, select the x or y coordinate, evaluate $\mathcal{S}|_{x^i}$ or $\mathcal{S}|_{y^i}$, select $k = u[1, n]$ and set:

$$x'^i = x^i + u(a_k, b_k)$$

or

$$y'^i = y^i + u(a_k, b_k),$$

while fixing the remaining coordinates.

Non-uniform mutation Select $i = u[1, N]$ and the x or y coordinate, evaluate $\mathcal{S}|_{x^i}$ or $\mathcal{S}|_{y^i}$. Select k such that $x^i \in \langle a_k; b_k\rangle$ or $y^i \in \langle a_k; b_k\rangle$, generate a real number $p = u(0, 1)$ with uniform distribution on a closed interval $\langle 0; 1\rangle$ and set:

$$x'_i = \begin{cases} x^i + (b_k - x^i) f(t), & \text{if } p < .5 \\ x^i + (a_k - x^i) f(t), & \text{if } p \geq .5 \end{cases}$$

or

$$y'_i = \begin{cases} y^i + (b^k - y^i) f(t), & \text{if } p < .5 \\ y^i + (a^k - y^i) f(t), & \text{if } p \geq .5 \end{cases},$$

while fixing the remaining coordinates. The number $f(t)$ is the same as in Section 3.1.2

Multi-non-uniform mutation Non-uniform mutation applied successively to all coordinates of $\mathbf{X}$.

Simple two-point crossover Select $i = u[1,n]$ and $j = u[1,n] \wedge i < j$. Repeat for $k = i, \ldots, j$:

$$\begin{aligned} {}^1x'^k &= {}^1x^k(1-\alpha) +^2 x^k\alpha \\ {}^2x'^k &= {}^1x^k\alpha +^2 x^k(1-\alpha), \end{aligned}$$

and

$$\begin{aligned} {}^1y'^k &= {}^1y^k(1-\alpha) +^2 y^k\alpha \\ {}^2y'^k &= {}^1y^k\alpha +^2 y^k(1-\alpha), \end{aligned}$$

where e.g. ${}^2x^k$ corresponds to the x coordinate of k-th particles of the second parent. The parameter α is set to 1 initially. If $x'^k \notin \mathcal{S}|_{y^i}$ or $y'^k \notin \mathcal{S}|_{x^i}$, respectively, decrease α by $1/n_d$; n_d is the user-defined parameter (number of decreasing steps). This procedure is repeated until $x'^k \in \mathcal{S}|_{y^i}$ or $y'^k \in \mathcal{S}|_{x^i}$ holds (this condition is always met for $\alpha = 0$).

The above operators were implemented into the **AUSA** algorithm with considerable success. The algorithm met the convergence criteria in all 20 runs and the average number of evaluations was reduced by 50%. The results are summarized in Table 3.5

Table 3.5: AUSA algorithm with problem-dependent operators

Number	**Returned value** $\times 10^5$			**Number of evaluations**		
found	Min	Avg	Max	Min	Avg	Max
20/20	5.9	6.0	6.0	543	4,403	11,516

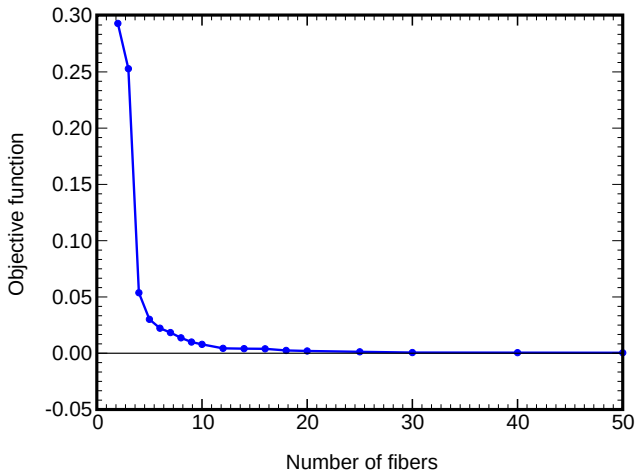

Figure 3.5: Variation of the objective function with the number of particles in the PUC.

3.1.5 Determination of the periodic unit cell

The principal objective of the present work is to construct a certain periodic unit cell, which may substitute the real microstructure when estimating the macroscopic response of a random composite subjected to uniform stresses or strains. In particular, we wish to assess a sensitivity of the proposed solution procedure to the size of the unit cell (number of particles within the PUC).

Here, this task is explored from the objective function point of view. The essential parts of the optimization procedure are reviewed in conjunction with the **AUSA** method. Results are presented for a selected set of unit cells.

Finding an optimal fiber configuration. Optimal fiber configuration was found combining the **AUSA** method (Algorithm 3.3) with the problem-specific operators presented in Section 3.1.4. The initial results appear in Fig. 3.5 showing a variation of the objective function, with the number of particles (fibers) within the unit cell. In all examples the initial population was generated purely randomly. Optimization process was terminated, when one of the following conditions was met:

- Algorithm returned value $F(\boldsymbol{x}^N_{H_1,H_2}) \leq \varepsilon = 10^{-2}$ for $N = 32$.
- Number of function evaluations exceeded 250,000.

The first condition is usually fulfilled for small values of N_m, while the second one takes effect in remaining cases. The results indicate that for unit cells with less than 10 particles the above convergence criterion was too severe. On the other hand, we registered a significant drop of the objective function already for 4 particles within the unit cell.

Results derived for each unit cell were chosen as the minimum from ten independent runs. In every run we started from only four points, in which we attempted to fit functions $K_0(r)$ and $K(r)$ ($N = 4$ in Eq. (3.1)). To improve conformity of both functions we successively increased the number of sampled points up to $N = 32$ while using the previous solution as the initial guess (best 50% of individuals were used). The selection of sampled points was biased towards the ratio $r/R = 2$ to capture an apparent correlation of individual space points within the sample.

Finding an optimal side ratio. The Golden Section search method, Algorithm 3.1, with values $\eta_a = 1.0$, $\eta_b = 2.0$ and $\epsilon = .05$ was employed. Fiber configuration corresponding to $N_m = 32$ for a given set of values H_1 and H_2 was used as a starting point for the second optimization problem (P2).

To illustrate this procedure we considered a periodic unit cell with 10 particles. Results appear in Fig. 3.6. Evolution of the unit cell with increasing accuracy of the solution is plotted in Fig. 3.6(a), whereas Fig. 3.6(b) displays a variation of the normalized second order intensity function $K(r)/\pi r^2$ corresponding to various stages of the solution process. A rather noisy character of this function associated with a given number of sampled points is attributed to the difference between the number of sampled points and the number of selected radii r for which this function is actually presented (all functions, including the one corresponding to the real microstructure were computed for the same radii r). Finally, some

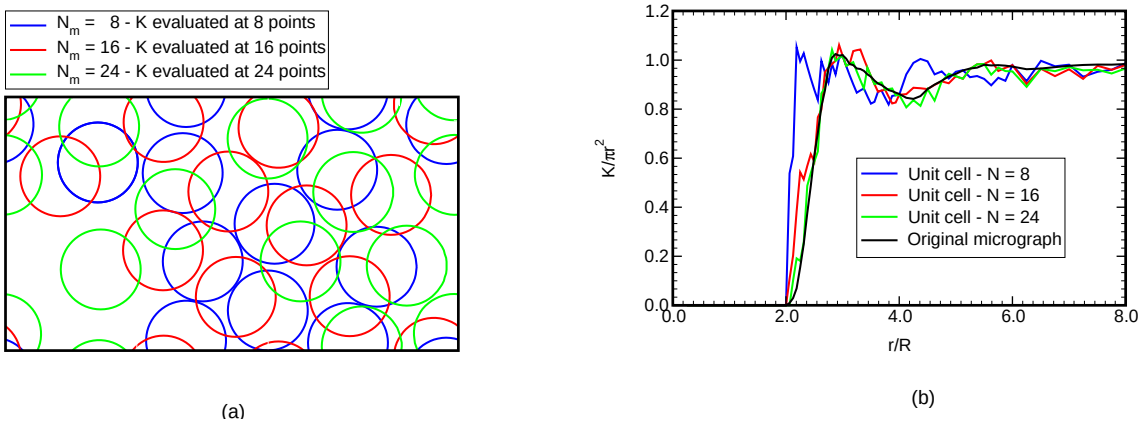

Figure 3.6: Evolution of the 10 particles PUC

examples of the resulting unit cells are illustrated in Fig. 3.7 together with the hexagonal lattice shown for comparison. It is evident, that periodic unit cells resulting from optimization are able to capture the clustering of particles in the original micrograph to some extent.

3.2 Effective response of composites with periodic microstructure

This section illustrates the capability of the present approach by comparing the effective response of both the real composite and selected set of associated periodic unit cells. With reference to the introductory part the micromechanical analysis is restricted to elastic and viscoelastic response of a composite aggregate to a prescribed path of uniform macroscopic strains or stresses and uniform temperature change. The principle objective of this section is to offer the smallest representative volume element (the periodic unit cell with the least number of particles) which gives the same macroscopic response as the real composite. Recall that results discussed in the previous section suggest, see Fig. 3.5, that the periodic unit cell with at least ten particles should be considered for the numerical analysis.

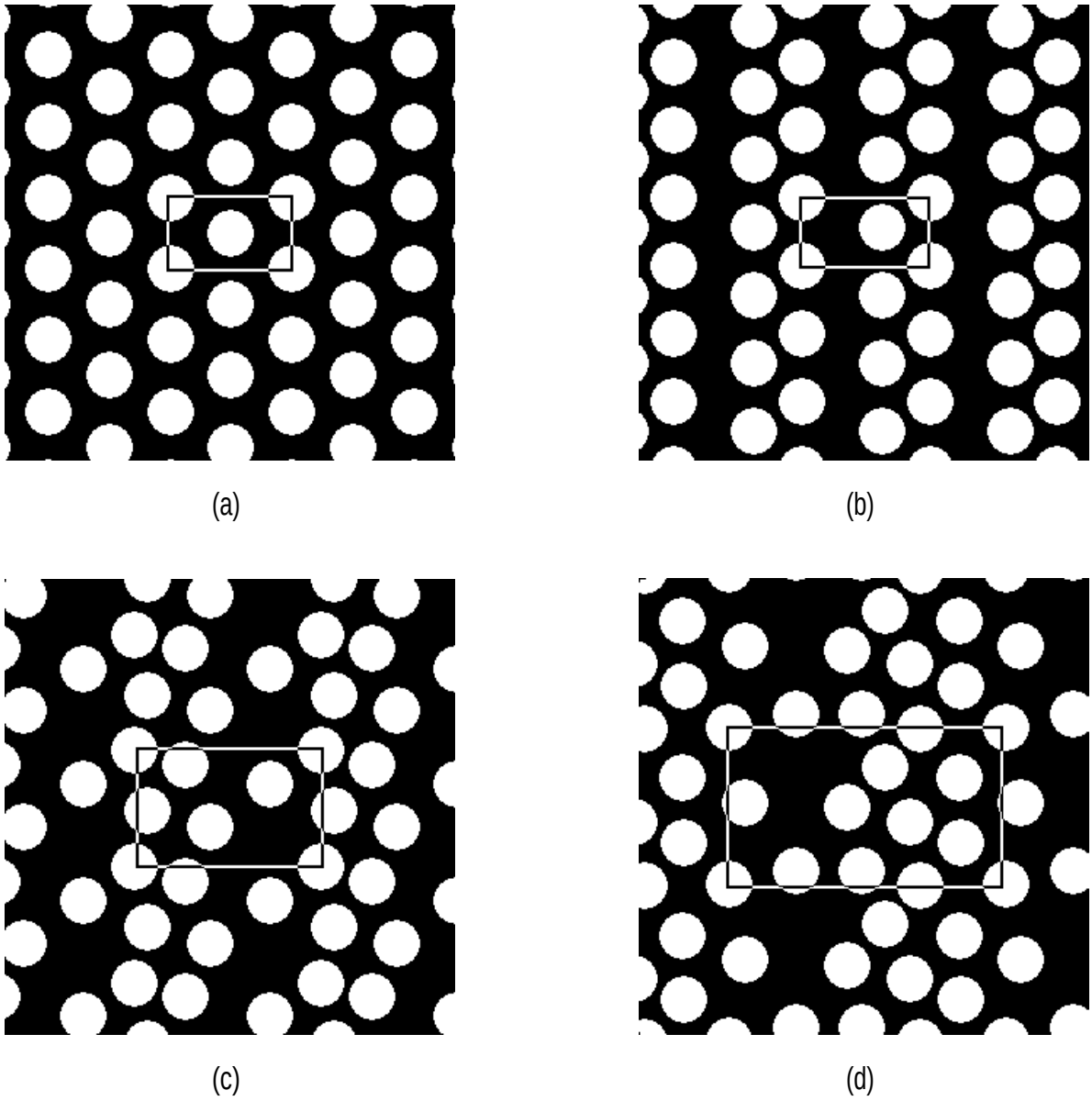

Figure 3.7: Periodic unit cells: (a) Hexagonal lattice, (b) 2-fibers PUC, (c) 5-fibers PUC, (d) 10-fibers PUC.

3.2.1 Effective elastic moduli

To narrow a vast body of material on this subject we limit our attention to studies dealing with the finite element analysis of the periodic unit cell [Teplý and Dvořák, 1988] and [Michel et al., 1999, to cite a few]. This approach becomes particularly attractive when applied to "simple" microstructures such as those displayed in Fig. 3.7 and will be used throughout this section to estimate overall elastic moduli of a graphite fiber tow impregnated by polymer matrix, Fig. 2.1.

The overall elastic behavior of such a composite is then governed by its microstructure and by the behavior of individual phases conveniently described by displacement, strain and stress fields in the form

$$\boldsymbol{\partial}\boldsymbol{\sigma}(\mathbf{x}) = -\boldsymbol{b}(\mathbf{x}), \tag{3.8}$$

$$\boldsymbol{\epsilon}(\mathbf{x}) = \boldsymbol{\partial}^{\mathrm{T}}\boldsymbol{u}(\mathbf{x}), \tag{3.9}$$

$$\boldsymbol{\sigma}(\mathbf{x}) = \mathbf{L}(\mathbf{x})\boldsymbol{\epsilon}(\mathbf{x}), \qquad \boldsymbol{\epsilon}(\mathbf{x}) = \mathbf{M}(\mathbf{x})\boldsymbol{\sigma}(\mathbf{x}), \tag{3.10}$$

where $\boldsymbol{u}$ is the displacement field; $\boldsymbol{\epsilon}$ and $\boldsymbol{\sigma}$ are the strain and stress fields, respectively; $\mathbf{L}$ is the stiffness tensor and $\mathbf{M}$ is the compliance tensor such that $\mathbf{L}^{-1} = \mathbf{M}$; $\boldsymbol{b}$ is the vector of body forces and $\boldsymbol{\partial}$ is the differential operator matrix [Bittnar and Šejnoha, 1996, p. 9]

The following discussion is limited to two-phase fibrous composites with fibers aligned along the x_3 axis. We further assume that each phase is transversally isotropic with x_3 being the axis of rotational symmetry. Additional simplification arises when neglecting the out-of-plane shear response. The generalized plane strain is then a natural assumption. In such a state, the only non-zero components of the strain and stress tensors are $\epsilon_{11}, \epsilon_{12}, \epsilon_{22}, \epsilon_{33}$ and $\sigma_{11}, \sigma_{12}, \sigma_{22}, \sigma_{33}$, respectively. Note that due to perfect bonding between individual phases the components ϵ_{33} and σ_{33} attain constant values. Employing Hill's notation [Hill, 1964]

the stiffness tensor $\mathbf{L}$ can be represented by the 4×4 matrix in the form

$$\mathbf{L} = \begin{bmatrix} (\mathrm{k}+\mathrm{m}) & (\mathrm{k}-\mathrm{m}) & 0 & l \\ (\mathrm{k}-\mathrm{m}) & (\mathrm{k}+\mathrm{m}) & 0 & l \\ 0 & 0 & \mathrm{m} & 0 \\ l & l & 0 & \mathrm{n} \end{bmatrix}, \tag{3.11}$$

which in general is function of $\mathbf{x}$; constants k,m,n and l are related to the material engineering constants by

$$\begin{aligned} \mathrm{k} &= -[1/\mathrm{G_T} - 4/\mathrm{E_T} + 4\nu_\mathrm{A}^2/\mathrm{E_A}]^{-1} \qquad l = 2\mathrm{k}\nu_\mathrm{A} \\ \mathrm{n} &= \mathrm{E_A} + 4\mathrm{k}\nu_\mathrm{A}^2 = \mathrm{E_A} + l^2/\mathrm{k} \qquad \mathrm{m} = \mathrm{G_T}. \end{aligned}$$

Assuming constant phase moduli and with reference to Eqs. (3.10) the elastic constitutive equations of the phases are given by

$$\boldsymbol{\sigma}_r(\mathbf{x}) = \mathbf{L}_r\boldsymbol{\epsilon}_r(\mathbf{x}), \qquad \boldsymbol{\epsilon}_r(\mathbf{x}) = \mathbf{M}_r\boldsymbol{\sigma}_r(\mathbf{x}), \qquad r = f, m. \tag{3.12}$$

Define the following mechanical loading problems

$$\boldsymbol{u}_0(\mathbf{x}) = \boldsymbol{E}\cdot\mathbf{x} \qquad \mathbf{x}\in S, \tag{3.13}$$

$$\boldsymbol{p}_0(\mathbf{x}) = \boldsymbol{\Sigma}\cdot\boldsymbol{n}(\mathbf{x}) \qquad \mathbf{x}\in S, \tag{3.14}$$

where $\boldsymbol{u}_0$ and $\boldsymbol{p}_0$ are the displacement and traction vectors at the external boundary S of a representative volume element Ω of the composite; $\boldsymbol{n}$ is the outer unit normal to S; $\boldsymbol{E}$ and $\boldsymbol{\Sigma}$ are the applied macroscopic uniform strain and stress fields, respectively. The macroscopic constitutive relations are then provided by

$$\langle\boldsymbol{\sigma}(\mathbf{x})\rangle = \langle\mathbf{L}(\mathbf{x})\boldsymbol{\epsilon}(\mathbf{x})\rangle = \sum_{r=1}^{2} c_r\mathbf{L}_r\langle\boldsymbol{\epsilon}_r(\mathbf{x})\rangle = \mathbf{L}\,\boldsymbol{E} \tag{3.15}$$

$$\langle\boldsymbol{\epsilon}(\mathbf{x})\rangle = \langle\mathbf{M}(\mathbf{x})\boldsymbol{\sigma}(\mathbf{x})\rangle = \sum_{r=1}^{2} c_r\mathbf{M}_r\langle\boldsymbol{\sigma}_r(\mathbf{x})\rangle = \mathbf{M}\,\boldsymbol{\Sigma}, \tag{3.16}$$

where $\langle\cdot\rangle$ stands for the spatial average of a given field, c_r is the volume fraction of the r^{th} phase, and $\mathbf{L}$ and $\mathbf{M}$ are the effective stiffness and compliance matrices of the heterogenous

material, respectively. Eqs. (3.15) and (3.16) follow directly from Hill's lemma [Hill, 1963]. He proved that for compatible strain and equilibrated stress fields the following relation holds

$$\left\langle \boldsymbol{\epsilon}(\mathbf{x})^{\mathrm{T}} \boldsymbol{\sigma}(\mathbf{x}) \right\rangle = \langle \boldsymbol{\epsilon}(\mathbf{x}) \rangle^{\mathrm{T}} \langle \boldsymbol{\sigma}(\mathbf{x}) \rangle , \tag{3.17}$$

and consequently

$$\boldsymbol{E}^{\mathrm{T}} \mathbf{L} \boldsymbol{E} = \langle \boldsymbol{\epsilon}(\mathbf{x})^{\mathrm{T}} \mathbf{L}(\mathbf{x}) \boldsymbol{\epsilon}(\mathbf{x}) \rangle, \tag{3.18}$$

$$\boldsymbol{\Sigma}^{\mathrm{T}} \mathbf{M} \boldsymbol{\Sigma} = \langle \boldsymbol{\sigma}(\mathbf{x})^{\mathrm{T}} \mathbf{M}(\mathbf{x}) \boldsymbol{\sigma}(\mathbf{x}) \rangle. \tag{3.19}$$

Eq. (3.17) states in fact that the average of "microscopic" internal work is equal to the macroscopic work done by internal forces. The above relations provide the stepping stone for the derivation of effective properties of composite materials.

The following paragraphs outline evaluation of effective properties of a composite aggregate represented here by the periodic material models of Fig. 3.7. Two specific approaches corresponding to loading conditions (3.13) and (3.14) are discussed in the sequel.

Formulation based on strain approach

Consider a material representative volume defined in terms of a periodic unit cell (PUC). Suppose that the PUC is subjected to boundary displacements $\boldsymbol{u}_0$ resulting in a uniform strain $\boldsymbol{E}$ throughout the body, Eq. (3.13). In view of boundary conditions imposed on the unit cell the strain and displacement fields in the PUC admit the following decomposition

$$\boldsymbol{u}(\mathbf{x}) = \boldsymbol{E} \cdot \mathbf{x} + \boldsymbol{u}^*(\mathbf{x}), \qquad \forall\, \mathbf{x} \in \Omega, \;\; \boldsymbol{u} = \boldsymbol{u}_0 \;\forall\, \mathbf{x} \in S \tag{3.20}$$

$$\boldsymbol{\epsilon}(\mathbf{x}) = \boldsymbol{E} + \boldsymbol{\epsilon}^*(\mathbf{x}), \qquad \forall\, \mathbf{x} \in \Omega. \tag{3.21}$$

The first term in Eq. (3.20) corresponds to a displacement field in an effective homogeneous medium which has the same overall properties at the composite aggregate. The fluctuation part $\boldsymbol{u}^*$ enters Eq. (3.20) as a consequence of the presence of heterogeneities and has to disappear upon volume averaging, see [Beran, 1968] for further discussion. This condition

is met for any periodic displacement field with the period equal to the size of the unit cell under consideration, [Michel et al., 1999, and references therein]. The periodicity of $\boldsymbol{u}^*$ further implies that the average of $\boldsymbol{\epsilon}^*$ in the unit cell vanishes as well. Hence

$$\langle \boldsymbol{\epsilon}(\mathbf{x}) \rangle = \boldsymbol{E} + \langle \boldsymbol{\epsilon}^*(\mathbf{x}) \rangle \,, \qquad \langle \boldsymbol{\epsilon}^*(\mathbf{x}) \rangle = \frac{1}{\Omega} \int_\Omega \boldsymbol{\epsilon}^*(\mathbf{x}) \mathrm{d}\mathbf{x} = \mathbf{0}. \tag{3.22}$$

Next, assume a virtual displacement $\delta\boldsymbol{u}(\mathbf{x}) = \delta\boldsymbol{E} \cdot \mathbf{x} + \delta\boldsymbol{u}^*(\mathbf{x})$, with $\delta\boldsymbol{u}^*(\mathbf{x})$ being periodic. Then the principle of virtual work reads

$$\left\langle \delta\boldsymbol{\epsilon}(\mathbf{x})^{\mathrm{T}} \boldsymbol{\sigma}(\mathbf{x}) \right\rangle = \langle \delta\boldsymbol{\epsilon}(\mathbf{x}) \rangle^{\mathrm{T}} \langle \boldsymbol{\sigma}(\mathbf{x}) \rangle = 0, \tag{3.23}$$

since $\langle \boldsymbol{\sigma} \rangle = \mathbf{0}$. Eq. (3.23) is essentially the Hill lemma introduced by Eq. (3.17).

Solving the above relation calls for a suitable numerical technique such as the Finite Element Method (FEM), [Bittnar and Šejnoha, 1996]. In this framework the displacement field in Eq. (3.20) assumes the form

$$\boldsymbol{u}(\mathbf{x}) = \boldsymbol{E} \cdot \mathbf{x} + \mathbf{N}(\mathbf{x})\boldsymbol{r}, \tag{3.24}$$

where $\mathbf{N}(\mathbf{x})$ represent shape functions of a given element (constant strain triangles are used in the present study) and $\boldsymbol{r}$ is the vector of unknown degrees of freedom. The corresponding strain field is then provided by

$$\boldsymbol{\epsilon}(\mathbf{x}) = \boldsymbol{E} + \mathbf{B}(\mathbf{x})\boldsymbol{r}. \tag{3.25}$$

Introducing Eq. (3.25) into Eq. (3.23) gives for any kinematically admissible strains $\delta\boldsymbol{\epsilon}^* = \mathbf{B}\delta\mathbf{u}^*$ the associated system of linear equations in the form

$$\mathbf{K}\boldsymbol{r} = \boldsymbol{f}, \tag{3.26}$$

where

$$\begin{aligned} \mathbf{K} &= \sum_e \mathbf{K}^e \quad \text{where} \quad \mathbf{K}^e = \frac{1}{\Omega} \int_{A^e} \mathbf{B}^{\mathrm{T}} \mathbf{L}^e \mathbf{B} \, \mathrm{d}A^e \\ \boldsymbol{f} &= \sum_e \boldsymbol{f}^e \quad \text{where} \quad \boldsymbol{f}^e = -\frac{1}{\Omega} \int_{A^e} \mathbf{B}^{\mathrm{T}} \mathbf{L}^e \boldsymbol{E} \, \mathrm{d}A^e, \end{aligned} \tag{3.27}$$

where $\mathbf{K}$ is the stiffness matrix of the system and $\boldsymbol{f}$ is the vector of global nodal forces resulting from the loading by $\boldsymbol{E}$; e stands for the number of elements, A^e is the area of element e and Ω is the area of the PUC.

System (3.26) can be used to provide the coefficients of the effective stiffness matrix $\mathbf{L}$ as volume averages of the local fields derived from the solution of four successive elasticity problems. To that end, the periodic unit cell is loaded, in turn, by each of the four components of $\boldsymbol{E}$, while the other three components vanish. The volume stress averages normalized with respect to $\boldsymbol{E}$ then furnish individual columns of $\mathbf{L}$. The required periodicity conditions (same displacements $\boldsymbol{u}^*$ on opposite sides of the unit cell) is accounted for through multi-point constraints.

Formulation based on stress approach

Sometimes it is desirable to apply the overall stress $\boldsymbol{\Sigma}$, Eq. (3.14), instead of the overall strain $\boldsymbol{E}$. Eq. (3.23) then modifies to

$$\left\langle \delta\boldsymbol{\epsilon}(\mathbf{x})^{\mathrm{T}}\boldsymbol{\sigma}(\mathbf{x})\right\rangle = \delta\boldsymbol{E}^{\mathrm{T}}\boldsymbol{\Sigma}, \qquad\qquad \boldsymbol{\Sigma} = \langle\boldsymbol{\sigma}(\mathbf{x})\rangle\,. \tag{3.28}$$

Clearly, such a loading condition leaves us with unknown overall strain $\boldsymbol{E}$ and periodic displacement field $\boldsymbol{u}^*$ to be determined. Substituting Eq. (3.21) into Eq. (3.28) yields

$$\delta\boldsymbol{E}^{\mathrm{T}}\left\langle\mathbf{L}(\mathbf{x})\left(\boldsymbol{E}+\boldsymbol{\epsilon}^*(\mathbf{x})\right)\right\rangle + \left\langle\delta\boldsymbol{\epsilon}^*(\mathbf{x})^{\mathrm{T}}\mathbf{L}(\mathbf{x})\boldsymbol{E}\right\rangle + \left\langle\delta\boldsymbol{\epsilon}^*(\mathbf{x})^{\mathrm{T}}\mathbf{L}(\mathbf{x})\boldsymbol{\epsilon}^*(\mathbf{x})\right\rangle = \delta\boldsymbol{E}^{\mathrm{T}}\boldsymbol{\Sigma}. \tag{3.29}$$

Since $\delta\boldsymbol{E}$ and $\delta\boldsymbol{\epsilon}^*(\mathbf{x})$ are independent, the preceding equation can be split into two equalities

$$\begin{aligned} \delta\boldsymbol{E}^{\mathrm{T}}\boldsymbol{\Sigma} &= \delta\boldsymbol{E}^{\mathrm{T}}\left[\langle\mathbf{L}(\mathbf{x})\rangle\,\boldsymbol{E} + \langle\mathbf{L}(\mathbf{x})\boldsymbol{\epsilon}^*(\mathbf{x})\rangle\right] \\ 0 &= \left\langle\delta\boldsymbol{\epsilon}^*(\mathbf{x})^{\mathrm{T}}\mathbf{L}(\mathbf{x})\right\rangle\boldsymbol{E} + \left\langle\delta\boldsymbol{\epsilon}^*(\mathbf{x})^{\mathrm{T}}\mathbf{L}(\mathbf{x})\boldsymbol{\epsilon}^*(\mathbf{x})\right\rangle \end{aligned} \tag{3.30}$$

Finally, following the same lines as in the previous paragraph the FE discretization, Eqs. (3.24) and (3.25), provides the linear coupled system in the form, [Michel et al., 1999],

$$\begin{bmatrix} \frac{1}{\Omega}\int_\Omega \mathbf{L}\,\mathrm{d}\Omega & \frac{1}{\Omega}\int_\Omega \mathbf{LB}\,\mathrm{d}\Omega \\ \frac{1}{\Omega}\int_\Omega \mathbf{B}^{\mathrm{T}}\mathbf{L}\,\mathrm{d}\Omega & \frac{1}{\Omega}\int_\Omega \mathbf{B}^{\mathrm{T}}\mathbf{LB}\,\mathrm{d}\Omega \end{bmatrix} \begin{Bmatrix} \boldsymbol{E} \\ \boldsymbol{r} \end{Bmatrix} = \begin{Bmatrix} \boldsymbol{\Sigma} \\ \mathbf{0} \end{Bmatrix}. \tag{3.31}$$

The above system of equations serves to derive the coefficients of the effective compliance matrix $\mathbf{M}$. In analogy with the strain approach, the periodic unit cell is loaded, in turn, by each of the four components of $\boldsymbol{\Sigma}$, while the other three components vanish. The volume strain averages normalized with respect to $\boldsymbol{\Sigma}$ then supply individual entries of $\mathbf{M}$.

3.2.2 Numerical results

In keeping up with our promise we now present several numerical results derived for a given material system, in order to provide estimates of the minimum size of the periodic unit cell with regard to the material effective properties. A generalized plane-strain state is assumed throughout the analysis. Details regarding the theoretical formulation are given in [Michel et al., 1999].

As an example we consider a brittle (or quasibrittle) composite system composed of the graphite fibers embedded in the epoxy matrix. Material properties are listed in Table 3.6.

Table 3.6: Material properties of T30/Epoxy system

phase	E_A [GPa]	E_T [GPa]	G_T [GPa]	ν_A
fiber	386	7.6	2.6	0.41
matrix	5.5	5.5	1.96	0.40

First, to prove applicability of the proposed method, we compare the elastic moduli derived for the original microstructure, Fig 2.1, with those found for the periodic unit cells displayed in Fig. 3.7. Note that the solution of the original problem requires to process of the order of magnitude more equations than the solution based on the PUC approach.

Selected components of the effective stiffness matrix $\mathbf{L}$ are stored in Table 3.7. Results obtained for the hexagonal arrangements of fibers are provided for additional comparison. Evidently, the periodic unit cell unlike the hexagonal lattice, which corresponds to the

Table 3.7: Components of the effective stiffness matrix [GPa]

Unit cell	L_{11}	L_{22}	L_{33}	L_{44}	c_f
Original	10.76	10.73	2.215	177.2	0.44
2 fibers PUC	10.78	10.75	2.202	177.2	0.44
5 fibers PUC	10.76	10.73	2.215	177.2	0.44
10 fibers PUC	10.76	10.73	2.215	177.2	0.44
Hexagonal array	10.74	10.74	2.213	177.3	0.44

transversally isotropic medium, is capable of capturing a slight anisotropy associated with the real microstructure. In addition, the results in Table 3.7 also promote the PUC consisting of 5 fibers only as the smallest one we should consider for the evaluation of effective properties.

To further support the present approach we determined the mean value and standard deviation of effective stiffnesses derived from five independent runs for unit cells defined through a random cut of the original micrograph, Fig. 2.1(b). Dimensions of such a unit cell were selected to comply with dimensions found for the PUC consisting of 10 particles. Results, given in Table 3.9, are rather discouraging and should caution the reader against pursuing this approach.

Table 3.8: Variation of effective stiffnesses for five ten-particle optimal PUC

Modulus	**Mean value** [GPa]	**Standard deviation** [GPa]	**Variation coefficient** [%]
L_{11}	10.76	0.013	0.12
L_{22}	10.73	0.013	0.12
L_{33}	2.215	0.003	0.13

Finally, to confirm our theoretical expectations, we investigated an influence of the proposed optimization technique on the effective moduli computed for the 10-fibers PUC derived from five independent optimization runs. Results stored in Table 3.8 show that the final moduli are not sensible to the particular fiber configuration (each optimization run provides a slight different fiber arrangements having, however, the same material's statistics up to two-point probability function).

Table 3.9: Variation of effective stiffnesses for five randomly picked ten-particle PUC

Modulus	**Mean value**	**Standard deviation**	**Variation coefficient**
	[GPa]	[GPa]	[%]
L_{11}	10.73	0.32	2.97
L_{22}	10.71	0.38	3.54
L_{33}	2.210	0.07	3.48

3.3 Thermal and residual fields

Apart from mechanical loading, Eqs. (3.13) and (3.14), composite materials often experience loading by distribution of local eigenstrains or eigenstresses. Regardless of their origin they may be interpreted as internal loads in an otherwise elastic medium [Fish et al., 1997, Dvorak and Benveniste, 1992a]. Thermal and viscoelastic strains, admitted in the present analysis, together with transformation strains discussed in Chapter 4 are specific examples of such fields. Extension to the modeling of inelastic deformation and various damage events such as fiber debonding and/or sliding by means of equivalent eigenstrains has also been successfully examined [Sejnoha, 1999, Srinivas, 1997, Dvorak and Benveniste, 1992b].

3.3.1 Thermomechanical response

Consider the RVEs of Fig. 3.7. Further suppose that in addition to mechanical loading the representative volume is subjected to a uniform temperature change $\Delta\theta$. The local constitutive equations (3.10) are then augmented to read

$$\boldsymbol{\sigma}(\mathbf{x}) = \mathbf{L}(\mathbf{x})\boldsymbol{\epsilon}(\mathbf{x}) + \boldsymbol{\lambda}(\mathbf{x}), \qquad \boldsymbol{\epsilon}(\mathbf{x}) = \mathbf{M}(\mathbf{x})\boldsymbol{\sigma}(\mathbf{x}) + \boldsymbol{\mu}(\mathbf{x}), \qquad r = f, m, \tag{3.32}$$

and similarly the phase constitutive equations (3.12) become

$$\boldsymbol{\sigma}_r(\mathbf{x}) = \mathbf{L}_r\boldsymbol{\epsilon}_r(\mathbf{x}) + \boldsymbol{\lambda}_r, \qquad \boldsymbol{\epsilon}_r(\mathbf{x}) = \mathbf{M}_r\boldsymbol{\sigma}_r(\mathbf{x}) + \boldsymbol{\mu}_r, \qquad r = f, m, \tag{3.33}$$

where the local phase eigenstrain $\boldsymbol{\mu}_r = \boldsymbol{m}_r\Delta\theta$ and eigenstress $\boldsymbol{\lambda}_r$ are related by

$$\boldsymbol{\mu}_r = -\mathbf{M}_r\boldsymbol{\lambda}_r, \qquad \boldsymbol{\lambda}_r = -\mathbf{L}_r\boldsymbol{\mu}_r, \qquad r = f, m. \tag{3.34}$$

The thermal strain vector $\boldsymbol{m}_r$ lists the coefficients of thermal expansion of the phase r.

To proceed we recall the stress control approach and rewrite Eq. (3.28) in the form

$$\left\langle \delta\boldsymbol{\epsilon}(\mathbf{x})^{\mathrm{T}}\boldsymbol{\sigma}(\mathbf{x}) \right\rangle = \left\langle \delta\boldsymbol{\epsilon}(\mathbf{x})^{\mathrm{T}}\mathbf{L}(\mathbf{x})\left(\boldsymbol{\epsilon}(\mathbf{x}) - \boldsymbol{\mu}(\mathbf{x})\right) \right\rangle = \delta\boldsymbol{E}^{\mathrm{T}}\boldsymbol{\Sigma}. \tag{3.35}$$

With reference to Eq. (3.31) the resulting system of algebraic equations arising in the Finite Element formulation assumes the form

$$\begin{bmatrix} \frac{1}{\Omega}\int_\Omega \mathbf{L}\,\mathrm{d}\Omega & \frac{1}{\Omega}\int_\Omega \mathbf{L}\mathbf{B}\,\mathrm{d}\Omega \\ \frac{1}{\Omega}\int_\Omega \mathbf{B}^{\mathrm{T}}\mathbf{L}\,\mathrm{d}\Omega & \frac{1}{\Omega}\int_\Omega \mathbf{B}^{\mathrm{T}}\mathbf{L}\mathbf{B}\,\mathrm{d}\Omega \end{bmatrix} \begin{Bmatrix} \boldsymbol{E} \\ \boldsymbol{r} \end{Bmatrix} = \begin{Bmatrix} \boldsymbol{\Sigma} + \frac{1}{\Omega}\int_\Omega \mathbf{L}\boldsymbol{\mu}\,\mathrm{d}\Omega \\ \frac{1}{\Omega}\int_\Omega \mathbf{B}^{\mathrm{T}}\mathbf{L}\boldsymbol{\mu}\,\mathrm{d}\Omega \end{Bmatrix}. \tag{3.36}$$

When excluding the thermal effects the above equation reduces to Eq. (3.31). However, when the loading conditions are limited to the uniform temperature change equal to unity, the components of the overall average strain comply with the effective coefficients of thermal expansion $\boldsymbol{m}$. Note that the present formulation is not applicable with the strain control conditions when admitting the thermal loading. Clearly, the overall strain $\boldsymbol{E}$ is then not known and cannot be prescribed.

We now proceed to examine various connections between the thermal and mechanical properties of composite materials. To begin, recall the primary principle of virtual work written in the form

$$\int_{\Omega} \delta\boldsymbol{\epsilon}(\mathbf{x})^{\mathrm{T}}\boldsymbol{\sigma}(\mathbf{x})\,\mathrm{d}\Omega = \Omega\,\delta\boldsymbol{E}^{\mathrm{T}}\boldsymbol{\Sigma}. \tag{3.37}$$

When introducing Eq. $(3.32)_2$ into Eq. (3.37) we get

$$\int_{\Omega} \delta\boldsymbol{\sigma}(\mathbf{x})^{\mathrm{T}}\mathbf{M}\boldsymbol{\sigma}(\mathbf{x})\,\mathrm{d}\Omega = \Omega\,\delta\boldsymbol{E}^{\mathrm{T}}\boldsymbol{\Sigma}, \qquad \delta\boldsymbol{\mu}(\mathbf{x}) \;=\; \delta\boldsymbol{m}(\mathbf{x})\Delta\theta \;=\; \mathbf{0}. \tag{3.38}$$

Then, substituting Eq. $(3.32)_2$ into the dual virtual principle gives

$$\int_{\Omega} \delta\boldsymbol{\sigma}(\mathbf{x})^{\mathrm{T}}\left[\mathbf{M}(\mathbf{x})\boldsymbol{\sigma}(\mathbf{x}) + \boldsymbol{m}(\mathbf{x})\Delta\theta\right]\,\mathrm{d}\Omega = \Omega\,\delta\boldsymbol{\Sigma}^{\mathrm{T}}\boldsymbol{E} \;=\; \Omega\,\delta\boldsymbol{E}^{\mathrm{T}}\mathbf{L}\boldsymbol{E}. \tag{3.39}$$

Introducing $\boldsymbol{\sigma}(\mathbf{x}) = \mathbf{B}(\mathbf{x})\boldsymbol{\Sigma}$ and combining Eqs. (3.38) and (3.39) yields

$$\begin{aligned} \Omega\,\delta\boldsymbol{E}^{\mathrm{T}}\boldsymbol{\Sigma} \;&+\; \delta\boldsymbol{\Sigma}^{\mathrm{T}}\int_{\Omega}\mathbf{B}(\mathbf{x})^{\mathrm{T}}\boldsymbol{m}(\mathbf{x})\,\mathrm{d}\Omega\;\Delta\theta \;=\; \Omega\,\delta\boldsymbol{E}^{\mathrm{T}}\mathbf{L}\boldsymbol{E}, \\ \delta\boldsymbol{\Sigma} \;&=\; \mathbf{L}\delta\boldsymbol{E}, \end{aligned} \tag{3.40}$$

where $\mathbf{B}(\mathbf{x})$ represents the mechanical stress influence function. Eqs. (3.40) then readily provide the overall stress and strain fields in the form

$$\boldsymbol{\Sigma} + \mathbf{L}\boldsymbol{m}\Delta\theta = \mathbf{L}\boldsymbol{E}, \tag{3.41}$$

$$\boldsymbol{\Sigma} = \mathbf{L}\left(\boldsymbol{E} - \boldsymbol{m}\Delta\theta\right), \qquad \boldsymbol{E} \;=\; \mathbf{M}\boldsymbol{\Sigma} + \boldsymbol{m}\Delta\theta, \tag{3.42}$$

where the macroscopic thermal strain vector $\boldsymbol{m}\Delta\theta$ is given by

$$\boldsymbol{m}\Delta\theta = \Delta\theta\frac{1}{\Omega}\int_{\Omega}\mathbf{B}(\mathbf{x})^{\mathrm{T}}\boldsymbol{m}(\mathbf{x})\,\mathrm{d}\Omega. \tag{3.43}$$

After setting $\Delta\theta$ to unity and introducing the phase volume fraction $c_r = \frac{\Omega_r}{\Omega}$ we arrive at the familiar Levin formula

$$\boldsymbol{m} = \sum_r \frac{\Omega_r}{\Omega}\int_{\Omega_r}\mathbf{B}(\mathbf{x})^{\mathrm{T}}\boldsymbol{m}_r\,\mathrm{d}\Omega \;=\; \sum_r c_r{\mathbf{B}_r}^{\mathrm{T}}\boldsymbol{m}_r. \tag{3.44}$$

Under pure thermal loading Eq. (3.42_2) reduces to $\boldsymbol{E} = \boldsymbol{m}\Delta\theta$ where the overall average strain $\boldsymbol{E}$ follows from the solution of the system of equations (3.31). On the contrary,

when setting $\Delta\theta = 0$ the system (3.31) can be used to extract the phase concentration factor tensors $\mathbf{B}_r$. Thus both Eqs. (3.42_1) and (3.44) can be exploit to obtain the effective coefficients of thermal expansion listed in vector $\boldsymbol{m}$.

An alternate approach relies on standard volume averaging. In particular, recall the strain volume average in the form

$$\begin{aligned} \langle \boldsymbol{\epsilon}(\mathbf{x}) \rangle &= \frac{1}{\Omega} \int_\Omega \left[\mathbf{M}(\mathbf{x}) \boldsymbol{\sigma}(\mathbf{x}) + \boldsymbol{m}(\mathbf{x}) \Delta\theta \right] \, \mathrm{d}\Omega \\ &= \boldsymbol{E} + \langle \boldsymbol{\epsilon}^*(\mathbf{x}) \rangle \,, \qquad\qquad \langle \boldsymbol{\epsilon}^*(\mathbf{x}) \rangle = \mathbf{0}, \end{aligned} \tag{3.45}$$

which directly provides the macroscopic constitutive law Eq. (3.42_2)

$$\frac{1}{\Omega} \int_\Omega \left[\mathbf{M}(\mathbf{x}) \boldsymbol{\sigma}(\mathbf{x}) + \boldsymbol{m}(\mathbf{x}) \Delta\theta \right] \, \mathrm{d}\Omega = \mathbf{M}\boldsymbol{\Sigma} + \boldsymbol{m}\Delta\theta. \tag{3.46}$$

When admitting only thermal effects, $\boldsymbol{\Sigma} = \mathbf{0}$, and introducing the thermal stress influence function $\mathbf{b}(\mathbf{x})$ such that

$$\boldsymbol{\sigma}(\mathbf{x}) = \mathbf{b}(\mathbf{x}) \Delta\theta, \tag{3.47}$$

we find

$$\langle \boldsymbol{\sigma}(\mathbf{x}) \rangle = \sum_r \frac{\Omega_r}{\Omega} \int_{\Omega_r} \mathbf{b}(\mathbf{x}) \, \mathrm{d}\Omega = \sum_r c_r \mathbf{b}_r \, = \, \mathbf{0}. \tag{3.48}$$

After combining Eqs. (3.46) and (3.48) we arrive at the overall thermal strain vector now given by

$$\boldsymbol{m} = \frac{1}{\Omega} \int_\Omega \mathbf{M}(\mathbf{x}) \mathbf{b}(\mathbf{x}) \, \mathrm{d}\Omega + \langle \boldsymbol{m}(\mathbf{x}) \rangle \,. \tag{3.49}$$

Assuming again piecewise uniform variation of phase thermal and elastic properties we finally get

$$\boldsymbol{m} = \sum_r c_r \left(\mathbf{M}_r \mathbf{b}_r + \boldsymbol{m}_r \right). \tag{3.50}$$

Numerical results

Here we present some numerical results obtained for the graphite-epoxy composite system. The material properties are listed in Table 3.10. The analysis was carried out under generalized plane strain conditions.

Table 3.10: Material properties of T30/Epoxy system

phase	E_A [GPa]	E_T [GPa]	G_T [GPa]	ν_A	α_A [K^{-1}]	α_T [K^{-1}]
fiber	386	7.6	2.6	0.41	-1.2×10^{-6}	7×10^{-6}
matrix	5.5	5.5	1.96	0.40	2.4×10^{-5}	2.4×10^{-5}

The resulting effective thermal expansion coefficients for selected periodic unit cells together with the results obtained with the Mori-Tanaka method and hexagonal arrangement of fibers are stored in Table 3.11. In turns out that the periodic unit cell derived from the optimization procedure is again able to reflect the slight geometrical anisotropy possessed by the current material.

Table 3.11: Components of the effective thermal expansion coefficients [K^{-1}]

Unit cell	α_x	α_y	α_A	c_f
Original	2.269×10^{-5}	2.248×10^{-5}	-7.463×10^{-7}	0.436
2 fibers PUC	2.273×10^{-5}	2.244×10^{-5}	-7.463×10^{-7}	0.436
5 fibers PUC	2.269×10^{-5}	2.248×10^{-5}	-7.462×10^{-7}	0.436
10 fibers PUC	2.269×10^{-5}	2.249×10^{-5}	-7.462×10^{-7}	0.436
Hexagonal array	2.259×10^{-5}	2.259×10^{-5}	-7.462×10^{-7}	0.436
Mori-Tanaka	2.250×10^{-5}	2.250×10^{-5}	-7.464×10^{-7}	0.436

Finally, Table 3.12 shows that the values of effective coefficients of thermal expansion obtained using relations (3.36), (3.44) and (3.50) are identical.

Table 3.12: Comparison of relations (3.36), (3.44) and (3.50) for 5-fiber PUC [K^{-1}]

Relation	α_x	α_y	α_A
Equation 21	2.269×10^{-5}	2.249×10^{-5}	-7.462×10^{-7}
Equation 30	2.269×10^{-5}	2.249×10^{-5}	-7.462×10^{-7}
Equation 36	2.269×10^{-5}	2.249×10^{-5}	-7.462×10^{-7}

3.3.2 Thermo-viscoelastic response

Majority of material systems currently at the forefront of engineering interest experience the time dependent behavior at sustained loading. Examples include polymer matrix composite systems also examined in the present work. Constitutive relations that describe the time dependent deformation of such systems usually assume linearly elastic response of fibers while liner thermo-viscoelastic models are appropriate for polymer matrices in most practical applications. Inventory of contributions to viscoelastic analysis of composites includes [Chaboche, 1997, Wafa, 1994, Schapery, 1981, among others]. This section revisits the subject in conjunction with the present modeling framework developed for random composites.

Macroscopic constitutive law

Constitutive equations for viscoelastic constituents can be formulated either in the integral form, or in the incremental form. The incremental form, that is more convenient for numerical implementation, can be derived by converting the integral equations into a rate-type form and by subsequent integration under certain simplifying assumptions. Typically, the degenerate (Dirichlet) kernels

$$\begin{aligned} J(t,\tau) &= \sum_{\mu=1}^{M} \frac{1}{D_\mu(\tau)} \left\{1 - exp\left[y_\mu(\tau) - y_\mu(t)\right]\right\}, \\ R(t,\tau) &= \sum_{\mu=1}^{M} E_\mu(\tau)\, exp\left[y_\mu(\tau) - y_\mu(t)\right], \end{aligned} \tag{3.51}$$

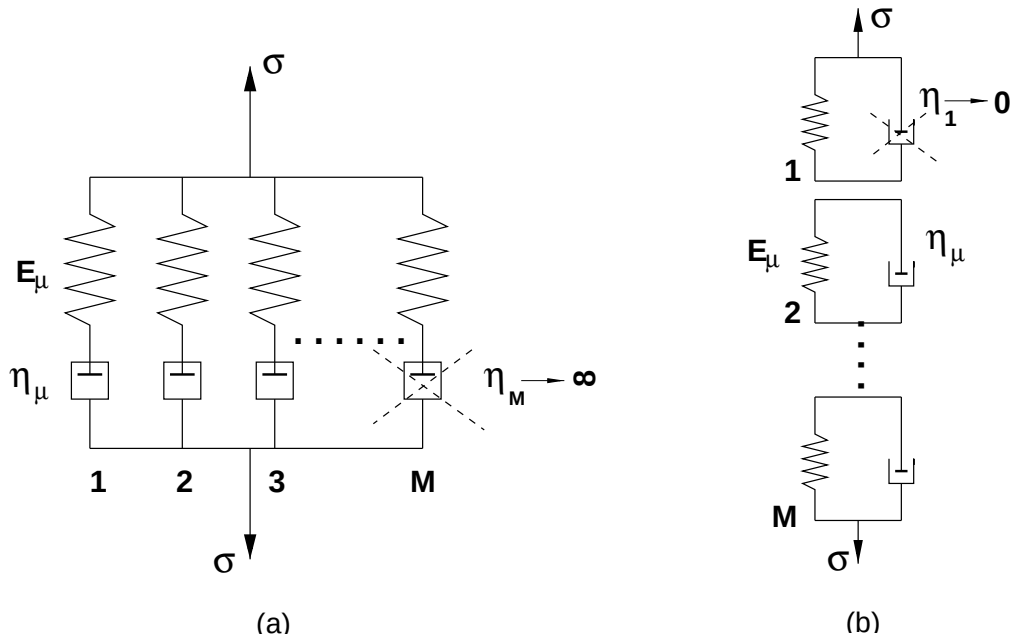

Figure 3.8: Rheological models: a) Maxwell chain, b) Kelvin chain

where $y_\mu(t) = (t/\Theta_\mu)^{q_\mu}$, are used to approximate the creep and relaxation functions $J(t,\tau)$ and $R(t,\tau)$, respectively. Retardation times Θ_μ must satisfy certain rules necessary for the success of calculation [Bazant and Wu, 1973]. The coefficient q_μ is introduced in order to reduce the number of terms of the Dirichlet expansions. Functions D_μ and E_μ are usually obtained by fitting the creep or relaxation functions via Eqs. (3.51) using the method of least squares.

Recall that the compliance function of a linear viscoelastic material represents the strain at time t due to a unit stress applied at time τ and kept constant, while the relaxation function represents the stress at time t due to a unit strain applied at time τ and held constant. When written in the form of Dirichlet series, these functions are identical with representation provided by Kelvin and Maxwell chains, respectively (see Fig. 3.8). For example, the Maxwell chain model gives the local stress in the form

$$\boldsymbol{\sigma}(\mathbf{x}) = \sum_{\mu=1}^{M} \boldsymbol{\sigma}_\mu(\mathbf{x}), \tag{3.52}$$

where $\boldsymbol{\sigma}_\mu$, called hidden stress, represents the stress in the μ^{th} Maxwell unit, which satisfies the differential constitutive equation

$$\dot{\boldsymbol{\sigma}}_\mu(\mathbf{x}) + \dot{y}_\mu \boldsymbol{\sigma}_\mu(\mathbf{x}) = E_\mu(\mathbf{x})\widehat{\mathbf{L}}(\mathbf{x})(\dot{\boldsymbol{\epsilon}}(\mathbf{x}) - \dot{\boldsymbol{\epsilon}}_0(\mathbf{x})), \qquad \dot{y}_\mu(t) = \frac{E_\mu(t)}{\eta_\mu(t)}, \tag{3.53}$$

where $\mathbf{L}(\mathbf{x}, t) = E_\mu(\mathbf{x}, t)\widehat{\mathbf{L}}(\mathbf{x})$ is the instantaneous stiffness matrix of a linear elastic isotropic material at the material point $\mathbf{x}$.

Numerical solution of the viscoelastic problem is based on dividing the time axis into intervals of length Δt_i. Suppose that at the beginning of the i^{th} interval $\langle t_{i-1}, t_i\rangle$, the stress vector $\boldsymbol{\sigma}_\mu(\mathbf{x}, t_{i-1})$, $\mu = 1, 2, \ldots, M$, is known. The incremental form of Eq. (3.53) is then written as [Bittnar and Šejnoha, 1996]

$$\Delta\boldsymbol{\sigma}_i(\mathbf{x}) = \mathbf{L}_i(\mathbf{x})\left(\Delta\boldsymbol{\epsilon}_i(\mathbf{x}) - \Delta\boldsymbol{\mu}_i(\mathbf{x})\right), \tag{3.54}$$

where the current increment of local eigenstrain reads

$$\Delta\boldsymbol{\mu}_i(\mathbf{x}) = \Delta\boldsymbol{\epsilon}_i^0(\mathbf{x}) + \Delta\widehat{\boldsymbol{\epsilon}}_i(\mathbf{x}). \tag{3.55}$$

The initial strain vector $\Delta\boldsymbol{\epsilon}_i^0$ may represent many different physical phenomena including thermal strains, shrinkage, swelling, plastic strains, etc. When admitting only thermal and creep effects we get

$$\Delta\boldsymbol{\epsilon}_i^0(\mathbf{x}) = \boldsymbol{m}(\mathbf{x})\Delta\theta_i, \qquad \Delta\widehat{\boldsymbol{\epsilon}}_i(\mathbf{x}) = \frac{1}{\widehat{E}_i(\mathbf{x})}\sum_{\mu=1}^{M}\left(1 - e^{-\Delta y_\mu}\right)\boldsymbol{\sigma}_\mu(\mathbf{x}, t_{i-1}). \tag{3.56}$$

The stiffness $\widehat{E}_i$ for the i^{th} interval is determined by

$$\widehat{E}_i(\mathbf{x}) = \sum_{\mu=1}^{M} E_\mu(\mathbf{x}, t_i - \Delta t_i/2)\left(1 - e^{-\Delta y_\mu}\right)/\Delta y_\mu. \tag{3.57}$$

The above description of the material properties on the microscale is sufficient to determine the local stress and strain fields by increments of the overall strain, $\boldsymbol{E}$, or stress $\boldsymbol{\Sigma}$. To that end, consider an incremental form of Eq. (3.35)

$$\left\langle \delta\boldsymbol{\epsilon}^{\mathrm{T}}\Delta\boldsymbol{\sigma}\right\rangle = \delta\boldsymbol{E}^{\mathrm{T}}\Delta\boldsymbol{\Sigma}. \tag{3.58}$$

Substituting the local strain increment $\Delta\boldsymbol{\epsilon}(\mathbf{x}) = \Delta\boldsymbol{E} + \Delta\boldsymbol{\epsilon}^*(\mathbf{x})$ together with local constitutive equation (3.54) into Eq. (3.58) provides the desired incremental form of Eq. (3.36) as

$$\begin{bmatrix} \frac{1}{\Omega}\int_\Omega \mathbf{L}_i \,\mathrm{d}\Omega & \frac{1}{\Omega}\int_\Omega \mathbf{L}_i\mathbf{B} \,\mathrm{d}\Omega \\ \frac{1}{\Omega}\int_\Omega \mathbf{B}^{\mathrm{T}}\mathbf{L}_i \,\mathrm{d}\Omega & \frac{1}{\Omega}\int_\Omega \mathbf{B}^{\mathrm{T}}\mathbf{L}_i\mathbf{B} \,\mathrm{d}\Omega \end{bmatrix} \begin{Bmatrix} \Delta\boldsymbol{E}_i \\ \Delta\boldsymbol{r}_i \end{Bmatrix} = \begin{Bmatrix} \Delta\boldsymbol{\Sigma}_i + \frac{1}{\Omega}\int_\Omega \mathbf{L}_i\Delta\boldsymbol{\mu}_i \,\mathrm{d}\Omega \\ \frac{1}{\Omega}\int_\Omega \mathbf{B}^{\mathrm{T}}\mathbf{L}_i\Delta\boldsymbol{\mu}_i \,\mathrm{d}\Omega \end{Bmatrix}. \tag{3.59}$$

Finally, after rewriting the above equation as

$$\begin{bmatrix} \mathbf{K}_{11} & \mathbf{K}_{12} \\ \mathbf{K}_{21} & \mathbf{K}_{22} \end{bmatrix}_i \begin{Bmatrix} \Delta\boldsymbol{E} \\ \Delta\boldsymbol{r} \end{Bmatrix}_i = \begin{Bmatrix} \Delta\boldsymbol{\Sigma} + \Delta\boldsymbol{F}^0 \\ \Delta\boldsymbol{f}^0 \end{Bmatrix}_i, \tag{3.60}$$

and eliminating the fluctuating displacements vector $\Delta\boldsymbol{r}_i$ we arrive at the incremental form of the macroscopic constitutive law

$$\Delta\boldsymbol{\Sigma}_i = \mathbf{L}_i\Delta\boldsymbol{E}_i + \Delta\boldsymbol{\Lambda}_i, \tag{3.61}$$

where

$$\mathbf{L}_i = \left(\mathbf{K}_{11} - \mathbf{K}_{12}\mathbf{K}_{22}^{-1}\mathbf{K}_{12}^{\mathrm{T}}\right)_i, \qquad \Delta\boldsymbol{\Lambda}_i = -\Delta\boldsymbol{F}_i^0 + \left(\mathbf{K}_{12}\mathbf{K}_{22}^{-1}\Delta\boldsymbol{f}^0\right)_i.$$

Numerical results

As an example, consider an artificial composite system listed in Table 3.13 with the matrix properties taken from [Fára, 1990].

Table 3.13: Material properties of T30/Epoxy system

phase	E_A [GPa]	E_T [GPa]	G_T [GPa]	ν_A
fiber	386	7.6	2.6	0.41
matrix	2.1	2.1	0.75	0.40

The time dependent material properties of the epoxy matrix were derived experimentally from a set of well cured specimens, so that the material aging was neglected [Fára, 1990].

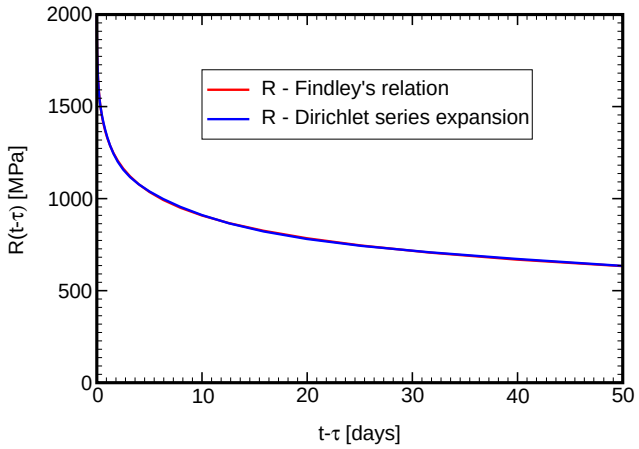

Figure 3.9: Relaxation function

The resulting experimental data were approximated by Findley's expression

$$J(t,\tau) = a + b(t-\tau)^n, \tag{3.62}$$

were for the present material $a = 0.04744, b = 0.002142, n = 0.3526$ with $(t-\tau)$ given in minutes. The corresponding relaxation function $R(t,\tau)$ appears in Fig. 3.9. Ten elements of the Dirichlet series expansion Eq. (3.51) uniformly distributed in $\log(t-\tau)$ over the period of hundred days were assumed. The fit of the relaxation function Eq. (3.62) by Eq. (3.51_2) is plotted in Fig. 3.9.

Numerical results are presented only for transverse tension. Both the strain and stress control conditions are considered in simulations. Fig. 3.10 illustrates the time variation of the applied load. The corresponding composite response then appears in Fig. 3.11. Judging from our previous results, the ten-particle unit cell is assumed to represent the material behavior of a real composite. Both the creep Fig. 3.11(a) and relaxation Fig. 3.11(b) tests confirm a good correlation between statistically optimal unit cells and the PHA model. On the contrary, an anisotropic character of the present medium evident from Fig. 3.12 cannot be attained by simple periodic unit cells (recall Tables 3.7 and 3.11). The present approach is therefore preferable.

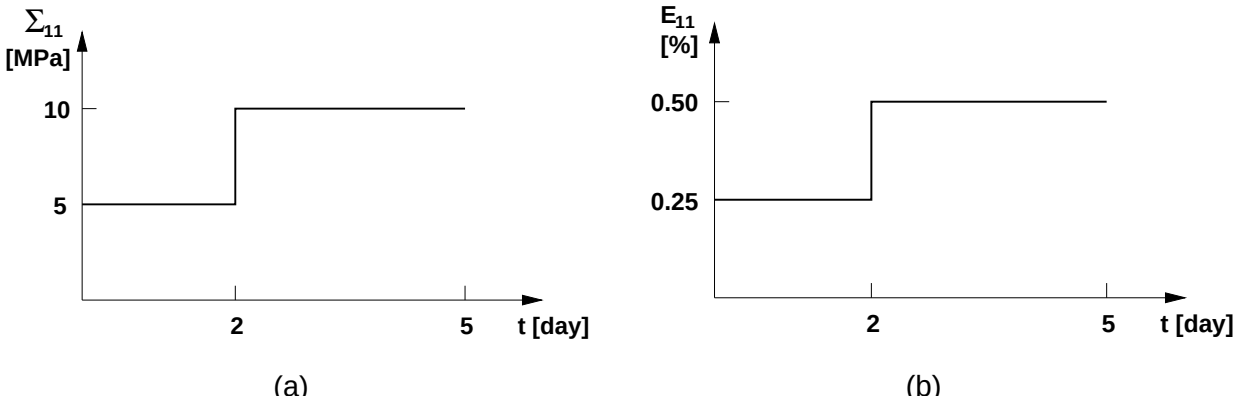

Figure 3.10: Applied loading: a) creep test, b) relaxation test

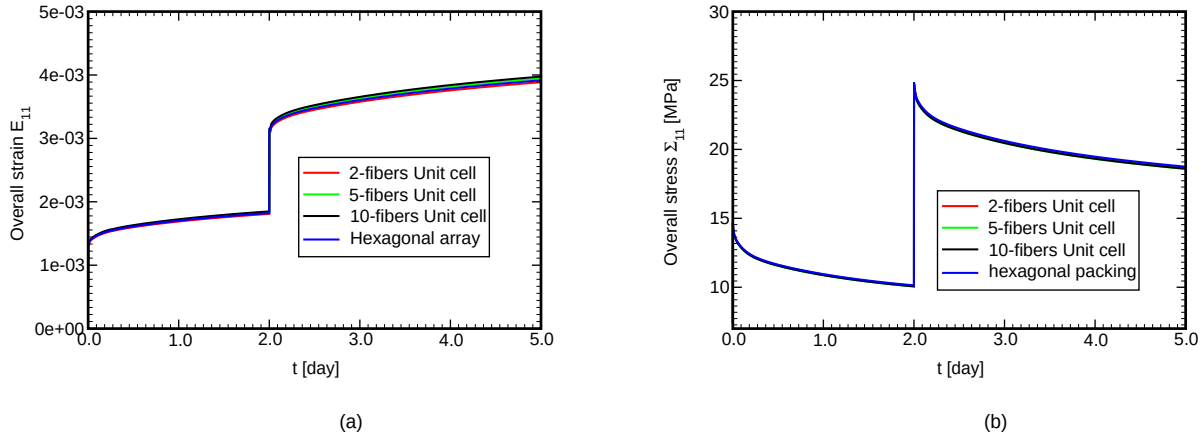

Figure 3.11: Overall response: a) creep test, b) relaxation test

3.3.3 Closure

In the present contribution we revisited a popular problem of evaluating the effective properties of two-phase disordered media. In particular, we turned our attention to a real composite material represented here by a bundle of non-overlapping graphite fibers surrounded by the epoxy matrix, Fig. 2.1.

The random character of the microstructure does not permit a direct use of various averaging techniques such as the Mori-Tanaka or self-consistent methods. Instead, procedures incorporating various statistical descriptors such as the joint probability density function must be used to give proper description of the mechanical behavior of random composites.

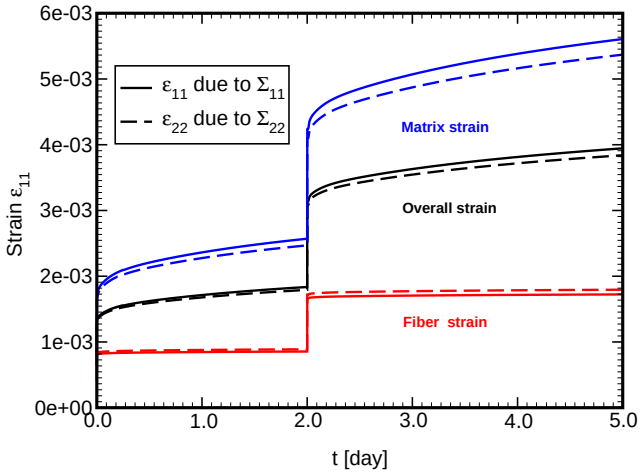

Figure 3.12: Local response: creep test

Chapter 2 provides such microstructural information of the fiber tow up to two-point level tagging this composite with a nice label of being statistically "isotropic" and "ergodic". This result allowed to substitute the two-point probability density function with the well known second order intensity function much more suitable for direct numerical simulations. Pleasant features of this function examined in Section 2.4 were further exploited, although indirectly, when evaluating the effective mechanical properties of the composite.

In this particular treatment, however, we abandoned a rather standard approach of incorporating the material's statistics directly into various variational principles [Beran, 1968, Torquato, 1991, Ponte Casteñada and Willis, 1995, Drugan and Willis, 1996]. Instead, in view of ensuing analysis of inelastic response of random composites, we followed suggestions given in [Povirk, 1995] and generated a small unit cell with the same statistics (up to two-point level) as possessed by the real microstructure. The augmented simulating annealing method discussed in Section 3.1.2 proved to be a very powerful tool in this matter. Attributed to the random nature of genetic algorithms the repeated use of the **AUSA** method results in a family of unit cells with slightly different arrangements of fibers but identical in their statistical details. This was demonstrated in Section 3.2.2 showing the invariance

of effective properties with respect to individual fiber configurations. It is worth to note that the second order intensity function (or the pair distribution function), although evaluated under assumption of spatial isotropy of fibers locations, can capture, when used in the optimization problem Eq. (3.1), clustering character of the real microstructure (compare Figs. 2.3 and 3.7). A slight anisotropy of spatial distribution of fibers is further supported by results stored in Tables 3.7 and 3.11. Similar conclusion can be further drawn from Fig. 3.12.

A number of other numerical tests explored in Sections 3.2 and 3.3 highlight the need for proper statistical description when dealing with random composites (recall Tables 3.7–3.9). Although, by judging from Tables 3.7, 3.11 and Figs. 3.11, one may question the tedious procedure introduced in the paper, which eventually provides results very similar to those obtained when simply assuming the hexagonal arrangement of fibers, we note that an appreciable difference may appear when the contrast between the phases (ratio between the transverse Young's modulus of the harder phase to the transverse Young's modulus of the softer phase) increases. We further expect the proposed approach to become irreplaceable by simple unit cells such as the periodic hexagonal array model [Teplý and Dvořák, 1988] when describing the inelastic response (plasticity, damage) of material systems similar to one under current investigation. But this has to be yet confirm. On the other hand, as mentioned in [Teplý and Dvořák, 1988], an application of simple periodic unit cell when used to estimate overall elastic properties in systems with large volume fraction of the inclusions seems to be justified. This agrees well with the present study.

Chapter 4

MACROSCOPIC MATERIAL PROPERTIES BASED ON EXTENDED HASHIN–SHTRIKMAN VARIATIONAL PRINCIPLES

Basic energy principles were reviewed in the preceding chapter to derive effective thermoelastic material properties of a random composite assuming periodic distribution of the microstructure. Another approach is available when analyzing material elements having a length scale sufficiently large compare to the microstructural length scale so it can be treated as statistically representative of the composite. Such a definition of a representative volume element (RVE) is adopted in the present section when deriving the generalized macroscopic constitutive equations of composite systems with statistically homogeneous distribution of phases.

To be consistent with the problems discussed in the previous section we select again the graphite fiber tow embedded in the polymer matrix as a representative of the two-phase disordered composite media. Random character of fibers arrangement, typical for such material systems, is conveniently described by the two-point probability function. When used with the Hashin-Shtrikman variational principles this function provides sufficient information for obtaining bounds on the thermo-elastic material properties of real composites with statistically homogeneous microstructure.

In particular, Hashin and Shtrikman [Hashin and Shtrikman, 1963] presented two alternative representations of energy functions by incorporating polarization fields relative to a homogeneous reference (comparison) medium. In this section, we focus on theoretical aspects associated with the variational formulation for anisotropic and non-homogeneous bodies with

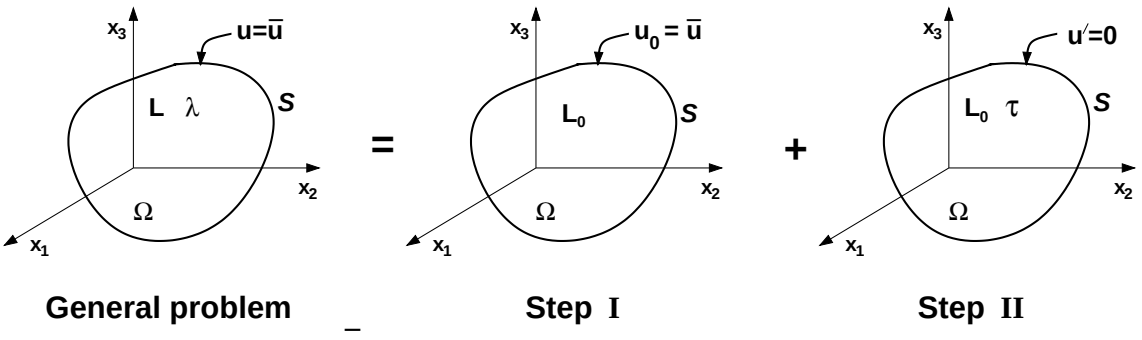

Figure 4.1: Body with prescribed surface displacements including eigenstresses

either prescribed displacements $\boldsymbol{u} = \overline{\boldsymbol{u}}$ or tractions $\boldsymbol{p} = \overline{\boldsymbol{p}}$ along the entire boundary S of the composite. In addition, eigenstrains (stress free strains) or eigenstresses are admitted in the present formulation.

4.1 Body with prescribed surface displacements and eigenstresses

The computational procedure is split into two steps. First, suppose that an affine displacement field $\boldsymbol{u}_0(\mathbf{x}) = \boldsymbol{E} \cdot \mathbf{x}$ is prescribed. The corresponding uniform strain $\boldsymbol{E}$ and stress $\boldsymbol{\Sigma}$ fields are related through constitutive law in the form

$$\boldsymbol{\Sigma} = \mathbf{L}_0 \boldsymbol{E} \quad \text{in } \Omega, \quad \boldsymbol{u}_0 = \overline{\boldsymbol{u}} \text{ on } S, \tag{4.1}$$

where $\mathbf{L}_0$ is the material stiffness tensor of a homogeneous reference material.

Next, a geometrically identical body, generally anisotropic and heterogeneous, with the same prescribed surface displacements is considered. Associated displacements $\boldsymbol{u}$, strains $\boldsymbol{\epsilon}$ and stresses $\boldsymbol{\sigma}$ are yet to be determined. Generalized Hook's law including eigenstresses $\boldsymbol{\lambda}$ is then written as

$$\boldsymbol{\sigma}(\mathbf{x}) = \mathbf{L}(\mathbf{x})\boldsymbol{\epsilon}(\mathbf{x}) + \boldsymbol{\lambda}(\mathbf{x}) \text{ in } \Omega, \boldsymbol{u} = \overline{\boldsymbol{u}} \text{ on } S. \tag{4.2}$$

Following the Hashin-Shtrikman idea, we introduce the symmetric stress polarization tensor $\boldsymbol{\tau}$ such that

$$\boldsymbol{\sigma}(\mathbf{x}) = \mathbf{L}_0\boldsymbol{\epsilon}(\mathbf{x}) + \boldsymbol{\tau}(\mathbf{x}). \tag{4.3}$$

In addition, denote

$$\boldsymbol{u}' = \boldsymbol{u} - \boldsymbol{u}_0 \text{ in } \Omega, \boldsymbol{u}' = \boldsymbol{0} \text{ on } S \tag{4.4}$$

and

$$\boldsymbol{\epsilon}' = \boldsymbol{\epsilon} - \boldsymbol{E}, \ \boldsymbol{\sigma}' = \boldsymbol{\sigma} - \boldsymbol{\Sigma} \text{ in } \Omega. \tag{4.5}$$

The objective is to formulate a variational principle describing the behavior of the nonhomogeneous and anisotropic material subjected to known eigenstresses and prescribed boundary displacements. Schematic representation of this problem is displayed in Fig. 4.1. Provided that both $\boldsymbol{\sigma}$ and $\boldsymbol{\Sigma}$ fields are statically admissible (see [Bittnar and Šejnoha, 1996]), the following equations have to be satisfied

$$\boldsymbol{\nabla} \cdot (\mathbf{L}_0\boldsymbol{\epsilon} + \boldsymbol{\tau}) = \boldsymbol{0} \quad \text{in } \Omega, \tag{4.6}$$

$$\boldsymbol{\tau} - (\mathbf{L} - \mathbf{L}_0)\boldsymbol{\epsilon} - \boldsymbol{\lambda} = \boldsymbol{0} \quad \text{in } \Omega, \tag{4.7}$$

$$\boldsymbol{u}' = \boldsymbol{0} \quad \text{on } S. \tag{4.8}$$

A formulation equivalent to Eqs. (4.6) and (4.7) may be obtained by performing a variation of the extended functional

$$\begin{aligned} U_{\boldsymbol{\tau}} = \frac{1}{2}\int_\Omega \Big(& \boldsymbol{E}^{\mathrm{T}}\boldsymbol{\Sigma} - (\boldsymbol{\tau} - \boldsymbol{\lambda})^{\mathrm{T}}(\mathbf{L} - \mathbf{L}_0)^{-1}(\boldsymbol{\tau} - \boldsymbol{\lambda}) \\ & -2\boldsymbol{\tau}^{\mathrm{T}}\boldsymbol{E} - \boldsymbol{\epsilon}'^{\mathrm{T}}\boldsymbol{\tau} - \boldsymbol{\lambda}^{\mathrm{T}}\mathbf{L}^{-1}\boldsymbol{\lambda}\Big)\,\mathrm{d}\Omega. \end{aligned} \tag{4.9}$$

Setting

$$\delta U_{\boldsymbol{\tau}} = -\frac{1}{2}\int_\Omega \{2\delta\boldsymbol{\tau}^{\mathrm{T}}[(\mathbf{L} - \mathbf{L}_0)^{-1}(\boldsymbol{\tau} - \boldsymbol{\lambda}) - \boldsymbol{\epsilon}] + \delta\boldsymbol{\tau}^{\mathrm{T}}\boldsymbol{\epsilon}' - \delta\boldsymbol{\epsilon}'^{\mathrm{T}}\boldsymbol{\tau}\}\mathrm{d}\Omega = 0, \tag{4.10}$$

we find that Eq. (4.7) is one of the stationarity conditions of $U_{\boldsymbol{\tau}}$, while the second condition, Eq. (4.6), follows after recasting the remaining terms in the brackets. Finally, it can be proved that the stationary value $U^S_{\boldsymbol{\tau}}$ of the potential $U_{\boldsymbol{\tau}}$ equals the actual potential energy stored in the anisotropic and heterogeneous body

$$U^S_{\boldsymbol{\tau}} = \frac{1}{2}\int_\Omega (\boldsymbol{\epsilon} - \boldsymbol{\mu})^{\mathrm{T}}\mathbf{L}(\boldsymbol{\epsilon} - \boldsymbol{\mu})\mathrm{d}\Omega, \tag{4.11}$$

where $\boldsymbol{\mu} = -\mathbf{L}^{-1}\boldsymbol{\lambda}$ is the vector of eigenstrains (stress-free strains). The function $U_{\boldsymbol{\tau}}$ attains its maximum ($\delta^2 U_{\boldsymbol{\tau}} < 0$) if $(\mathbf{L} - \mathbf{L}_0)$ is positive definite and its minimum if $(\mathbf{L} - \mathbf{L}_0)$ is negative definite.

To make use of H-S functional, Eq. (4.9), or its variation, Eq. (4.10), one has to express $\boldsymbol{\epsilon}'$ via the polarization tensor $\boldsymbol{\tau}$

$$\boldsymbol{\epsilon}'(\mathbf{x}) = \boldsymbol{\epsilon}(\mathbf{x}) - \boldsymbol{E} = [\boldsymbol{\epsilon}_0^* \boldsymbol{\tau}], \tag{4.12}$$

where the operator $[\boldsymbol{\epsilon}_0^* \boldsymbol{\tau}]$ is defined in Appendix A. Subscript 0 is used to identify this operator with the homogeneous reference medium. Introducing an ensemble average of the local strain $\boldsymbol{\epsilon}$ in the form

$$\overline{\boldsymbol{\epsilon}(\mathbf{x})} = \boldsymbol{E} + \int_\Omega \boldsymbol{\epsilon}_0^*(\mathbf{x} - \mathbf{x}')\overline{\boldsymbol{\tau}(\mathbf{x}')}\, \mathrm{d}\Omega(\mathbf{x}'), \tag{4.13}$$

allows to rewrite Eq. (4.9) as

$$\begin{aligned} U_{\boldsymbol{\tau}} &= \frac{1}{2}\int_\Omega \Big(\boldsymbol{E}^{\mathrm{T}}\boldsymbol{\Sigma} - (\boldsymbol{\tau}(\mathbf{x}) - \boldsymbol{\lambda}(\mathbf{x}))^{\mathrm{T}}(\mathbf{L}(\mathbf{x}) - \mathbf{L}_0)^{-1}(\boldsymbol{\tau}(\mathbf{x}) - \boldsymbol{\lambda}(\mathbf{x})) - 2\boldsymbol{\tau}^{\mathrm{T}}(\mathbf{x})\overline{\boldsymbol{\epsilon}(\mathbf{x})} \\ &- \boldsymbol{\tau}^{\mathrm{T}}(\mathbf{x}) \int_\Omega \boldsymbol{\epsilon}_0^*(\mathbf{x} - \mathbf{x}') \left(\boldsymbol{\tau}(\mathbf{x}') - 2\overline{\boldsymbol{\tau}(\mathbf{x}')} \right) \mathrm{d}\Omega(\mathbf{x})' - \boldsymbol{\lambda}^{\mathrm{T}}(\mathbf{x})\mathbf{L}^{-1}(\mathbf{x})\boldsymbol{\lambda}(\mathbf{x}) \Big)\, \mathrm{d}\Omega(\mathbf{x}). \end{aligned} \tag{4.14}$$

Details are given in Appendix A. If each of the phase r of a randomly arranged composite is homogeneous with moduli $\mathbf{L}_r, r = 1, \ldots, n$, then the material stiffness matrix in the sample α can be expressed as [Drugan and Willis, 1996],

$$\mathbf{L}(\mathbf{x}, \alpha) = \sum_{r=1}^{n} \mathbf{L}_r \chi_r(\mathbf{x}, \alpha). \tag{4.15}$$

With the help of Eq. (2.11), the ensemble average of $\mathbf{L}$ is

$$\overline{\mathbf{L}(\mathbf{x})} = \sum_{r=1}^{n} \mathbf{L}_r S_r(\mathbf{x}). \tag{4.16}$$

Similarly, the trial field for $\boldsymbol{\tau}$ and eigenstress $\boldsymbol{\lambda}$ at any point $\mathbf{x}$ located in the sample α are provided by

$$\boldsymbol{\tau}(\mathbf{x}, \alpha) = \sum_{r=1}^{n} \boldsymbol{\tau}_r(\mathbf{x})\chi_r(\mathbf{x}, \alpha), \qquad \boldsymbol{\lambda}(\mathbf{x}, \alpha) = \sum_{r=1}^{n} \boldsymbol{\lambda}_r(\mathbf{x})\chi_r(\mathbf{x}, \alpha), \tag{4.17}$$

with the respective ensemble averages written as

$$\overline{\boldsymbol{\tau}(\mathbf{x})} = \sum_{r=1}^{n} \boldsymbol{\tau}_r(\mathbf{x}) S_r(\mathbf{x}), \qquad \overline{\boldsymbol{\lambda}(\mathbf{x})} = \sum_{r=1}^{n} \boldsymbol{\lambda}_r(\mathbf{x}) S_r(\mathbf{x}). \tag{4.18}$$

To facilitate the solution of the present problem the material is assumed to be ergodic and statistically homogeneous. Therefore,

$$\overline{\mathbf{L}} = \sum_{r=1}^{n} \mathbf{L}_r c_r, \; \overline{\boldsymbol{\tau}(\mathbf{x})} = \sum_{r=1}^{n} \boldsymbol{\tau}_r(\mathbf{x}) c_r, \; \overline{\boldsymbol{\lambda}(\mathbf{x})} = \sum_{r=1}^{n} \boldsymbol{\lambda}_r(\mathbf{x}) c_r. \tag{4.19}$$

Substituting Eqs. (4.19) into Eq. (4.14) yields the extended averaged form of the Hashin-Shtrikman principle

$$\begin{aligned} \overline{U}_{\boldsymbol{\tau}} \;=\; & \frac{1}{2} \int_{\Omega} \boldsymbol{E}^{\mathrm{T}} \boldsymbol{\Sigma} \, \mathrm{d}\Omega(\mathbf{x}) \\ - \; & \frac{1}{2} \sum_{r} \int_{\Omega} \left(c_r (\boldsymbol{\tau}_r(\mathbf{x}) - \boldsymbol{\lambda}_r(\mathbf{x}))^{\mathrm{T}} (\mathbf{L}_r - \mathbf{L}_0)^{-1} (\boldsymbol{\tau}_r(\mathbf{x}) - \boldsymbol{\lambda}_r(\mathbf{x})) - 2 c_r \boldsymbol{\tau}_r{}^{\mathrm{T}}(\mathbf{x}) \overline{\boldsymbol{\epsilon}(\mathbf{x})} \right) \mathrm{d}\Omega(\mathbf{x}) \\ - \; & \frac{1}{2} \sum_{r} \sum_{s} \int_{\Omega} \boldsymbol{\tau}_r(\mathbf{x})^{\mathrm{T}} \int_{\Omega} \boldsymbol{\epsilon}_0^*(\mathbf{x} - \mathbf{x}') \left[S_{rs}(\mathbf{x} - \mathbf{x}') \boldsymbol{\tau}_s(\mathbf{x}') - 2 c_s \overline{\tau(\mathbf{x}')} \right] \mathrm{d}\Omega(\mathbf{x}') \mathrm{d}\Omega(\mathbf{x}). \end{aligned} \tag{4.20}$$

Performing variation with respect to $\boldsymbol{\tau}_r(\mathbf{x})$ and using Eq. $(4.19)_2$ provides the extended form of the stationarity conditions

$$\begin{aligned} & (\mathbf{L}_r - \mathbf{L}_0)^{-1} \boldsymbol{\tau}_r(\mathbf{x}) c_r - \sum_{s=1}^{n} \int_{\Omega} \boldsymbol{\epsilon}_0^*(\mathbf{x} - \mathbf{x}') \left[S_{rs}(\mathbf{x} - \mathbf{x}') - c_r c_s \right] \boldsymbol{\tau}_s(\mathbf{x}') \, \mathrm{d}\Omega(\mathbf{x}') = \\ & = \overline{\boldsymbol{\epsilon}(\mathbf{x})} c_r + (\mathbf{L}_r - \mathbf{L}_0)^{-1} \boldsymbol{\lambda}_r(\mathbf{x}) c_r, \qquad r = 1, \ldots, n. \end{aligned} \tag{4.21}$$

Drugan and Willis [Drugan and Willis, 1996] employed the Fourier transforms to solve Eq. (4.21) for two-phase composites with $\boldsymbol{\lambda}_r = \mathbf{0}$. Including these terms into their approach, the Fourier transform of polarization stress $\widetilde{\boldsymbol{\tau}_r}(\boldsymbol{\xi})$ can be found as

$$\widetilde{\boldsymbol{\tau}_r}(\boldsymbol{\xi}) = \sum_{s=1}^{2} \widetilde{\mathbf{T}}_{rs}(\boldsymbol{\xi}) c_s \left[\overline{\widetilde{\boldsymbol{\epsilon}}(\boldsymbol{\xi})} + (\mathbf{L}_s - \mathbf{L}_0)^{-1} \widetilde{\boldsymbol{\lambda}_s}(\boldsymbol{\xi}) \right], \tag{4.22}$$

where $\widetilde{\mathbf{T}}_{rs}$ are certain microstructure-dependent tensors. For details the reader is referred to [Drugan and Willis, 1996]. The Fourier transform of Eq. $(4.19)_2$ is

$$\overline{\widetilde{\boldsymbol{\tau}}(\boldsymbol{\xi})} = \sum_{r=1}^{2} \sum_{s=1}^{2} c_r \widetilde{\mathbf{T}}_{rs}(\boldsymbol{\xi}) c_s \left[\overline{\widetilde{\boldsymbol{\epsilon}}(\boldsymbol{\xi})} + (\mathbf{L}_s - \mathbf{L}_0)^{-1} \widetilde{\boldsymbol{\lambda}_s}(\boldsymbol{\xi}) \right], \tag{4.23}$$

Consequently, the inverse Fourier transform of Eq. (4.23) reads

$$\overline{\boldsymbol{\tau}(\mathbf{x})} = \sum_{r=1}^{2}\sum_{s=1}^{2}\int_{\Omega} c_r \mathbf{T}_{rs}(\mathbf{x}-\mathbf{x}')c_s \left[\overline{\boldsymbol{\epsilon}(\mathbf{x}')} + (\mathbf{L}_s - \mathbf{L}_0)^{-1}\boldsymbol{\lambda}_s(\mathbf{x}')\right] \mathrm{d}\Omega(\mathbf{x}'). \tag{4.24}$$

Provided that $\overline{\boldsymbol{\epsilon}(\mathbf{x})}$ and $\boldsymbol{\lambda}_r(\mathbf{x})$ do not vary with $\mathbf{x}$, then Eq. (4.24) does not require the inverse Fourier transform of $\widetilde{\mathbf{T}}_{rs}(\boldsymbol{\xi})$ to be expressed explicitly, since

$$\int_{\Omega} \mathbf{T}_{rs}(\mathbf{x}-\mathbf{x}')\mathrm{d}\Omega(\mathbf{x}') = \int_{\Omega} \mathbf{T}_{rs}(\mathbf{x})\mathrm{d}\Omega(\mathbf{x}) = \widetilde{\mathbf{T}}_{rs}(\boldsymbol{\xi}=\mathbf{0}). \tag{4.25}$$

Hence, according to (4.2) and (4.3) the overall constitutive law takes this form

$$\overline{\boldsymbol{\sigma}} = \widehat{\mathbf{L}}\overline{\boldsymbol{\epsilon}} + \overline{\boldsymbol{\lambda}}, \tag{4.26}$$

where

$$\widehat{\mathbf{L}} = \mathbf{L}_0 + \sum_{r=1}^{2}\sum_{s=1}^{2} c_r \widetilde{\mathbf{T}}_{rs}(\boldsymbol{\xi}=\mathbf{0})c_s, \tag{4.27}$$

$$\overline{\boldsymbol{\lambda}} = \sum_{r=1}^{2}\sum_{s=1}^{2} c_r \widetilde{\mathbf{T}}_{rs}(\boldsymbol{\xi}=\mathbf{0})c_s(\mathbf{L}_s - \mathbf{L}_0)^{-1}\boldsymbol{\lambda}_s. \tag{4.28}$$

Note that analytical expressions for tensors $\widetilde{\mathbf{T}}_{rs}(\boldsymbol{\xi}=\mathbf{0})$ is available only for certain configurations such as statistically isotropic composites with linear elastic isotropic phases [Drugan and Willis, 1996]. In general, numerical solution is required to solve unknown polarization stress $\boldsymbol{\tau}_r$. This approach is discussed in the following paragraph.

Suppose again that $(\overline{\boldsymbol{\epsilon}(\mathbf{x})} = \overline{\boldsymbol{\epsilon}}, \boldsymbol{\lambda}_r(\mathbf{x}) = \boldsymbol{\lambda}_r, \boldsymbol{\tau}_r(\mathbf{x}) = \boldsymbol{\tau}_r)$ for a general n-phase composite medium. The system (4.21) then reduces to

$$(\mathbf{L}_r - \mathbf{L}_0)^{-1}\boldsymbol{\tau}_r c_r - \sum_{s=1}^{n}\mathbf{A}_{rs}\boldsymbol{\tau}_s = c_r\overline{\boldsymbol{\epsilon}} + (\mathbf{L}_r - \mathbf{L}_0)^{-1}c_r\boldsymbol{\lambda}_r, \quad r = 1, 2, \ldots, n, \tag{4.29}$$

where microstructure-dependent matrices $\mathbf{A}_{rs}$ do not depend on $\mathbf{x}$ and are provided by

$$\mathbf{A}_{rs} = \int_{\Omega} \boldsymbol{\epsilon}_0^*(\mathbf{x}-\mathbf{x}')\left[S_{rs}(\mathbf{x}-\mathbf{x}') - c_r c_s\right] \mathrm{d}\Omega(\mathbf{x}'). \tag{4.30}$$

The solution of system (4.29) can be written in the form (compare with Eq. (4.22))

$$\boldsymbol{\tau}_r = \sum_{s=1}^{n}\mathbf{T}_{rs}c_s\left[\overline{\boldsymbol{\epsilon}} + (\mathbf{L}_s - \mathbf{L}_0)^{-1}\boldsymbol{\lambda}_s\right], \tag{4.31}$$

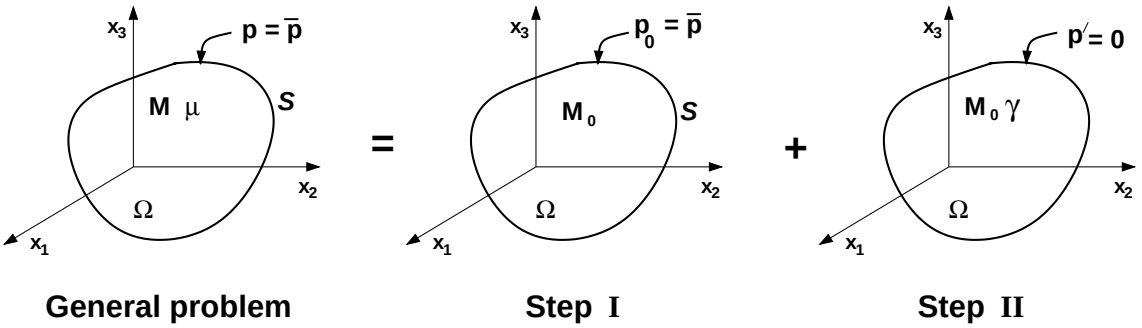

Figure 4.2: Body with prescribed surface tractions including eigenstrains

from which

$$\overline{\boldsymbol{\tau}} = \sum_{r=1}^{n}\sum_{s=1}^{n} c_r \mathbf{T}_{rs} c_s \left[\overline{\boldsymbol{\epsilon}} + (\mathbf{L}_s - \mathbf{L}_0)^{-1}\boldsymbol{\lambda}_s\right]. \tag{4.32}$$

Solving Eq. (4.29) calls for an efficient method to tackle Eq. (4.30). A suitable method of attack for obtaining the matrices $\mathbf{A}_{rs}$ numerically for a binary representation of real microstructures is presented in Appendix B.

4.2 Body with prescribed surface tractions and eigenstrains

Recall that the primary variational principal of Hashin and Shtrikman Eq. (4.9), modified to account for presence of initial stresses, can be used to derive the effective stiffness matrix $\widehat{\mathbf{L}}$ and overall eigenstress $\boldsymbol{\lambda}$ of the composite medium. Similarly, employing its dual counterpart one may arrive at the effective compliance matrix $\widehat{\mathbf{M}}$ and overall eigenstrain $\boldsymbol{\mu}$. In such a case the boundary value problem discussed in Section 4.1 is modified according to Fig. 4.2.

In particular, suppose that surface tractions $\overline{\boldsymbol{p}} = \boldsymbol{\Sigma}\cdot\mathbf{n}$ compatible with uniform stress $\boldsymbol{\Sigma}$ are applied along the boundary S of a homogeneous comparison medium (Step I) characterized by the compliance matrix $\mathbf{M}_0$. The corresponding uniform strain $\boldsymbol{E}$ then follows from the constitutive law

$$\boldsymbol{E} = \mathbf{M}_0\boldsymbol{\Sigma} \quad \text{in } \Omega, \quad \boldsymbol{p}_0 = \overline{\boldsymbol{p}} \text{ on } S. \tag{4.33}$$

The local stress $\boldsymbol{\sigma}(\mathbf{x})$ at point $\mathbf{x}$ in Ω of a composite is found by superimposing the solution of the local problem displayed in Fig. 4.2 Step II. The respective governing equations are then given by

$$\begin{aligned}
\boldsymbol{\epsilon}(\mathbf{x}) &= \mathbf{M}(\mathbf{x})\boldsymbol{\sigma}(\mathbf{x}) + \boldsymbol{\mu}(\mathbf{x}) \ \text{ in } \Omega, \quad \boldsymbol{p} = \overline{\boldsymbol{p}} \ \text{ on } S. && (4.34)\\
\boldsymbol{\epsilon}(\mathbf{x}) &= \mathbf{M}_0\boldsymbol{\sigma}(\mathbf{x}) + \boldsymbol{\gamma}(\mathbf{x}) && (4.35)\\
0 &= \epsilon'_{ij,kl} + \epsilon'_{kl,ij} - \epsilon'_{ik,jl} - \epsilon'_{jl,ik} \ \text{ in } \Omega, && (4.36)\\
\mathbf{0} &= \boldsymbol{\gamma} - (\mathbf{M} - \mathbf{M}_0)\boldsymbol{\sigma} - \boldsymbol{\mu} \ \text{ in } \Omega, && (4.37)\\
\boldsymbol{p}' &= \boldsymbol{p} - \boldsymbol{p}_0, \quad \boldsymbol{p}' = \mathbf{0} \ \text{ on } S, && (4.38)
\end{aligned}$$

where $\boldsymbol{\mu}(\mathbf{x})$ is the local eigenstrain and $\boldsymbol{\gamma}(\mathbf{x})$ is called the polarization strain. The compatibility equation (4.36) together with Eq. (4.37) follow from the extended energy functional given by

$$\begin{aligned}
U_{\boldsymbol{\gamma}} = \frac{1}{2}\int_\Omega \Big(&\boldsymbol{\Sigma}^{\mathrm{T}}\boldsymbol{E} - (\boldsymbol{\gamma}-\boldsymbol{\mu})^{\mathrm{T}}(\mathbf{M}-\mathbf{M}_0)^{-1}(\boldsymbol{\gamma}-\boldsymbol{\mu})\\
&-2\boldsymbol{\gamma}^{\mathrm{T}}\boldsymbol{\Sigma} - \boldsymbol{\sigma'}^{\mathrm{T}}\boldsymbol{\gamma}\Big)\,\mathrm{d}\Omega. \qquad (4.39)
\end{aligned}$$

Again, performing a variation with respect to unknown quantities $\boldsymbol{\gamma}$ and $\boldsymbol{\sigma}'$ gives

$$\delta U_{\boldsymbol{\gamma}} = -\frac{1}{2}\int_\Omega \{2\delta\boldsymbol{\gamma}^{\mathrm{T}}[(\mathbf{M}-\mathbf{M}_0)^{-1}(\boldsymbol{\gamma}-\boldsymbol{\mu}) - \boldsymbol{\sigma}] + \delta\boldsymbol{\gamma}^{\mathrm{T}}\boldsymbol{\sigma}' - \delta\boldsymbol{\sigma}'^{\mathrm{T}}\boldsymbol{\gamma}\}\mathrm{d}\Omega. \qquad (4.40)$$

Setting $\delta U_{\boldsymbol{\gamma}} = 0$ we immediately recover Eq. (4.37), while the compatibility condition, Eq. (4.36), follows after recasting the remaining terms in the brackets. As for the primary variational principle, it can be proved that the stationary value $U^S_{\boldsymbol{\gamma}}$ of the potential $U_{\boldsymbol{\gamma}}$ equals the actual potential energy stored in the anisotropic and heterogeneous body

$$U^S_{\boldsymbol{\gamma}} = \frac{1}{2}\int_\Omega (\boldsymbol{\sigma}^{\mathrm{T}}\mathbf{M}\boldsymbol{\sigma} + 2\boldsymbol{\sigma}^{\mathrm{T}}\boldsymbol{\mu})\mathrm{d}\Omega. \qquad (4.41)$$

The function $U_{\boldsymbol{\gamma}}$ attains its maximum ($\delta^2 U_{\boldsymbol{\tau}} < 0$) if $(\mathbf{M}-\mathbf{M}_0)$ is positive definite and its minimum if $(\mathbf{M}-\mathbf{M}_0)$ is negative definite.

To reduce the number of unknown quantities we first write $\boldsymbol{\sigma}'$ in terms of the polarization strain $\boldsymbol{\gamma}$ in the form

$$\boldsymbol{\sigma}'(\mathbf{x}) = \boldsymbol{\sigma}(\mathbf{x}) - \boldsymbol{\Sigma} = [\boldsymbol{\sigma}^*_0\boldsymbol{\gamma}]\,. \qquad (4.42)$$

The operator $[\boldsymbol{\sigma}_0^*\boldsymbol{\gamma}]$ can be identified with the operator $[\boldsymbol{\epsilon}_0^*\boldsymbol{\tau}]$ when replacing $\boldsymbol{\gamma}$ for $\boldsymbol{\tau}$ and $\boldsymbol{\sigma}_0^*$ for $\boldsymbol{\epsilon}_0^*$ in Eq. (A.1) and suitably modifying the boundary term to reflect the traction boundary conditions. As for properties of tensor $\boldsymbol{\sigma}_0^*$ the reader is referred to Appendix C, Eq. (C.22). Again, subscript 0 stands for the homogeneous reference medium.

Next, taking into account Eq. (4.35) we introduce, in analogy with the primary principle, an ensemble average of the local stress $\boldsymbol{\sigma}$ in the form

$$\overline{\boldsymbol{\sigma}(\mathbf{x})} = \boldsymbol{\Sigma} + \int_\Omega \boldsymbol{\sigma}_0^*(\mathbf{x}-\mathbf{x}')\overline{\boldsymbol{\gamma}(\mathbf{x}')}\,\mathrm{d}\Omega(\mathbf{x}') - \mathbf{M}_0^{-1}\overline{\boldsymbol{\gamma}(\mathbf{x})}, \tag{4.43}$$

to rewrite Eq. (4.39) as

$$\begin{aligned} U_{\boldsymbol{\gamma}} &= \frac{1}{2}\int_\Omega \Big(\boldsymbol{\Sigma}^{\mathrm{T}}\boldsymbol{E} - (\boldsymbol{\gamma}(\mathbf{x})-\boldsymbol{\mu}(\mathbf{x}))^{\mathrm{T}}(\mathbf{M}(\mathbf{x})-\mathbf{M}_0)^{-1}(\boldsymbol{\gamma}(\mathbf{x})-\boldsymbol{\mu}(\mathbf{x})) - 2\boldsymbol{\gamma}^{\mathrm{T}}(\mathbf{x})\overline{\boldsymbol{\sigma}(\mathbf{x})} \\ &- \boldsymbol{\gamma}^{\mathrm{T}}(\mathbf{x})\int_\Omega \boldsymbol{\sigma}_0^*(\mathbf{x}-\mathbf{x}')\left(\boldsymbol{\gamma}(\mathbf{x}') - 2\overline{\boldsymbol{\gamma}(\mathbf{x}')}\right)\mathrm{d}\mathbf{x}' \\ &+ \boldsymbol{\gamma}^{\mathrm{T}}(\mathbf{x})\mathbf{M}_0^{-1}\left(\boldsymbol{\gamma}(\mathbf{x}) - 2\overline{\boldsymbol{\gamma}(\mathbf{x})}\right)\Big)\,\mathrm{d}\Omega(\mathbf{x}) \end{aligned} \tag{4.44}$$

Assuming that each phase r of a randomly arranged composite is homogeneous with the compliance matrix $\mathbf{M}_r, r = 1,\ldots,n$, we write in analogy with the Section 4.1 the material stiffness matrix, the polarization strain $\boldsymbol{\gamma}$ and eigenstrain $\boldsymbol{\mu}$ in the sample α as

$$\begin{aligned} \mathbf{M}(\mathbf{x},\alpha) &= \sum_{r=1}^n \mathbf{M}_r\chi_r(\mathbf{x},\alpha), \\ \boldsymbol{\gamma}(\mathbf{x},\alpha) &= \sum_{r=1}^n \boldsymbol{\gamma}_r(\mathbf{x})\chi_r(\mathbf{x},\alpha), \qquad \boldsymbol{\mu}(\mathbf{x},\alpha) = \sum_{r=1}^n \boldsymbol{\mu}_r(\mathbf{x})\chi_r(\mathbf{x},\alpha), \end{aligned} \tag{4.45}$$

with the respective ensemble averages given

$$\overline{\mathbf{M}(\mathbf{x})} = \sum_{r=1}^n \mathbf{M}_r S_r(\mathbf{x}), \quad \overline{\boldsymbol{\gamma}(\mathbf{x})} = \sum_{r=1}^n \boldsymbol{\gamma}_r(\mathbf{x})S_r(\mathbf{x}), \quad \overline{\boldsymbol{\mu}(\mathbf{x})} = \sum_{r=1}^n \boldsymbol{\mu}_r(\mathbf{x})S_r(\mathbf{x}). \tag{4.46}$$

Suppose the material is again ergodic and statistically homogeneous. Then individual terms in Eq. (4.46) simplify such that

$$\overline{\mathbf{M}} = \sum_{r=1}^n \mathbf{M}_r c_r, \ \overline{\boldsymbol{\gamma}(\mathbf{x})} = \sum_{r=1}^n \boldsymbol{\gamma}_r(\mathbf{x})c_r, \ \overline{\boldsymbol{\mu}(\mathbf{x})} = \sum_{r=1}^n \boldsymbol{\mu}_r(\mathbf{x})c_r. \tag{4.47}$$

Substituting Eqs. (4.47) into Eq. (4.44) readily provides the extended averaged form of the dual Hashin-Shtrikman principle

$$
\begin{aligned}
\overline{U}\boldsymbol{\gamma} \;=\; & \frac{1}{2}\int_\Omega \boldsymbol{\Sigma}^{\mathrm{T}}\boldsymbol{E}\,\mathrm{d}\Omega(\mathbf{x}) - \\
& \frac{1}{2}\sum_r \int_\Omega \left(c_r(\boldsymbol{\gamma}_r(\mathbf{x})-\boldsymbol{\mu}_r(\mathbf{x}))^{\mathrm{T}}(\mathbf{M}_r-\mathbf{M}_0)^{-1}(\boldsymbol{\gamma}_r(\mathbf{x})-\boldsymbol{\mu}_r(\mathbf{x})) - 2c_r{\boldsymbol{\gamma}_r}^{\mathrm{T}}(\mathbf{x})\overline{\boldsymbol{\sigma}(\mathbf{x})}\right)\mathrm{d}\Omega(\mathbf{x}) \\
- \; & \frac{1}{2}\sum_r\sum_s \int_\Omega \boldsymbol{\gamma}_r(\mathbf{x})^{\mathrm{T}} \int_\Omega \boldsymbol{\sigma}_0^*(\mathbf{x}-\mathbf{x}')\left[S_{rs}(\mathbf{x}-\mathbf{x}')\boldsymbol{\gamma}_s(\mathbf{x}') - 2c_s\overline{\boldsymbol{\gamma}(\mathbf{x}')}\right]\mathrm{d}\Omega(\mathbf{x}')\mathrm{d}\Omega(\mathbf{x}) \\
+ \; & \frac{1}{2}\sum_r\sum_s \int_\Omega \mathbf{M}_0^{-1}\left(\delta_{rs}c_rc_s\boldsymbol{\gamma}_s(\mathbf{x}) - 2c_s\overline{\boldsymbol{\gamma}_s(\mathbf{x})}\right)\mathrm{d}\Omega(\mathbf{x}).
\end{aligned}
\tag{4.48}
$$

Performing a variation with respect to $\boldsymbol{\gamma}_r(\mathbf{x})$ and using Eq. $(4.46)_2$ provides the extended form of the stationarity conditions

$$
\begin{aligned}
& (\mathbf{M}_r-\mathbf{M}_0)^{-1}\boldsymbol{\gamma}_r(\mathbf{x})c_r - \sum_{s=1}^{n}\left(\int_\Omega \boldsymbol{\sigma}_0^*(\mathbf{x}-\mathbf{x}')\left[S_{rs}(\mathbf{x}-\mathbf{x}') - c_rc_s\right]\boldsymbol{\gamma}_s(\mathbf{x}')\,\mathrm{d}\Omega(\mathbf{x}')\right. \\
- \; & \left.\mathbf{M}_0^{-1}(\delta_{rs}c_rc_s - c_sc_r)\right) = \overline{\boldsymbol{\sigma}(\mathbf{x})}c_r + (\mathbf{M}_r-\mathbf{M}_0)^{-1}\boldsymbol{\mu}_r(\mathbf{x})c_r.
\end{aligned}
\tag{4.49}
$$

To derive the macroscopic constitutive equation we follow the procedure outlined in the previous section. To that end, we first write the Fourier transform of polarization strain $\widetilde{\boldsymbol{\gamma}_r}(\boldsymbol{\xi})$ in the form

$$
\widetilde{\boldsymbol{\gamma}_r}(\boldsymbol{\xi}) = \sum_{s=1}^{2}\widetilde{\mathbf{R}}_{rs}(\boldsymbol{\xi})c_s\left[\overline{\widetilde{\boldsymbol{\sigma}}(\boldsymbol{\xi})} + (\mathbf{M}_s-\mathbf{M}_0)^{-1}\widetilde{\boldsymbol{\mu}_s}(\boldsymbol{\xi})\right],
\tag{4.50}
$$

where tensors $\widetilde{\mathbf{R}}_{rs}$ must be again obtained for the specific microstructure. Thus the Fourier transform of Eq. $(4.46)_2$ is given by

$$
\overline{\widetilde{\boldsymbol{\gamma}}(\boldsymbol{\xi})} = \sum_{r=1}^{2}\sum_{s=1}^{2} c_r\widetilde{\mathbf{R}}_{rs}(\boldsymbol{\xi})c_s\left[\overline{\widetilde{\boldsymbol{\sigma}}(\boldsymbol{\xi})} + (\mathbf{M}_s-\mathbf{M}_0)^{-1}\widetilde{\boldsymbol{\mu}_s}(\boldsymbol{\xi})\right],
\tag{4.51}
$$

and finally, the inverse Fourier transform of Eq. (4.51) gives

$$
\overline{\boldsymbol{\gamma}(\mathbf{x})} = \sum_{r=1}^{2}\sum_{s=1}^{2}\int_\Omega c_r\mathbf{R}_{rs}(\mathbf{x}-\mathbf{x}')c_s\left[\overline{\boldsymbol{\sigma}(\mathbf{x}')} + (\mathbf{M}_s-\mathbf{M}_0)^{-1}\boldsymbol{\mu}_s(\mathbf{x}')\right]\mathrm{d}\mathbf{x}'.
\tag{4.52}
$$

In analogy with Section 4.1 we limit our attention to constant ensemble average $\overline{\boldsymbol{\sigma}}$ and piecewise uniform distribution of eigenstrain $\boldsymbol{\mu}_e$ to get

$$
\int_\Omega \mathbf{R}_{rs}(\mathbf{x}-\mathbf{x}')\mathrm{d}\Omega(\mathbf{x}') = \int_\Omega \mathbf{R}_{rs}(\mathbf{x})\mathrm{d}\Omega(\mathbf{x}) = \widetilde{\mathbf{R}}_{rs}(\boldsymbol{\xi}=\mathbf{0}).
\tag{4.53}
$$

Ensemble average of Eq. (4.35) then leads to the desired macroscopic constitutive law

$$\overline{\boldsymbol{\epsilon}} = \widehat{\mathbf{M}}\overline{\boldsymbol{\sigma}} + \overline{\boldsymbol{\mu}}, \tag{4.54}$$

with

$$\widehat{\mathbf{M}} = \mathbf{M}_0 + \sum_{r=1}^{2}\sum_{s=1}^{2} c_r \widetilde{\mathbf{R}}_{rs}(\boldsymbol{\xi}=\mathbf{0}) c_s, \tag{4.55}$$

$$\overline{\boldsymbol{\mu}} = \sum_{r=1}^{2}\sum_{s=1}^{2} c_r \widetilde{\mathbf{R}}_{rs}(\boldsymbol{\xi}=\mathbf{0}) c_s (\mathbf{M}_s - \mathbf{M}_0)^{-1}\boldsymbol{\mu}_{\boldsymbol{s}}. \tag{4.56}$$

For a general n-phase composite medium the system (4.49) assumes the following form

$$(\mathbf{M}_r - \mathbf{M}_0)^{-1}\boldsymbol{\gamma}_r c_r - \sum_{s=1}^{n} \mathbf{B}_{rs}\boldsymbol{\gamma}_s = c_r\overline{\boldsymbol{\sigma}} + (\mathbf{M}_r - \mathbf{M}_0)^{-1} c_r \boldsymbol{\mu}_r, \quad r = 1, 2, \ldots, n, \tag{4.57}$$

where microstructure-dependent matrices $\mathbf{B}_{rs}$ are provided by

$$\mathbf{B}_{rs} = \int_{\Omega} \boldsymbol{\sigma}_0^*(\mathbf{x}-\mathbf{x}') \left[S_{rs}(\mathbf{x}-\mathbf{x}') - c_r c_s\right] \mathrm{d}\Omega(\mathbf{x}'). \tag{4.58}$$

In analogy with Eqs. (4.32), the solution of system (4.57) is found in the form

$$\boldsymbol{\gamma}_r = \sum_{s=1}^{n} \mathbf{R}_{rs} c_s \left[\overline{\boldsymbol{\sigma}} + (\mathbf{M}_s - \mathbf{M}_0)^{-1}\boldsymbol{\mu}_s\right], \tag{4.59}$$

so that

$$\overline{\boldsymbol{\gamma}} = \sum_{r=1}^{n}\sum_{s=1}^{n} c_r \mathbf{R}_{rs} c_s \left[\overline{\boldsymbol{\sigma}} + (\mathbf{M}_s - \mathbf{M}_0)^{-1}\boldsymbol{\mu}_s\right]. \tag{4.60}$$

Evaluation of microstructure-dependent tensors $\mathbf{B}_{rs}$ is outlined in Appendix B.

4.3 Numerical example

To make comparisons with the finite element approach we consider afresh the graphite fiber tow of Fig. 2.3. The primary goal is to recover the effective thermo-elastic properties already derived in Chapter 3.

Starting from the primary H-S variational principle, Section 4.1, the thermo-elastic macroscopic constitutive law receives the form

$$\overline{\boldsymbol{\sigma}} = \widehat{\mathbf{L}}\left(\overline{\boldsymbol{\epsilon}} - \overline{\boldsymbol{m}}\Delta\theta\right), \tag{4.61}$$

where $\overline{\boldsymbol{m}}$ is the overall thermal strain vector of the expansion coefficients. To fill individual entries in $\widehat{\mathbf{L}}$ and $\overline{\boldsymbol{m}}$ requires first to solve Eq. (4.28) for unknown components of vectors $\boldsymbol{\tau}_r$. To comply with the generalized plane strain conditions it is necessary to augment the 3×3 matrix $\mathbf{A}_{rs}$ into 4×4 matrix by zeros into the fourth column and row.

Eqs. (4.2) and (4.3) then readily provide the ensemble average $\overline{\boldsymbol{\sigma}}$ as

$$\overline{\boldsymbol{\sigma}} = \sum_{r=1}^{2} c_r \left\{ \mathbf{L}_r \left(\mathbf{L}_r - \mathbf{L}_0 \right)^{-1} \boldsymbol{\tau}_r + \mathbf{L}_r \left[\left(\mathbf{L}_r - \mathbf{L}_0 \right)^{-1} - \mathbf{I} \right] \boldsymbol{m}_r \Delta\theta \right\}. \tag{4.62}$$

Referring to Section 3.2.2 the coefficients of the stiffness matrix $\widehat{\mathbf{L}}$ are found from solutions of four successive elasticity problems. In each solution the medium, free of thermal strains, is subjected to overall strain $\overline{\boldsymbol{\epsilon}}$ with only one nonzero component of unit magnitude. The overall stress, resulting from Eq. (4.62), then furnishes the column of the (4×4) matrix $\widehat{\mathbf{L}}$ corresponding to the selected nonzero component of $\overline{\boldsymbol{\epsilon}}$ as a function of $\mathbf{L}_0$. Therefore, having properly chosen components of the stiffness matrix of the comparison medium $\mathbf{L}_0$ we may arrive either at the lower or upper bound on elastic stiffnesses of heterogeneous media. In particular, we select $\mathbf{L}_0$ as an artificial material with coefficients $L^0_{ij} \begin{matrix} < \\ > \end{matrix} L^r_{ij}$ smallest (largest) of all L^r_{ij} in Ω.

Results appear in Table 4.1. Material properties of individual phases are taken from Table 3.10. The FFT combined with the Gaussian quadrature is used to evaluate the microstructure dependent matrices $\mathbf{A}_{rs}$ (recall Section 2.3.1 and Appendix B).

The thermal strain coefficients are obtained in the similar way by setting $\overline{\boldsymbol{\epsilon}} = \mathbf{0}$ and applying the temperature change $\Delta\theta$ equal to unity. The stress from Eq. (4.62) is the overall eigenstress $\overline{\boldsymbol{\lambda}}$. The overall thermal strain $\overline{\boldsymbol{m}}$ then follows from

$$\overline{\boldsymbol{m}} = -\widehat{\mathbf{M}}\overline{\boldsymbol{\lambda}}, \tag{4.63}$$

where $\widehat{\mathbf{M}} = \widehat{\mathbf{L}}^{-1}$. Results are summarized in Table 4.2.

Clearly the finite element solutions from Chapter 3, except for the lowest resolution of the digitized medium which essentially overestimates the fiber volume fraction, falls within

Table 4.1: Effective elastic stiffnesses [GPa]

Bitmap	L_{11}			L_{22}			L_{33}		
resolution	LB	FEM	UB	LB	FEM	UB	LB	FEM	UB
122 × 84	10.733	10.762	10.770	10.713	10.725	10.746	2.211	2.215	2.218
244 × 179	10.740	10.762	10.777	10.720	10.725	10.752	2.209	2.215	2.216
488 × 358	10.730	10.762	10.763	10.721	10.725	10.754	2.209	2.215	2.216
976 × 716	10.730	10.762	10.763	10.721	10.725	10.764	2.209	2.215	2.216

Table 4.2: Effective coefficients of thermal expansion [K^{-1}]

Bitmap	$\alpha_x \times 10^5$			$\alpha_y \times 10^5$			$\alpha_z \times 10^7$			c_f
resolution	LB	FEM	UB	LB	FEM	UB	LB	FEM	UB	
122 × 84	2.248	2.269	2.278	2.230	2.248	2.253	-7.488	-7.463	-7.504	0.438
244 × 179	2.256	2.269	2.285	2.236	2.248	2.259	-7.455	-7.463	-7.471	0.436
488 × 358	2.256	2.269	2.287	2.237	2.248	2.260	-7.455	-7.463	-7.471	0.436
976 × 716	2.256	2.269	2.287	2.237	2.248	2.260	-7.455	-7.463	-7.471	0.436

individual bounds. Tables 4.1 and 4.2 further demonstrate insensivity of the solution to the selected bitmap resolution, as long as the volume fraction of the inclusion is the same (see Section 2.4.3). In addition, attributed to the assumed statistical homogeneity the results confirm a slight anisotropy of the present medium suggested by the results from the previous chapter. Efficiency of the present approach when compared to the FEM analysis is doubtless. Nevertheless, to fully accept this method a number of other numerical experiments, particularly when loading the material beyond the elastic limit, are needed.

Chapter 5

CONCLUSIONS

Effective thermoelastic and viscoelastic properties are found for a fibrous graphite-epoxy composite system with fibers randomly distributed within a transverse plane section of the composite aggregate. Two reliable and efficient approaches are introduced in the present work. Although different at their theoretical formulation both approaches are closely tight to the same statistical descriptors generally used to quantify random microstructures.

The first approach follows well established procedures which incorporate various periodic unit cell models combined with the finite element method. The complexity of real microstructures is reflected here in more complicated unit cells having larger number of particles. The required number particles and their arrangement is determined such that the macroscopic response of a unit cell is identical to the behavior of a real composite. A simple and intuitive approach based on microstructural statistics is proposed to derive such periodic unit cells. The stepping stone in the present approach is the knowledge of either the two-point probability function or the second order intensity function. Details regarding these functions are given in Chapter 2 together with methods for their determination. In addition, this chapter describes a series of tests confirming the validity of statistical isotropy and ergodicity assumptions suggested for the present composite system (graphite fiber tow impregnated by the polymer matrix). Chapter 3 then outlines generation of optimal unit cells by matching the material statistics of both the unit cell and real material up to two-point level. An optimization problem arising in informulation is then solved with the help of genetic algorithms. The present work promotes the Augmented Simulated Annealing method as the most suitable one in achieving this goal. Finally, an applicability of the present approach is confirmed by evaluating effective thermoelastic properties of the selected composite system

from both the small period unit cells (five to ten fibers unit cells) and considerably larger unit cells having of two orders of magnitude more particles (three to five hundred fibers). An excellent match is found. These results are rather encouraging particularly when applying the small unit cells to study an inelastic response of random composites. This approach is under current investigation.

An alternative procedure discussed in Chapter 4 is closely related to well known effective medium theories. Here, the most widely used variational principles of Hashin and Shtrikman are reviewed. Both the displacement and traction based formulations are revisited in conjunction with random composites and extended to account for the presents of initial stresses or strains. A very efficient numerical procedure based on the DFT which directly exploits digitized images of real microstructures is implemented. Fourier transform approach applied when solving the resulting integral equations is rather advantageous as it allows an arbitrary choice of the reference medium so that often encountered anisotropy of individual phases creates no obstacles in the solution procedure. When compared to unit cell approach this method is more efficient and thus preferable when evaluating the macroscopic elastic response of real composites. Not the same might be true when inelastic deformations are decisive. But this has yet to be confirmed.

BIBLIOGRAPHY

[Axelsen, 1995] Axelsen, M. (1995). *Quantitative description of the morphology and microdamage of composite materials*. PhD thesis, Aalborg University. Also available as `http://cwis.auc.dk/phd/fulltext/axelsen/pdf/axelsen.pdf`.

[Baker, 1987] Baker, J. E. (1987). Reducing bias and inefficiency in the selection algorithm. In Grefenstette, J., editor, *Proceedings of the First International Conference on Genetic Algorithms*, pages 101–111. Lawrence Erlbaum Associates.

[Bazant and Wu, 1973] Bazant, P. and Wu, S. (1973). Dirichlet series creep function for aging concrete. *J. of the Engineering Mechanics Division*, 99(EM2):367–387.

[Beasley et al., 1993] Beasley, D., Bull, D., and Martin, R. (1993). An overview of Genetic Algorithms: Part 1, Foundations. *University Computing*, 15(2):58–69. Also available as `ftp://ralph.cs.cf.ac.uk/pub/papers/GAs/ga_overview1.ps`.

[Benveniste, 1987] Benveniste, Y. (1987). A new approach to the application of Mori-Tanaka theory in composite materials. *Mechanics of Materials*, 6:147–157.

[Beran, 1968] Beran, M. J. (1968). *Statistical Continuum Theories*. Monographs in Statistical Physics. Interscience Publishers.

[Bittnar and Šejnoha, 1996] Bittnar, Z. and Šejnoha, J. (1996). *Numerical methods in structural engineering*. ASCE Press.

[Boublík, 1996] Boublík, T. (1996). *Statistická termodynamika*. Academia.

[Burden and Faires, 1989] Burden, R. and Faires, J. D. (1989). *Numerical Analysis*. PWS-Kent Publishing Company, 4th edition.

[Burrus and Parks, 1985] Burrus, C. and Parks, T. W. (1985). *DFT/FFT and convolution algorithms: Theory and implementation*. Topics in Digital Signal Processing. A Wiley-Interscience Publication.

[Chaboche, 1997] Chaboche, J. (1997). Thermodynamic formulation of constitutive equations and application to the viscoplasticity and viscoelasticity of metals and polymers. *Int. J. Solids and Structures*, 34:2239–2254.

[Davis, 1989] Davis, L. (1989). Adapting operator probabilities in genetic algorithm. In Schaffer, J. D., editor, *Proceeding of the Third International Conference on Genetic Algorithms*, pages 61–69. Morgan Kaufmann.

[Drugan and Willis, 1996] Drugan, W. and Willis, J. (1996). A micromechanics-based nonlocal constitutive equation and estimates of representative volume element size for elastic composites. *Journal of the Mechanics and Physics of Solids*, 44(4):497–524.

[Dvorak and Benveniste, 1992a] Dvorak, G. and Benveniste, Y. (1992a). On transformation strains and uniform fields in multiphase elastic media. *Proc. R. Soc. Lond., A*, 437:291–310.

[Dvorak and Benveniste, 1992b] Dvorak, G. and Benveniste, Y. (1992b). Transformation field analysis of inelastic materials. *Proc. R. Soc. Lond., A*, 437:311–326.

[Fára, 1990] Fára, F. (1990). *Komplexní hodnocení objemových změn kompozitních soustav*. PhD thesis, Czech Technical University in Prague, Faculty of Civil Engineerin, Prague, Czech Republic.

[Fish et al., 1997] Fish, J., Shek, K., Pandheeradi, M., and Shephard, M. (1997). Computational plasticity for composite structures based on mathenatical homogenization: Theory and practice. *Computer Methods in Applied Mechanics and Enginerring*, 148:53–73.

[Goldberg, 1989] Goldberg, D. (1989). *Genetic Algorithms in Search, Optimization and Machine Learning*. Addison-Wesley.

[Hashin and Shtrikman, 1963] Hashin, Z. and Shtrikman, S. (1963). A variational approach to the theory of elastic behavior of multiphase materials. *Journal of the Mechanics and Physics of Solids*, 11:127–140.

[Hill, 1963] Hill, R. (1963). Elastic properties of reinforced solids - Some theoretical principles. *Journal of the Mechanics and Physics of Solids*, 11:357–372.

[Hill, 1964] Hill, R. (1964). Theory of mechanical properties of fibre-strenghtened materials: I. Elastic behaviour. *Journal of the Mechanics and Physics of Solids*, 12:199–212.

[Hill, 1965] Hill, R. (1965). A self-consistent mechanics of composite materials. *Journal of the Mechanics and Physics of Solids*, 13:213–222.

[Houck et al., 1995] Houck, C. R., Joines, J. A., and Kay, M. G. (1995). A Genetic Algorithm for function OpTimization: A Matlab implementation. Technical Report NCSU-IE TR 95-09, North Carolina State University. Also available as `http://www.fmmcenter.ncsu.edu/fac_staff/joines/papers/gaot.ps`.

[Hudec, 1999] Hudec, B. (1999). *Programovací techniky*. ČVUT.

[Kohler and Papanicalou, 1982] Kohler, W. and Papanicalou, G. C. (1982). Bound for the overall conductivity of random media. In Burridge, R., Childress, S., and Papanicolaou, G., editors, *Macroscopic properties of disordered media*, volume 24 of *Lecture Notes in Physics*, pages 111–130. Courant Institute, Springer-Verlag, Berlin.

[Kvasnička, 1993] Kvasnička, V. (1993). Stochastické metody optimalizace funcií N premenných. In *Analýza dat*, Pardubice.

[Kvasnička, 1994] Kvasnička, V. (1994). Augmented simulated annealing adaption of feedforward neural networks. *Neural Network Worl*, 3:67–80.

[Lepš and Šejnoha, 2000] Lepš, M. and Šejnoha, M. (2000). New approach to optimization of reinforced concrete beams. In Bittnar, Z. and Topping, B., editors, *Computational concrete structures technology*, pages 143–151. Civil-Comp Press.

[Mahfoud and Goldberg, 1992] Mahfoud, S. and Goldberg, D. E. (1992). A genetic algorithm for parallel simulated annealing. In Manner, R. and Manderick, B., editors, *Parallel Problem from Nature*, volume 2, pages 301–310. North-Holland, Amsterdam.

[Markov, 1998] Markov, K. Z. (1998). On the cluster bounds for the effective properties of microcraked solids. *Journal of the Mechanics and Physics of Solids*, 46(2):357–388.

[Matouš et al., 2000] Matouš, K., Lepš, M., Zeman, J., and Šejnoha, M. (2000). Applying genetic algorithms to selected topics commonly encountered in engineering practice. *Computer Methods in Applied Mechanics and Engineering*, 190(13–14):1629–1650.

[Michalewicz, 1992] Michalewicz, Z. (1992). *Genetic Algorithms + Data Structures = Evolution Programs*. AI Series. Springer-Verlag, New York.

[Michalewicz et al., 1994] Michalewicz, Z., Logan, T. D., and Swaminathan, S. (1994). Evolutionary operators for continuous convex parameter spaces. In Sebald, A. and Fogel, L., editors, *Proceedings of the 3rd Annual Conference on Evolutionary Programming*, pages 84–97, River Edge, NJ. World Scientific Publishing. Also available as `ftp://ftp.uncc.edu/coe/evol/p1.ps`.

[Michel et al., 1999] Michel, J., Moulinec, H., and Suquet, P. (1999). Effective properties of composite materials with periodic microstructure: A computational approach. *Computer Methods in Applied Mechanics and Engineering*, 172:109–143.

[Mori and Tanaka, 1973] Mori, T. and Tanaka, K. (1973). Average stress in matrix and average elastic energy of elastic materials with misfitting inclusions. *Acta Metallurgica*, 21:571.

[Ponte Casteñada and Willis, 1995] Ponte Casteñada, P. and Willis, J. (1995). The effect of spatial distribution on the effective behavior of composite materials and cracked media. *Journal of the Mechanics and Physics of Solids*, 43(12):1919–1951.

[Povirk, 1995] Povirk, G. L. (1995). Incorporation of microstructural information into models of two-phase materials. *Acta metall. mater.*, 43(8):3199–3206.

[Press et al., 1992] Press, W. H., Teukolsky, S. A., Vetterling, W. T., and Flannergy, B. P. (1992). *Numerical recipes in C*. Cambridge University Press, 2nd edition. Also available as `http://www.nr.com`.

[Pyrz, 1994] Pyrz, R. (1994). Correlation of microstructure variability and local stress field in two-phase materials. *Materials Science and Engineering*, A177:253–259.

[Quintanilla and Torquato, 1997] Quintanilla, J. and Torquato, S. (1997). Microstructure functions for a model of statistically inhomogeneous random media. *Physical Review E*, 55(2):1558–1565.
Also available as `http://www.cherypit.princeton.edu/papers/paper-131.pdf`.

[Rektorys, 1995a] Rektorys, K., editor (1995a). *Přehled užité matematiky*, volume 2. Prometheus, 6th edition.

[Rektorys, 1995b] Rektorys, K., editor (1995b). *Přehled užité matematiky*, volume 1. Prometheus, 6th edition.

[Ripley, 1977] Ripley, B. (1977). Modeling of spatial patterns. *Journal of the Royal Statistical Society - Series B (methodological)*, 39(2):172–192.

[Schapery, 1981] Schapery, R. (1981). On viscoelastic deformation and failure behavior of composite materials with distributed flaws. In Wang, S. and Renton, W., editors, *Advances in Aerospace Structures and Materials*, pages 5–20. ASME, New York.

[Sejnoha, 1999] Sejnoha, M. (1999). *Micromechanical analysis of unidirectional fibrous composite plies and laminates*, volume 3 of *CTU Reports*. Czech Technical University in Prague.

[Smith and Torquato, 1988] Smith, P. and Torquato, S. (1988). Computer simulation results for the two-point probability function of composite media. *Journal of Computational Physics*, 76:176–191.

[Sokolnikoff and Redheffer, 1958] Sokolnikoff, I. S. and Redheffer, R. M. (1958). *Mathematics of physics and modern engeneering*. McGRAW W-HILL BOOK COMPANY, INC.

[Srinivas, 1997] Srinivas, M. (1997). *Micromechanical Modeling of Composite Plies and Laminates*. PhD thesis, Rensselaer Polytechnic Institute, Troy, New York.

[Suquet, 1987] Suquet, P. (1987). Elements of homogenization for inelastic solid mechanics. In Sanchez-Palencia, E. and Zaoui, A., editors, *Homogenization Techniques for Composite Media*, volume 272 of *Lecture notes in physics*, pages 194–278. Springer-Verlag, Berlin.

[Teplý and Dvořák, 1988] Teplý, J. L. and Dvořák, G. J. (1988). Bound on overall instantaneous properties of elastic-plastic composites. *Journal of the Mechanics and Physics of Solids*, 36(1):29–58.

[Torquato, 1991] Torquato, S. (1991). Random heterogeneous media: Microstructure and improved bound on effective properties. *Applied Mechanics Review*, 44(2):37–76.

[Torquato, 1998] Torquato, S. (1998). Morphology and effective properties of disordered media. *International journal of solids and structures*, 35(19):2385–2406.

[Torquato and Stell, 1982] Torquato, S. and Stell, G. (1982). Microstructure of two-phase random media. I. The n-point probability functions. *Journal of Chemical Physics*, 77(4):2071–2077.

[Torquato and Stell, 1985] Torquato, S. and Stell, G. (1985). Microstructure of two-phase random media. V. The n-point matrix probability functions for impenetrable spheres. *Journal of Chemical Physics*, 82(2):980–987.

[Šejnoha et al., 1999] Šejnoha, M., Horečka, L., and Matouš, K. (1999). Modeling of masonry structures strengthened by pre-tensioned glas-fiber-reinforced polymer laminates. In G.M. Carlomagno, C. B., editor, *Computational methods and experimental measurements IX*, pages 381–390. WITpress.

[Wafa, 1994] Wafa, A. M. (1994). *Application of the Transformation Field Analysis to Inelastic Composite Materials and structures*. PhD thesis, Rensselaer Polytechnic Institute, Troy, New York.

[Willis, 1977] Willis, J. R. (1977). Bounds and self-consistent estimates for the overall properties of anisotropic composites. *Journal of the Mechanics and Physics of Solids*, 25:185–202.

[Yeong and Torquato, 1998] Yeong, C. L. Y. and Torquato, S. (1998). Reconstructing random media. *Physical Review E*, 57(1):495–506.

[Yuret, 1994] Yuret, D. (1994). From genetic algorithms to efficient optimization. Technical Report 1569, Massachusetts Institute of Technology, Artificial Intelligence Laboratory. Also available as `http://www.ai.mit.edu/people/deniz/publications/aitr1569.ps.gz`.

[Zeman, 2000] Zeman, J. (2000). Random composites. Master's thesis, Czech Technical University in Prague.

[Zeman and Šejnoha, 2001] Zeman, J. and Šejnoha, M. (2001). Effective properties of graphite fiber tow impregnated by polymer matrix. *JMPS*, 49:69–90.

Appendix A

PROPERTIES OF THE OPERATOR $[\epsilon_0^* \tau]$

Derivation of the operator $[\boldsymbol{\epsilon}_0^* \boldsymbol{\tau}]$ calls for the solution of the boundary value problem displayed in Fig. A.1(a). Suppose that a three-dimensional homogeneous and isotropic body Ω with the boundary S is loaded by polarization stress $\boldsymbol{\tau}(\mathbf{x}), \mathbf{x} \in \Omega$, and surface displacements $\boldsymbol{u}'(\mathbf{x}), \mathbf{x} \in S$. The constitutive law together with assumed boundary conditions are shown in Fig. A.1(a).

Before proceeding with the solution of the present problem it is convenient to introduce an auxiliary problem described in Fig. A.1(b). In particular, consider an unbounded domain Ω^∞ with boundary S^∞. It is assumed that this new region is in an equilibrium state under application of a certain body force $\mathbf{b}^*$ discussed below.

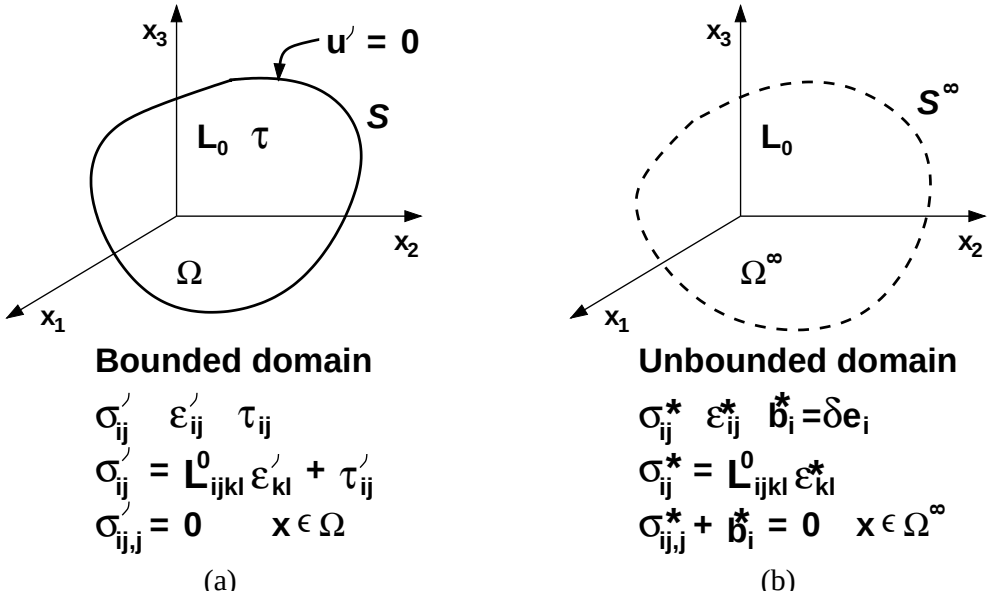

Figure A.1: Boundary value problem to derive the operator $[\boldsymbol{\epsilon}_0^* \boldsymbol{\tau}]$

If elastic properties remain the same in both cases, the solution of the original problem can now be inferred from application of Betti's theorem

$$\int_\Omega (\sigma'_{ij} - \tau_{ij})\epsilon^*_{ij}\ \mathrm{d}\Omega = \int_\Omega \epsilon'_{ij}\sigma^*_{ij}\ \mathrm{d}\Omega. \tag{A.1}$$

Integrating by parts both sides of Eq. (A.1) yields

$$-\int_\Omega \sigma'_{ij,j}u^*_i\ \mathrm{d}\Omega + \int_S \sigma'_{ij}n_j u^*_i\ \mathrm{d}S - \int_\Omega \tau_{ij}\epsilon^*_{ij}\ \mathrm{d}\Omega = -\int_\Omega \sigma^*_{ij,j}u'_i\ \mathrm{d}\Omega + \int_S \sigma^*_{ij}n_j u'_i\ \mathrm{d}S. \tag{A.2}$$

Note that $f_{,i} = \frac{\partial f}{\partial x_i}$. The first term on the left-hand side and the last term on the right-hand side disappear due to equilibrium and boundary conditions, see Fig. A.1(a). In addition, the equilibrium condition for unbounded domain, Fig. A.1(b), can be used in Eq. (A.2) to get

$$\int_S L^0_{ijkl}\epsilon'_{kl}n_j u^*_i\ \mathrm{d}S + \int_\Omega \tau_{ij,j}u^*_i\ \mathrm{d}\Omega = \int_\Omega b^*_i u'_i\ \mathrm{d}\Omega. \tag{A.3}$$

Notice that the divergence theorem was applied to the last term on the left-hand side to eliminate the polarization stress $\boldsymbol{\tau}$ from the boundary integral. It now becomes advantageous to modify Eq. (A.3) by subtracting a "zero" term

$$\int_\Omega \overline{\tau}_{ij,j}u^*_i\ \mathrm{d}\Omega,$$

from the last term on the left hand side, where $\overline{\boldsymbol{\tau}}$ is a constant polarization stress tensor. It is worthwhile to mention that this transformation is valid also in the case when $\overline{\boldsymbol{\tau}} = \overline{\boldsymbol{\tau}}(\mathbf{x})$ does vary, but $\overline{\tau}_{ij,j} \ll \tau_{ij,j}$. After integrating by parts the modified term we finally get

$$\int_\Omega b^*_i u'_i\ \mathrm{d}\Omega = \int_S \left(L^0_{ijkl}\epsilon'_{kl} + \tau_{ij} - \overline{\tau}_{ij}\right) n_j u^*_i\ \mathrm{d}S - \int_\Omega (\tau_{ij} - \overline{\tau}_{ij})\epsilon^*_{ij}\mathrm{d}\Omega. \tag{A.4}$$

If $\overline{\tau}_{ij}$ is taken as the mean value of $\tau_{ij}(\mathbf{x})$, then integrals involving $\tau_{ij}(\mathbf{x}) - \overline{\tau}_{ij}$ oscillate about zero and similarly in virtue of St. Venant's principle will do the term $L^0_{ijkl}\epsilon'_{kl}$. Hence the integral over S is insignificant except for points $\mathbf{x}'$ in a "boundary layer" close to S [Willis, 1977].

Eq. (A.4) can be further modified when associating individual components of the body force $\mathbf{b}^*$ with positive unit point loads applied at a point $\mathbf{x}' \in \Omega^\infty$ in the directions of the

coordinate axes x_1, x_2, x_3. To this end, denote

$$b_i^* = \delta_{pi}\delta(\mathbf{x}-\mathbf{x}')e_p, \tag{A.5}$$

where δ is the Dirac delta function, which has a zero value at all points $\mathbf{x} \neq \mathbf{x}'$ except for the point $\mathbf{x} = \mathbf{x}'$ where it tends to infinity. Recall the following property of the Dirac function

$$\int_\Omega u'_p(\mathbf{x})\delta(\mathbf{x}-\mathbf{x}')\,\mathrm{d}\Omega(\mathbf{x}) \;=\; u'_p(\mathbf{x}'). \tag{A.6}$$

Further introduce the corresponding displacement field $u_{pi}^* = u_{pi}^*(\mathbf{x}-\mathbf{x}')$

$$\begin{aligned} u_i^* &= u_{pi}^*(\mathbf{x}-\mathbf{x}')e_p \\ \epsilon_{ij}^* &= \epsilon_{pij}^*(\mathbf{x}-\mathbf{x}')e_p. \end{aligned} \tag{A.7}$$

Tensor u_{pi}^* is the so-called *fundamental solution* that satisfies the Lamé equation

$$L^0_{ijkl}u^*_{pk,lj}(\mathbf{x}-\mathbf{x}') + \delta_{pi}\delta(\mathbf{x}-\mathbf{x}') = 0. \tag{A.8}$$

It represents the displacements in the i direction at point $\mathbf{x}$ due to a unit point force applied at point $\mathbf{x}'$ in the direction p. Similarly, tensor ϵ_{pij}^* given by

$$\epsilon^*_{pij} = \frac{1}{2}(u^*_{pi,j} + u^*_{pj,i}), \tag{A.9}$$

then corresponds to the strains at point $\mathbf{x}$ due to a unit point force applied at point $\mathbf{x}'$ in the p^{th} direction. Substituting Eqs. (A.5)-(A.7) into Eq. (A.4) gives

$$\begin{aligned} u'_p(\mathbf{x}') &= \int_S \left(L^0_{ijkl}u'_{k,l}(\mathbf{x}) + \tau_{ij}(\mathbf{x}) - \overline{\tau}_{ij}(\mathbf{x})\right) n_j u^*_{pi}(\mathbf{x}-\mathbf{x}')\,\mathrm{d}S(\mathbf{x}) \\ &- \int_\Omega \left(\tau_{ij}(\mathbf{x}) - \overline{\tau}_{ij}(\mathbf{x})\right)\epsilon^*_{pij}(\mathbf{x}-\mathbf{x}')\,\mathrm{d}\Omega(\mathbf{x}). \end{aligned} \tag{A.10}$$

Finally, differentiating the above equation with respect to $\mathbf{x}'$ provides the operator $[\boldsymbol{\epsilon}_0^*(\boldsymbol{\tau}-\overline{\boldsymbol{\tau}})]$ in the form

$$\begin{aligned} \epsilon'_{pq}(\mathbf{x}') &= -\int_S \left(L^0_{ijkl}u'_{k,l}(\mathbf{x}) + \tau_{ij}(\mathbf{x}) - \overline{\tau}_{ij}(\mathbf{x})\right) n_j \epsilon^*_{ipq}(\mathbf{x}-\mathbf{x}')\,\mathrm{d}S(\mathbf{x}) \\ &+ \int_\Omega \left(\tau_{ij}(\mathbf{x}) - \overline{\tau}_{ij}(\mathbf{x})\right)\epsilon^*_{ijpq}(\mathbf{x}-\mathbf{x}')\,\mathrm{d}\Omega(\mathbf{x}) \\ &= \left[\boldsymbol{\epsilon}_0^*(\boldsymbol{\tau}-\overline{\boldsymbol{\tau}})\right], \end{aligned} \tag{A.11}$$

in which the singularity at $\mathbf{x} = \mathbf{x}'$ is interpreted in the sense of distributions. The values of $L^0_{ijkl} u'_{k,l} n_j$ on S follow from the solution of integral equation (A.10) subjected to $\boldsymbol{u}' = \mathbf{0}$ on S. These values, however, are not needed explicitly if neglecting the contribution due to boundary integral. Recall discussion above. The local strain thus follows from superposition of oscillating part of strain $\boldsymbol{\epsilon}'$ and the uniform strain $\boldsymbol{E}$ (recall Section 4.1, Fig. 4.1)

$$\epsilon_{pq}(\mathbf{x}') \;=\; \epsilon'_{pq} + E_{pq} = E_{pq} + \int_\Omega \left(\tau_{ij}(\mathbf{x}) - \overline{\tau}_{ij}(\mathbf{x})\right) \epsilon^*_{ijpq}(\mathbf{x} - \mathbf{x}') \, \mathrm{d}\Omega(\mathbf{x}), \tag{A.12}$$

with $\boldsymbol{\epsilon}'$ now given by

$$\epsilon'_{pq}(\mathbf{x}') \;=\; \int_\Omega \epsilon^*_{ijpq}(\mathbf{x} - \mathbf{x}') \left(\tau_{ij}(\mathbf{x}) - \overline{\tau}_{ij}(\mathbf{x})\right) \, \mathrm{d}\Omega(\mathbf{x}). \tag{A.13}$$

To conclude, recall the term $\boldsymbol{\tau}^{\mathrm{T}} \boldsymbol{\epsilon}'$ which appears in Eq. (4.9). Hence

$$\boldsymbol{\tau}^{\mathrm{T}} \boldsymbol{\epsilon}' \;=\; \boldsymbol{\tau}^{\mathrm{T}} \int_\omega \epsilon^*_0(\mathbf{x} - \mathbf{x}') \left(\boldsymbol{\tau}(\mathbf{x}) - \overline{\boldsymbol{\tau}}(\mathbf{x})\right) \, \mathrm{d}\Omega(\mathbf{x}). \tag{A.14}$$

Finally, ensemble averaging yields

$$\overline{\boldsymbol{\tau}^{\mathrm{T}} \boldsymbol{\epsilon}'} \;=\; \sum_r \sum_s \boldsymbol{\tau}_r{}^{\mathrm{T}}(\mathbf{x}') \int_\Omega \boldsymbol{\epsilon}^*_0(\mathbf{x} - \mathbf{x}') \left[S_{rs}(\mathbf{x} - \mathbf{x}') - c_r c_s\right] \boldsymbol{\tau}_s(\mathbf{x}) \, \mathrm{d}\Omega(\mathbf{x}) \tag{A.15}$$

Compare with Eqs. (4.20) and (4.21).

Appendix B

EVALUATION OF MICROSTRUCTURE-DEPENDENT QUANTITIES

B.1 Evaluation of $M(r)$ for impenetrable cylinders

The function $M(r)$ appears in the relation for the two-point matrix probability function of particulate media (see Eq.(2.36)). For the statistically isotropic media, it takes the form

$$M(r_{12}) = \int\int h(r_{34})m(r_{13})m(r_{24})\mathrm{d}\mathbf{r}_3\mathrm{d}\mathbf{r}_4. \tag{B.1}$$

An elegant approach based on the Fourier transform is available to evaluate the above integral. Starting from Eq. (C.1) the Fourier transform of function $h(\mathbf{x})$ is given by

$$\widetilde{h}(\boldsymbol{\xi}) = \int h(\mathbf{x})e^{\mathrm{i}\boldsymbol{\xi}\cdot\mathbf{x}}\mathrm{d}\mathbf{x}. \tag{B.2}$$

Writing Eq. (B.2) in polar coordinates gives

$$\begin{aligned}
\widetilde{h}(\xi,\theta) &= \int_0^\infty\int_0^{2\pi} h(r)e^{\mathrm{i}r\xi(\cos\theta\cos\phi+\sin\theta\sin\phi)}r\,\mathrm{d}r\mathrm{d}\phi = \\
&= \int_0^\infty\int_0^{2\pi} h(r)e^{\mathrm{i}r\xi(\cos(\theta-\phi))}r\,\mathrm{d}r\mathrm{d}\phi = \\
&= \int_0^\infty h(r)\,r\left(\int_0^{2\pi} e^{\mathrm{i}r\xi\cos\alpha}\mathrm{d}\alpha\right)\mathrm{d}r
\end{aligned} \tag{B.3}$$

Note that the bracketed term can be written as [Rektorys, 1995b, p. 663]

$$\int_0^{2\pi} e^{\mathrm{i}r\xi\cos\alpha}\mathrm{d}\alpha = 2\pi J_0(r\xi), \tag{B.4}$$

where J_0 is the Bessel function of the first kind and 0-th order. Eq. (B.3) then attains the following form

$$\boxed{\widetilde{h}(\xi) = 2\pi\int_0^\infty h(r)J_0(r\xi)\,r\,\mathrm{d}r}. \tag{B.5}$$

It now becomes advantageous to replace $h(r)$ with function $K(r)$ using Eqs. (2.31) and (2.32). Hence

$$\begin{aligned}\widetilde{h}(\xi) &= 2\pi\int_0^\infty h(r)rJ_0(r\xi)\mathrm{d}r = 2\pi\int_0^\infty \frac{1}{2\pi r}\frac{\mathrm{d}\widehat{K}(r)}{\mathrm{d}r}rJ_0(r\xi)\mathrm{d}r = \\ &= \int_0^\infty \frac{\mathrm{d}\widehat{K}(r)}{\mathrm{d}r}J_0(r\xi)\mathrm{d}r = \boxed{\xi\int_0^\infty \widehat{K}(r)J_1(r\xi)\mathrm{d}r} + \Big[J_0(r\xi)\widehat{K}(r)\Big]_0^\infty \end{aligned} \tag{B.6}$$

where $\widehat{K}(r) = K(r) - \pi r^2$ and J_1 is the Bessel function of the first kind and first order. The last term in Eq. (B.6) vanishes, since $\widehat{K}(0) = 0$ and for $r \to \infty$ $J_0(r\xi) \to 0$ and $\widehat{K}(r) \to$ const.

The quantity $\widetilde{m}(\xi)$ is provided by

$$\widetilde{m}(\xi) = 2\pi\int_0^\infty H(R-r)J_0(r\xi)\,r\,\mathrm{d}r = 2\pi\int_0^R J_0(r\xi)\,r\,\mathrm{d}r. \tag{B.7}$$

Note that (see [Rektorys, 1995b, p. 664])

$$\frac{\mathrm{d}}{\mathrm{d}r}(rJ_1(r)) = J_1(r) + r\frac{\mathrm{d}J_1(r)}{\mathrm{d}r} = J_1(r) + (-J_1(r) + rJ_0(r)) = rJ_0(r),$$

so that integral (B.7) yields

$$\widetilde{m}(\xi) = \left[\frac{2\pi r}{\xi}J_1(r\xi)\right]_0^R = \boxed{\frac{2\pi R}{\xi}J_1(R\xi)} \tag{B.8}$$

Using similar procedure and employing relation (B.5), the inverse transform of function $\widetilde{M}(\xi)$ can be obtained as

$$M(r) = \frac{1}{2\pi}\int_0^\infty \widetilde{M}(\xi)\xi J_0(r\xi)\mathrm{d}\xi. \tag{B.9}$$

B.2 Evaluation of matrices $\mathbf{A}_{rs}$ *and* $\mathbf{B}_{rs}$

Consider Eq. (4.30) to write the microstructure-dependent matrices $\mathbf{A}_{rs}$ in the form

$$\begin{aligned}\mathbf{A}_{rs} &= \int_\Omega \boldsymbol{\epsilon}_0^*(\mathbf{x}-\mathbf{x}')\left[S_{rs}(\mathbf{x}-\mathbf{x}') - c_r c_s\right]\mathrm{d}\Omega(\mathbf{x}') \\ &= \int_\Omega \boldsymbol{\epsilon}_0^*(\mathbf{x}-\mathbf{x}')S'_{rs}(\mathbf{x}-\mathbf{x}')\,\mathrm{d}\Omega(\mathbf{x}') = \int_\Omega \boldsymbol{\epsilon}_0^*(\mathbf{x})S'_{rs}(\mathbf{x})\,\mathrm{d}\Omega(\mathbf{x}),\end{aligned} \tag{B.10}$$

where S'_{rs} denotes the fluctuating part of S_{rs} under the no-long range orders hypothesis. Next, using Eq. (C.1) observe that the preceding formula can be written as

$$\begin{aligned} \mathbf{A}_{rs} &= \int_\Omega \boldsymbol{\epsilon}_0^*(\mathbf{x}) S'_{rs}(\mathbf{x})\, \mathrm{d}\Omega(\mathbf{x}) \\ &= \left[\int_\Omega \boldsymbol{\epsilon}_0^*(\mathbf{x}) S'_{rs}(\mathbf{x}) e^{\mathrm{i}\mathbf{x}\cdot\boldsymbol{\xi}}\, \mathrm{d}\Omega(\mathbf{x})\right]_{\boldsymbol{\xi}=\mathbf{0}} = \mathcal{F}\left[\boldsymbol{\epsilon}_0^*(\mathbf{x}) S'_{rs}(\mathbf{x})\right]_{\boldsymbol{\xi}=\mathbf{0}}. \end{aligned} \tag{B.11}$$

Then, recall Eq. (C.10) to get

$$\mathbf{A}_{rs} = \frac{1}{(2\pi)^d}\left[\int_\Omega \widetilde{\boldsymbol{\epsilon}_0^*}(\boldsymbol{\xi}-\boldsymbol{\xi'})\widetilde{S'}_{rs}(\boldsymbol{\xi'})\mathrm{d}\boldsymbol{\xi'}\right]_{\boldsymbol{\xi}=\mathbf{0}} = \frac{1}{(2\pi)^d}\int_\Omega \widetilde{\boldsymbol{\epsilon}_0^*}(-\boldsymbol{\xi'})\widetilde{S'}_{rs}(\boldsymbol{\xi'})\mathrm{d}\boldsymbol{\xi'} \tag{B.12}$$

Since $\widetilde{\epsilon_0^*}(-\boldsymbol{\xi}) = \widetilde{\epsilon_0^*}(\boldsymbol{\xi})$ we finally arrive at

$$\mathbf{A}_{rs} = \frac{1}{(2\pi)^d}\int_\Omega \widetilde{\boldsymbol{\epsilon}_0^*}(\boldsymbol{\xi'})\widetilde{S'}_{rs}(\boldsymbol{\xi'})\mathrm{d}\boldsymbol{\xi'} \tag{B.13}$$

Similar procedure then provides

$$\mathbf{B}_{rs} = \frac{1}{(2\pi)^d}\int_\Omega \widetilde{\boldsymbol{\sigma}_0^*}(\boldsymbol{\xi'})\widetilde{S'}_{rs}(\boldsymbol{\xi'})\mathrm{d}\boldsymbol{\xi'} \tag{B.14}$$

Note that Fourier's transform $\widetilde{\boldsymbol{\epsilon}_0^*}$ or $\widetilde{\boldsymbol{\sigma_0}^*}$ can be obtained for any homogeneous anisotropic reference media (see Appendix C, Section C.4), which is not generally possible for function $\boldsymbol{\epsilon}_0^*$ itself. Therefore, once we are able to compute the values of $\widetilde{S'}_{rs}$ we may evaluate integrals (B.13) and (B.14) by appropriate numerical procedure such as the familiar Gaussian quadrature.

Appendix C

THE FOURIER TRANSFORM

C.1 The Fourier transform

The d-dimensional Fourier transform of function $f(\mathbf{x})$ is provided by

$$\mathcal{F}\left[f(\mathbf{x})\right] = \widetilde{f}(\xi) = \int_{\Omega} f(\mathbf{x}) e^{\mathrm{i}\boldsymbol{\xi}\cdot\mathbf{x}} \mathrm{d}\mathbf{x}, \tag{C.1}$$

where i is the imaginary unit. The operator $\mathcal{F}$ is called the Fourier transform operator. The inverse operator $\mathcal{F}^{-1}$ is obtained by changing the sign of i and dividing by $(2\pi)^d$. Hence, the inverse Fourier transform is given by

$$\mathcal{F}^{-1}\left[\widetilde{f}(\boldsymbol{\xi})\right] = f(\mathbf{x}) = (2\pi)^{-d} \int_{\Omega} f(\boldsymbol{\xi}) e^{-\mathrm{i}\boldsymbol{\xi}\cdot\mathbf{x}} \mathrm{d}\boldsymbol{\xi}. \tag{C.2}$$

Simple algebra shows that the operator $\mathcal{F}$ satisfies the following equation

$$\mathcal{F}^{-1}\left[\mathcal{F}\left[f(\mathbf{x})\right]\right] = f(\mathbf{x}). \tag{C.3}$$

Provided that function $f(\mathbf{x})$ decays "sufficiently rapidly" to 0 for $|\mathbf{x}| \to \infty$ we have

$$\left(\widetilde{\frac{\partial f}{\partial x_i}}\right)(\boldsymbol{\xi}) = \int_{\Omega} \frac{\partial f}{\partial x_i} e^{\mathrm{i}\boldsymbol{\xi}\cdot\mathbf{x}} \mathrm{d}\mathbf{x} = -\mathrm{i}\xi_i \int_{\Omega} f(\mathbf{x}) e^{\mathrm{i}\boldsymbol{\xi}\cdot\mathbf{x}} \mathrm{d}\mathbf{x} = -\mathrm{i}\xi_i \widetilde{f}(\boldsymbol{\xi}). \tag{C.4}$$

C.2 Discrete Fourier Transform

The Discrete Fourier Transform (DFT) often replaces its continuous counterpart when analyzing discrete systems such as digitized images of real microstructures. The complexity of their geometries usually calls for sampling of large micrographs, recall Fig. 2.3. The actual microstructure is then approximated by the measured segment periodically extended

outside the measured region. Such a representation invites an application of the DFT to carry out Fourier analysis if needed. Clearly, the discrete Fourier representation results in periodic representation in real space. Note that the spectrum of the discrete real space is also periodic.

Without loss of generality we now limit our attention to a one-dimensional problem and consider a discrete set of N points defined on the interval $0 \leq n \leq N-1$. Applying a discrete version of the Fourier series this set is given by

$$x(n) = \frac{1}{N} \sum_{k=0}^{N-1} \xi(k) \mathrm{e}^{\mathrm{i}(2\pi/N)kn}, \tag{C.5}$$

where the coefficients $\xi(k)$ are provided by the Discrete Fourier Transform of $x(n)$

$$\xi(k) = \frac{1}{N} \sum_{n=0}^{N-1} x(n) \mathrm{e}^{-\mathrm{i}(2\pi/N)kn}. \tag{C.6}$$

Extension to cover 2D and 3D problems is rather straightforward. Further discussion on this subject can be found in very readable form in [Burrus and Parks, 1985].

C.3 The convolution theorem

The convolution of two functions f and g is defined as

$$\int_{\Omega} f(\mathbf{x} - \mathbf{x}') g(\mathbf{x}') \mathrm{d}\mathbf{x}'.$$

The convolution theorem states that the transform of the convolution equals the product of the transforms

$$\mathcal{F}\left[\int_{\Omega} f(\mathbf{x} - \mathbf{x}') g(\mathbf{x}') \mathrm{d}\mathbf{x}'\right] = \mathcal{F}\left[f(\mathbf{x})\right] \mathcal{F}\left[g(\mathbf{x})\right]. \tag{C.7}$$

The prove is remarkably simple (see [Sokolnikoff and Redheffer, 1958] for further discussion). We have

$$\begin{aligned} \mathcal{F}\left[\int_{\Omega} f(\mathbf{x} - \mathbf{x}') g(\mathbf{x}') \mathrm{d}\mathbf{x}'\right] &= \int_{\Omega} \left[\int_{\Omega} f(\mathbf{x} - \mathbf{x}') g(\mathbf{x}') \mathrm{d}\mathbf{x}'\right] e^{\mathrm{i}\boldsymbol{\xi}\cdot\mathbf{x}} \mathrm{d}\mathbf{x} \\ &= \int_{\Omega} g(\mathbf{x}') \left[\int_{\Omega} f(\mathbf{x} - \mathbf{x}') e^{\mathrm{i}\boldsymbol{\xi}\cdot\mathbf{x}} \mathrm{d}\mathbf{x}\right] \mathrm{d}\mathbf{x}' \\ &= \mathcal{F}\left[f(\mathbf{x})\right] \int g(\mathbf{x}') e^{\mathrm{i}\boldsymbol{\xi}\cdot\mathbf{x}'} \mathrm{d}\mathbf{x}' = \mathcal{F}\left[f\right] \mathcal{F}\left[g\right] \end{aligned} \tag{C.8}$$

Similarly, using Eq. (C.2) gives

$$\mathcal{F}^{-1}\left[\int_\Omega \widetilde{f}(\boldsymbol{\xi}-\boldsymbol{\xi'})\widetilde{g}(\boldsymbol{\xi'})\mathrm{d}\boldsymbol{\xi}'\right] = (2\pi)^d f(\mathbf{x})g(\mathbf{x}), \tag{C.9}$$

which implies that

$$\mathcal{F}\left[f(\mathbf{x})g(\mathbf{x})\right] = (2\pi)^{-d}\int_\Omega \widetilde{f}(\boldsymbol{\xi}-\boldsymbol{\xi'})\widetilde{g}(\boldsymbol{\xi'})\mathrm{d}\boldsymbol{\xi'}. \tag{C.10}$$

Finally, the Fourier transform of the integral

$$\int_\Omega f(\mathbf{x}+\mathbf{x}')g(\mathbf{x}')\mathrm{d}\mathbf{x}',$$

where $g(\mathbf{x})$ is a real function, is given by ([Press et al., 1992] Chapter 12)

$$\mathcal{F}\left[\int_\Omega f(\mathbf{x}+\mathbf{x}')g(\mathbf{x}')\mathrm{d}\mathbf{x}'\right] = \mathcal{F}\left[f(\mathbf{x})\right]\overline{\mathcal{F}\left[g(\mathbf{x})\right]}, \tag{C.11}$$

where $\bar{\cdot}$ means complex conjugate and should not be mistaken with the ensemble average used before.

C.4 Fourier transform of the Dirac delta function

General properties of the Dirac delta function are discussed in Appendix A. In particular, Eq. (A.6) can be used to infer

$$\int_\Omega \delta(\mathbf{x})e^{\mathrm{i}\boldsymbol{\xi}\cdot\mathbf{x}}\mathrm{d}x = \mathbf{1}, \tag{C.12}$$

where $\mathbf{1}$ represents the identity matrix. Hence, the inverse relation gives

$$\frac{1}{(2\pi)^d}\int_\Omega \mathbf{1}\cdot e^{-\mathrm{i}\boldsymbol{\xi}\cdot\mathbf{x}}\mathrm{d}\boldsymbol{\xi} = \delta(\mathbf{x}). \tag{C.13}$$

C.5 The Fourier transform of tensors ϵ^*_{ijkl} and σ^*_{ijkl}

In Chapter 4 we introduced the forth order tensors ϵ^*_{ijkl} and σ^*_{ijkl} related to the fundamental solution u^*_{ij}. Specific forms of these tensors for a homogeneous and isotropic material can be found e.g. in [Bittnar and Šejnoha, 1996]. Their Fourier transforms, however, needed for evaluations of matrices $\mathbf{A}_{rs}$ and $\mathbf{B}_{rs}$ in Eqs. (4.30) and (4.58) deserve more attention.

First, consider the tensor ϵ^*_{ijkl}. When differentiating Eq. (A.10) it becomes clear that

$$\epsilon^*_{ijkl}(\boldsymbol{x}) = \frac{1}{2}\left(\epsilon^*_{ikl,j}(\boldsymbol{x}) + \epsilon^*_{jkl,i}(\boldsymbol{x})\right). \tag{C.14}$$

Then, introducing Eq. (A.9) into Eq. (C.14) yields

$$\epsilon^*_{ijkl}(\boldsymbol{x}) = \frac{1}{4}\left(u^*_{ik,lj}(\boldsymbol{x}) + u^*_{il,kj}(\boldsymbol{x}) + u^*_{jk,li}(\boldsymbol{x}) + u^*_{jl,ki}(\boldsymbol{x})\right). \tag{C.15}$$

Hence, according to definition the Fourier transform of Eq. (C.15) can be written in the form

$$\widetilde{\epsilon}^*_{ijkl}(\boldsymbol{\xi}) = -\frac{1}{4}\left(\widetilde{u}^*_{ik}(\boldsymbol{\xi})\xi_l\xi_j + \widetilde{u}^*_{il}(\boldsymbol{\xi})\xi_k\xi_j + \widetilde{u}^*_{jk}(\boldsymbol{\xi})\xi_l\xi_i + \widetilde{u}^*_{jl}(\boldsymbol{\xi})\xi_k\xi_i\right). \tag{C.16}$$

Similarly, the Fourier transform of Eq. (A.8) reads

$$-L^0_{ijkl}\xi_i\xi_l\widetilde{u}^*_{jm}(\boldsymbol{\xi}) + \delta_{km} = 0, \tag{C.17}$$

so that

$$\widetilde{u}^*_{jk}(\boldsymbol{\xi}) = \left(L^0_{ijkl}\xi_i\xi_l\right)^{-1}. \tag{C.18}$$

For a homogeneous and isotropic material the above equation assumes the form

$$\widetilde{u}^*_{jk}(\boldsymbol{\xi}) = \frac{1}{|\boldsymbol{\xi}|^2\mu}\delta_{jk} - \frac{\lambda+\mu}{\mu(\lambda+2\mu)}\frac{\xi_j}{|\boldsymbol{\xi}|^2}\frac{\xi_k}{|\boldsymbol{\xi}|^2}, \tag{C.19}$$

where λ and μ are Lamé parameters. Finally, substituting Eq (C.19) into Eq (C.16) gives the Fourier transform of the tensor ϵ^*_{ijkl}

$$\widetilde{\epsilon}^*_{ijkl} = -\frac{1}{|\boldsymbol{\xi}|^4\mu}\left\{\frac{|\boldsymbol{\xi}|^2}{4}\left(\xi_j\xi_l\delta_{ik} + \xi_i\xi_l\delta_{jk} + \xi_j\xi_k\delta_{il} + \xi_i\xi_k\delta_{jl}\right) - \frac{\lambda+\mu}{\mu(\lambda+2\mu)}\xi_i\xi_j\xi_k\xi_l\right\}. \tag{C.20}$$

To derive the Fourier transform of the tensor σ^*_{ijkl} we begin with the constitutive law for isotropic material given by

$$\sigma_{ij}(\boldsymbol{x}) = \lambda u_{l,l}(\boldsymbol{x})\delta_{ij} + \mu(u_{i,j}(\boldsymbol{x}) + u_{j,i}(\boldsymbol{x})). \tag{C.21}$$

The above equation can be used to show that

$$\sigma^*_{ijkl}(\boldsymbol{x}) = \lambda\sigma^*_{mkl,m}\delta_{ij} + \mu(\sigma^*_{ikl,j} + \sigma^*_{jkl,i}), \tag{C.22}$$

where

$$\sigma^*_{ijk}(\boldsymbol{x}) = \lambda u^*_{il,l}(\boldsymbol{x})\delta_{jk} + \mu(u^*_{ij,k}(\boldsymbol{x}) + u^*_{ik,j}(\boldsymbol{x})). \tag{C.23}$$

Fourier transforming of Eq. (C.22) then provides

$$\widetilde{\sigma}^*_{ijkl}(\boldsymbol{\xi}) = -\mathrm{i}\lambda\widetilde{\sigma}^*_{mkl}(\boldsymbol{\xi})\xi_m\delta_{ij} - \mathrm{i}\mu(\widetilde{\sigma}^*_{ikl}(\boldsymbol{\xi})\xi_j + \widetilde{\sigma}^*_{jkl}(\boldsymbol{\xi})\xi_i), \tag{C.24}$$

where the Fourier transform of σ^*_{ijk} is given by

$$\widetilde{\sigma}^*_{ijk}(\boldsymbol{\xi}) = -\mathrm{i}\lambda\widetilde{u}^*_{il}(\boldsymbol{\xi})\xi_l\delta_{jk} - \mathrm{i}\mu(\widetilde{u}^*_{ij}(\boldsymbol{\xi})\xi_k + \widetilde{u}^*_{ik}(\boldsymbol{\xi})\xi_j). \tag{C.25}$$

Therefore, after substituting the above equation into Eq. (C.24) we arrive at

$$\begin{aligned}
\widetilde{\sigma}^*_{ijkl}(\boldsymbol{\xi}) \;=\; & -\lambda^2\widetilde{u}^*_{mn}(\boldsymbol{\xi})\xi_m\xi_n\delta_{ij}\delta_{kl} \\
& -\lambda\mu\left(\widetilde{u}^*_{mk}(\boldsymbol{\xi})\xi_l\xi_m\delta_{ij} + \widetilde{u}^*_{ml}(\boldsymbol{\xi})\xi_k\xi_m\delta_{ij} + \widetilde{u}^*_{in}(\boldsymbol{\xi})\xi_n\xi_j\delta_{kl} + \widetilde{u}^*_{jn}(\boldsymbol{\xi})\xi_n\xi_i\delta_{kl}\right) \\
& -\mu^2\left(\widetilde{u}^*_{ik}(\boldsymbol{\xi})\xi_l\xi_j + \widetilde{u}^*_{il}(\boldsymbol{\xi})\xi_k\xi_j + \widetilde{u}^*_{jk}(\boldsymbol{\xi})\xi_l\xi_i + \widetilde{u}^*_{jl}(\boldsymbol{\xi})\xi_k\xi_i\right).
\end{aligned} \tag{C.26}$$

The last step requires substitution of Eq. (C.19) into Eq. (C.26). After some lengthy algebra we finally get the desired results in the form

$$\begin{aligned}
\widetilde{\sigma}^*_{ijkl} \;=\; & -\frac{\lambda\mu}{|\xi|^2(\lambda+2\mu)}\left\{\frac{\lambda}{\mu}|\xi|^2\delta_{ij}\delta_{kl} - 4\frac{\lambda+\mu}{|\xi|^2\lambda}\xi_i\xi_j\xi_k\xi_l + 2\left(\xi_i\xi_j\delta_{kl} + \xi_k\xi_l\delta_{ij}\right)\right. \\
& \left. + \frac{\lambda+2\mu}{\lambda}\left(\xi_j\xi_l\delta_{ik} + \xi_j\xi_k\delta_{il} + \xi_i\xi_l\delta_{jk} + \xi_i\xi_k\delta_{jl}\right)\right\}
\end{aligned} \tag{C.27}$$

For a general anisotropic solid one may start from Eq. (C.16) and write the tensor $\widetilde{\sigma}^*_{ijkl}$ as

$$\widetilde{\sigma}^*_{ijkl} = L^0_{ijrs}\widetilde{\epsilon}^*_{rsmn}L^0_{mnkl}. \tag{C.28}$$